# Battery-Free Wireless Sensors for Internet-of-Things and Cyberphysical Systems

BY

LIANG ZHU
B.S., Sun Yat-Sen University, GuangZhou, China, 2012
M.S., Sun Yat-Sen University, GuangZhou, China, 2015

DISSERTATION

Submitted as partial fulfillment of the requirements
for the degree of Doctor of Philosophy in Electrical and Computer Engineering
in the Graduate College of the
University of Illinois at Chicago, 2021

Chicago, Illinois

Defense Committee:

Pai-Yen Chen, Chair and Advisor
Piergiorgio L. E. Uslenghi
Ahmet Enis Cetin
Jie Xu, Mechanical and Industrial Engineering
Haiyu Huang, Maxim Integrated, Inc,

## ACKNOWLEDGMENTS

I would express my sincere gratitude to my Ph.D. advisor, Prof. Pai-Yen Chen for his support and help. This is a great opportunity for me to work on my Ph.D. studies with Dr. Chen as my adviser who has mentored me not only in the academic research, but also for the development of my own personalities. Thank you so much for your patient, time and great help!

I am also grateful to all of those, whom I have had the pleasure to work with throughout my Ph.D. career. Additionally, I would like to thank my lab colleagues who helped me a lot during the past five years. Without your training and help, my research could not go smoothly.

Each of the members of my dissertation committee has provided me extensive personal and professional guidance and taught me a great deal about both scientific research and life in general. I also thank all the staff members of the ECE department at University of Illinois at Chicago for their help during my Ph.D. study.

LZ

# CONTRIBUTION OF AUTHORS

The Chapter 2, entitled "a compact hybrid-fed microstrip antenna for harmonics-based radar and sensor systems", is based upon the design and fabrication of a novel hybrid microstrip antenna. This result has been published in IEEE Antennas and Wireless Propagation Letters. I was responsible for designing, fabricating and composing the manuscript under the help of my advisor, Prof. Pai-Yen Chen. Besides, Dr. Nasser Alkhaldi and Dr. Haysam M Kadry helped me test the devices and collect the experimental data. Dr. Shaolin Liao helped me to polish the manuscript.

The Chapter 3, entitled "a zero-power ubiquitous wireless liquid-level sensor based on microfluidic-integrated microstrip antenna", is based on the design of a dual-resonance microstrip antenna constituted by an elliptical patch perturbed by shorting pins. In addition, we demonstrate a fully-passive compact harmonic sensor consisting of the proposed microstrip antenna loaded with a fluidic channel, aiming for practical liquid monitoring in rich-scattering environments. A portion of the content has been published in IEEE Journal of Radio Frequency Identification. In this project, I was responsible for the design, fabrication and test of the proposed harmonic sensor. Mr. Nabeel Alsaab helped me during the device fabrication and test stage. Prof. Mark Ming-Cheng Cheng and my advisor Prof. Pai-Yen Chen edited the manuscript.

The content of Chapter 4, entitled "a compact, passive frequency-hopping harmonic sensor based on a microfluidic reconfigurable dual-band antenna", is regarding the design and fabrication of a harmonic transponder that comprises a dual-band antenna reconfigured by different sample under test (SUT) injected in the fluidic cavity. A portion of the content of this Chapter has been published in IEEE Sensors Journal. Here, I was responsible for the design, fabrication and measurement of the proposed harmonic sensor. Dr. Mohamed Farhat and Dr. Yi-Chao Chen helped

# CONTRIBUTION OF AUTHORS (Continued)

me to optimize the hybrid antenna design. Dr. Khaled N Salama helped me with the fluidic channel design and test. Prof. Pai-Yen Chen was in charge of this project and help to edit the manuscript.

The Chapter 5 is about "absolute value wireless sensing based on nonlinear harmonic analysis assisted with frequency-hopping spread spectrum", which has been published in Measurement Science and Technology. In this project. I designed, fabricated and measured this fully passive harmonic tag. Prof. Pai-Yen Chen is responsible for improving the theory with regard to this passive tag in noisy environment, as well as editing the paper.

The content of Chapter 6 is based on the design and fabrication of "a compact, flexible harmonic transponder sensor with multiplexed sensing capabilities for rapid, contactless microfluidic diagnosis". The content has been published in IEEE Transactions on Microwave Theory and Techniques. I was working on the design, fabrication and test of this multiplexed harmonic sensor under the guidance from my advisor, Prof. Pai-Yen Chen. Dr. Haiyu Huang optimized the design of the passive circuits, and Prof. Mark Ming-Cheng Cheng contribute to polish the manuscript.

# TABLE OF CONTENT

CHAPTER PAGE

# TABLE OF CONTENT (Continued)

CHAPTER PAGE

# LIST OF TABLES

TABLE PAGE

# LIST OF FIGURES

# LIST OF FIGURES (Continued)

FIGURE PAGE

# LIST OF FIGURES (Continued)

FIGURE PAGE

# LIST OF FIGURES (Continued)

FIGURE PAGE

# LIST OF FIGURES (Continued)

FIGURE PAGE

# LIST OF FIGURES (Continued)

FIGURE PAGE

## SUMMARY

In the past decades, the passive interrogating techniques based on harmonic transponders have drawn tremendous attentions since it shows great potential for suppressing antenna cross talks, clutters, background echoes and also the electromagnetic interferences in the rich-scattering environment. In principle, the antenna sensors in the harmonic radar/sensor systems will receives the fundamental tone signal, doubling its resonant frequency through an integrated passive frequency doubler, and then re-transmitting the modulated higher order harmonics to the interrogators in the far field region. Thanks to the frequency orthogonality between the incident and re-transmitted signal, the backscattering multipath reflections and electromagnetic interferences have been successfully removed. The idea of harmonic sensor has been developed in industrial and medical applications, for example, wireless sensing of strain and continuous real-time monitoring of drug delivery.

However, the up-to-date harmonic transponder-based sensors still face several challenges. In general, they lack the capability of simultaneously dealing with multiple channels or multiple monitoring parameters, which will not satisfy the demand of many practical applications. Another drawback is the lack of flexibility, which further limits their applications in the fields of textile or wearable electronics.

# I. INTRODUCTION

In recent years, along with the development of smart world, the battery-free wireless sensing techniques have attracted increasing interests since the integration of communication networks with sensing nodes could provide prominent advantages with regard to higher data rate, real time information monitoring, and also the potential to synchronously upload data to the cloud base. So far, wireless sensing techniques have been widely explored in various areas including environmental monitoring, e.g., humidity, biological parameter and humidity. Unfortunately, most commonly used wireless devices are still active devices, in other words, they usually demand external power sources, like batteries or energy harvesters, that inevitably adds a large number of complexity or error sources within the system. To improve the system's robustness and durability, and to lower the maintenance costs, various battery-free wireless sensing techniques have been developed, which could be categorized into two groups. The first one is on the basis of near-field inductive or capacitive coupling mechanism that has been demonstrated effective for LC-based biomedical detectors, and capacitive humidity sensors. The second one is based on electromagnetic backscattering techniques with relatively long-distance wireless sensing. In this scenarios, antenna sensors and radio frequency identification sensors have been studied for detecting environmental changes remotely. However, although such systems can offer longer interrogation distance, they are typically vulnerable to scattering interferences and clutters surrounding these devices.

Very recently, low-profile harmonic sensors begin to gain attentions. Similar as a harmonic radar, which has been used for tracking objects with a very small RCS, a harmonic sensor will launch and detect orthogonal harmonic signals, and thus, successfully avoid clutters, multiple interferences, and crosstalks between transmitters and receviers. This approach has been investigated in remote sensing, localization of underground assets, and non-invasive monitoring

of critical symptoms in healthcare applications. Particularly, facing the crisis about global aging and pandemic, such as COVID-19, low-cost and disposable point-of-care tests, and drive-through inspections are in exponentially growing demands. Even though the existing harmonic sensors have numbers of advantages in IoT applications, they still have certain intrinsic and inevitable limitations. For example, they commonly lack the capability to test multiple channels or multiple parameters simultaneously, making them not applicable in many practical healthcare applications. Another challenge is poor mechanical flexibility that further limits their applications in the fields of flexible electronics.

Therefore, aiming at addressing the aforementioned issues, this thesis focuses on three major topics: (1) Compact and hybrid-fed antennas for harmonic wireless sensing applications; (2) Absolute wireless sensing approach based on harmonic analysis enabled by frequency-hopping spread spectrum; (3) Flexible harmonic sensors with multiplexed sensing capabilities for rapid, contactless microfluidic diagnosis.

**Chapter 2** presented a hybrid microstrip antenna for harmonic radars and sensors, which can receive the fundamental signal and re-transmit the modulated second harmonics. This antenna is enabled by a single-layer and dual-feed geometry, which consists of an inner circular antenna operating at 6 GHz related to $TM_{110}$ mode, and one outer split-ring patch antenna working at 3GHz enabled by the higher order $TM_{310}$ or $TM_{210}$ mode. Analytical solutions were derived for the antenna's resonant frequencies under different modes. Our measurement results report that the maximum gain is 1.17 dB at 3 GHz and 3.33 dB at 6 GHz, with a good impedance matching and high isolation.

**Chapter 3** studied a dual-resonance microstrip antenna constituted by an elliptical patch perturbed by shorting pins. In principle, this antenna uses $TM_{e110}$ mode to intercept the fundamental

tone at 2.86 GHz, and uses the $TM_{o110}$ mode to retransmit the second harmonics at 5.72 GHz. Furthermore, we have manufactured a wireless liquid sensor that comprises the proposed antenna and a liquid channel. Our results state that even in the rich-scattering environment full of clutters, echos, or electromagnetic interference, the second harmonics can still accurately indicate the dielectric properties of the liquid injected in the fluidic tank, e.g., acetone-water mixtures with various concentrations.

**Chapter 4** describes a battery-free wireless liquid sensor enabled by a harmonic transponder that comprises a dual-band antenna reconfigured by different sample under test (SUT) injected in the fluidic cavity. This microstrip antenna has the hybrid-feed geometry, in which an inner elliptical antenna exhibits wideband resonance at $2f_0$ enabled by hybridization of $TM_{o110}$ and $TM_{e110}$ modes, and an outer split-ring antenna displays a narrow band resonance at the fundamental frequency $f_0$. Particularly, the outer patch is mounted with a fluidic channel for controlling the resonance of the $TM_{310}$ mode at $f_0$. Our results demonstrate the potential of employing this passive wireless sensor in rich-scatting environments filled with crosstalks, clutters and multiple reflections.

**Chapter 5** introduces a wireless sensing platform, which can enable long-range interrogating of compact and passive sensors in complex environments. This telemetry approach requires postprocessing the higher order received signal strength indicator in the frequency hopping spread spectrum (i.e., FHSS), in which the harmonic sensor has a narrow resonance antenna sensor working at fundamental frequency $f_0$ and a wideband circular monopole antenna covering the second harmonic spectrum at $2f_0$. We have proved that the information of the liquid-reconfigured antenna sensor can be encoded in the peak value of the harmonic received signal strength indicator (RSSI) pattern.

**Chapter 6** discusses a flexible harmonic sensor, which is capable of performing multiplexed fluidic sensing. The harmonic sensor consists of two frequency-reconfigurable electrically-small antennas (ESAs) loaded with fluidic channels that are used for receiving radio-frequency waves at fundamental frequencies, and a broadband monopole antenna for re-transmitting the second-harmonics to a portable sniffer. We show that the injection of liquid samples into the fluidic channels, can dynamically detune the resonant frequencies of the ESAs, which then could be precisely extracted by processing the shift of the RSSI patterns. Additionally, we also demonstrate a prototype of rapid and multiplexed sample detection with the proposed harmonic sensor.

**Chapter 7** demonstrates a smart face mask based on the passive harmonic tag for performing real-time cough event monitoring. Our results indicate that the coughs can be accurately monitored through non-contact track of the received signal strength indicator (RSSI) at the harmonic frequency. Owing to the frequency orthogonality between the launched and backscattered radio-frequency (RF) signals, the harmonic tag-based smart mask can well suppress the electromagnetic interferences, such as clutters and crosstalks in noisy environments. We envision that this zero-power and lightweight wireless wearable device may be beneficial for cough monitoring and the public health condition in terms of tracking potential contagious person and virus-transmissive events.

Finally, in **Chapter 8**, I draw a conclusion regarding the impact of my works and briefly discuss some of the directions for future research areas that stem from these projects.

# II. A COMPACT HYBRID-FED MICROSTRIP ANTENNA FOR HARMONICS-BASED RADAR AND SENSOR SYSTEMS



In this chapter, I presented a hybrid microstrip antenna for harmonic radars and sensors applications, which can receive the fundamental signal and re-transmit the modulated second harmonics. This antenna is enabled by a single-layer and dual-feed geometry, which consists of an inner circular antenna operating at 6 GHz related to $TM_{110}$ mode, and one outer split-ring patch antenna working at 3GHz enabled by the higher order $TM_{310}$ or $TM_{210}$ mode. Analytical solutions were derived for the antenna's resonant frequencies under different modes. Our measurement results report that the maximum gain is 1.17 dB at 3 GHz and 3.33 dB at 6 GHz, with a good impedance matching and high isolation.

## 2.1 Introduction to harmonic transponder

Wireless sensing and tracking platforms have drawn increasingly growing interest in the emerging fields of smart health, internet-of-things (IoTs), and smart cities [1]-[3]. Most recently, battery-free telemetries based on harmonic detection, for example, harmonic radar [4]-[10] and harmonic sensors [11]-[16], have been gaining popularity, primarily thanks to its robustness to surrounding jammer, clutter, multipath interference, and even crosstalk between antennas. In these nonlinear systems, there is a compact tag or sensor on the basis of the passive harmonic transponder for receiving fundamental signal with frequency $f_0$, then doubling its frequency, and finally retransmitting the second harmonics (with frequency $2f_0$) to the interrogators located in a noisy environment, as illustrated

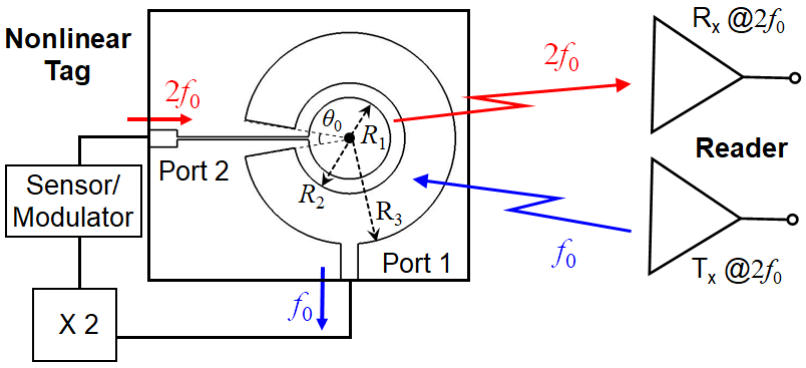


Figure 1. Schematics of a compact harmonic tag on the basis of the proposed hybrid-fed antenna

in Fig. 1. Given the fact that the reader transmits and receives signals at two orthogonal frequencies, the effect of the multi-path interferences and the clutters could be considerably suppressed.

These harmonic-based radar system has been demonstrated and visualized as promising techniques for tracking movements of low-RCS insects near the ground [4]-[10], which is impossible before due to strong clutters and reflections close to the interface. Most recently, battery-free and low-profile harmonic-based sensors have been developed for Internet-of-Things applications, with the advantages of lower power consumption and longer read range [11]-[16]. A harmonic-based sensor normally includes a physically or chemically-sensitive sensor for modulating the strength or resonant frequency of the backscattered harmonics [11]-[16]. This technique has been utilized for non-invasive detection of symptoms in healthcare applications [11]-[14], and also remote sensing for humidity and temperature [15], [16].

Even though the harmonic radar and its sensing systems could offer advantages with regard to detection range and power, they typically require two antennas operating at distant frequencies, one for the fundamental tone and another for harmonic frequency [4]-[16]. This will inevitably increases the overall devices' occupation are and cost. To address this limitation, we herein

propose a hybrid-fed microstrip antenna for the harmonic radar, sensing and tracking applications, as shown in Fig. 1. Unlike conventional harmonic transponders having separate antennas at two frequencies [2], the proposed one could significantly decrease the area occupation and is able to be predicted by an analytical model, with versatile modal excitation. This chapter is organized as follows. In Section 2.2, we use the cavity model to calculate the resonant modes and field distributions of the microstrip antenna, significant for determining feeding points. Next, we conduct the full-wave numerical simulations to further verify the analytical solutions. In Section 2.3, we experimentally fabricate the antennas and study their performance in terms of the reflection coefficient, antenna gain and radiation pattern. At last, we will conclude the results in Section 2.4. Note that our results demonstrate that the proposed antennas, despite of their compact size and good conformality, they can still provide good impedance matching and radiation properties, with acceptable high port isolations.

### 2.2 Design and simulation

Fig. 1 presents the geometry of the hybrid-fed microstrip antenna, which consists of a circular patch antenna (radius $R_1$), and a concentric split-ring patch antenna with outer radius $R_3$, inner radius $R_2$, and a cutting angle $\theta_0$. The two metal layers are separated by the 1.5 mm FR4 substrate that has a relative permittivity $\varepsilon_r = 4.3$ and loss tangent $\delta = 0.025$. The resonant frequency of this hybrid antenna could be estimated according to cavity model [3], in which the circular patch antenna and outer split-ring antenna respectively resonate at second harmonics ($2f_0$) and the fundamental frequency $f_0$. In each case, the PEC boundary condition is assumed for the top and bottom, and the PMC boundary condition is applied to the sidewalls. Therefore, the transcendental equation can be derived as accordingly, with the following for the inner cavity at different radius $R_1$:

$$J_n'(kR_1) = 0, \quad \text{and} \ \ n = 1,\ 2,\ 3\ldots \tag{1}$$

where $J_n(\cdot)$ and $Y_n(\cdot)$ are the Bessel functions for the first and second kinds, $k = \omega\sqrt{\varepsilon_r \varepsilon_0 \mu_0}$ with $\varepsilon_0$ and $\mu_0$ referring to free-space permittivity and permeability, respectively. As for the outer split ring cavity, the transcendental equation, will be a function of the radii $R_2$ and $R_3$, and also the cutting angle $\theta_0$, calculated as:

$$J_n'(kR_2)Y_n'(kR_3) - J_n'(kR_3)Y_n'(kR_2) = 0, \tag{2a}$$

$$n = m\frac{\pi}{2\pi - \theta_0}, \ \ \text{and} \ \ m = 1,\ 2,\ 3\ldots \tag{2b}$$

Here, we should note that for the inner circular cavity, the fundamental $TM_{110}$ mode should be excited at the second harmonic frequency $2f_0$, which is dedicatedly controlled by the radius $R_1$ , accordingly to Eq. (1). On the other hand, the higher-order modes $TM_{210}$ or $TM_{310}$ could be individually excited in the concentric split-ring cavity, by judiciously choosing the feed position that governs the fundamental frequency $f_0$, and can be adjusted by parameters $R_2$, $R_3$, and $\theta_0$, based on Eq. (2).

In this work, we have explored the dual-fed patch antenna for a harmonic transponder system with a fundamental frequency at 3 GHz and a harmonic frequency at 6 GHz. Note that the feeding position is important, since it determines the operation under specific $TM_{mn0}$ modes, and Eqs. (1) and (2) are utilized for deciding the geometries of this hybrid-fed microstrip patch antenna. To excite the $TM_{210}$ mode at 3 GHz, the concentric, split annular-ring patch are designed with $R_2$ = 7.6 mm, $R_3$ = 11 mm, and $\theta_0$ = 20°. At the same operating frequency of 3 GHz, the $TM_{310}$ mode will have the parameters as $R_2$ = 9 mm, $R_3$ = 17.2 mm, and $\theta_0$ = 20°. As for the inner circular patch

with $TM_{110}$ mode at 6 GHz, the radius will be $R_1$ = 6.72 mm. Here, it should be noted that although the outer split-ring patch with $TM_{110}$ mode can also operate at 3 GHz with the designed parameter $R_2$ = 3 mm

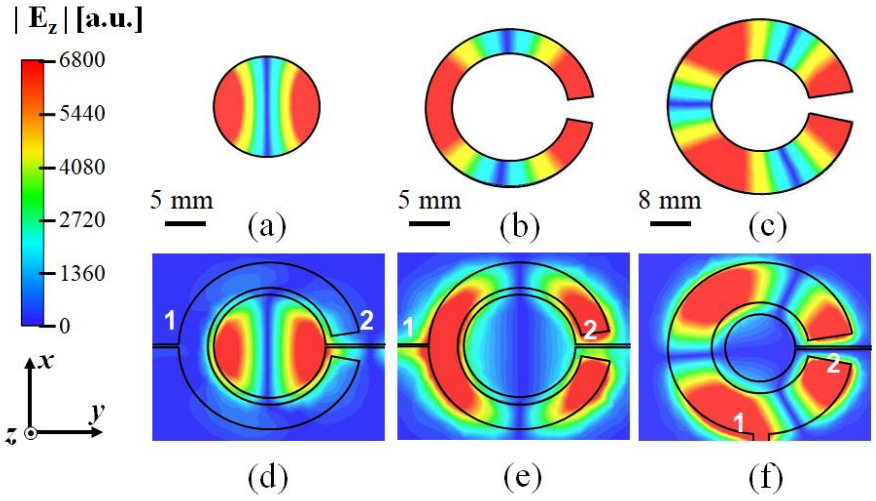


Figure 2. Snapshots of electric field distributions for (a) $TM_{110}$ mode of the circular-shape cavity at 6 GHz, and (b) $TM_{210}$ mode and (c) $TM_{310}$ mode of the split annular-ring cavity at 3 GHz. (d)-(f) are similar to (a)-(c), but for results of realistic microstrip antennas with microstrip line feeding.

and $R_3$ = 7 mm, the dimension $R_2$ will be smaller $R_1$, and thus, it is too small to be integrated with the inner circular patch $R_1$, unapplicable for harmonic transponder applications. By contrast, if the modes are higher than $TM_{410}$, the radiation pattern is undesirable with more side lobes, due to the complicated current distribution related to the higher order modes.

Next, we also conducted the full-wave numerical simulations to verify our analytical solution derived by the cavity model. According to the eigenmodal analysis in Fig. 2, we have studied two hybrid antennas, namely, one combination with $TM_{110}$ and $TM_{210}$ modes and another

one with $TM_{110}$ and $TM_{310}$, which are all fed by microstrip lines with 50 Ω excitation ports. By tuning the feeding point and the antenna geometry, both $TM_{210}$ and $TM_{310}$ modes could be excited at the 3 GHz, well suitable for serving as fundamental frequency receiver on harmonic tag. The optimal position of the feeding point for different modes could be achieved by observing the maximum field intensities location, as shown in Figs. 2(b) and 2(c). The snapshots of electric field distribution with regard to the realistic microstrip antenna under microstrip line feeding are reported in Figs. 2(d)-(f). A good agreement could be seen between the simulation results of the realistic antennas with microstrip line feeding network [Figs. 2(d)-(f)] and those calculated from the eigenmodal analysis [Figs. 2(a)-(c)].

### 2.3 Fabrication and measurement results

According to the simulated results in Section 2.2, we have manufactured four different types of hybrid-fed microstrip patch antennas for miniature harmonic transponders applications.

#### 2.3.1 Hybrid-fed $TM_{110}$-$TM_{210}$ microstrip patch antennas

We manufactured the designed microstrip antenna by using the low-cost PCB technique, with a 1.5 mm FR4 substrate. Fig. 3(a) presents the hybrid-fed $TM_{110}$-$TM_{210}$ antenna, in which the received fundamental signal will be guided into port 1, and the as-doubled signal will be re-radiated from the port 2. Fig. 3(b) reports the simulated and measured $S_{11}$ at different frequencies for the hybrid-fed microstrip antenna in Fig. 3(a). It is evidently seen that the measured and simulated results are in a good agreement, with small fluctuations due to fabrication and assembly errors. In Fig. 3(b), the analytical solutions obtained from Eqs. (1) and (2) are also highlighted. According to our measurement result, we confirm the resonant behaviors of this hybrid-fed patch antenna, with a significant $S_{11}$ dip at 3 GHz for fundamental frequency and $S_{22}$ dip at 6 GHz for second

harmonics. Moreover, both results imply a good impedance matching with a -10 dB bandwidth of 50 MHz at 3 GHz and 160 MHz at 6 GHz. The measured $S_{21}$ confirms a < -20 dB isolation between two ports.

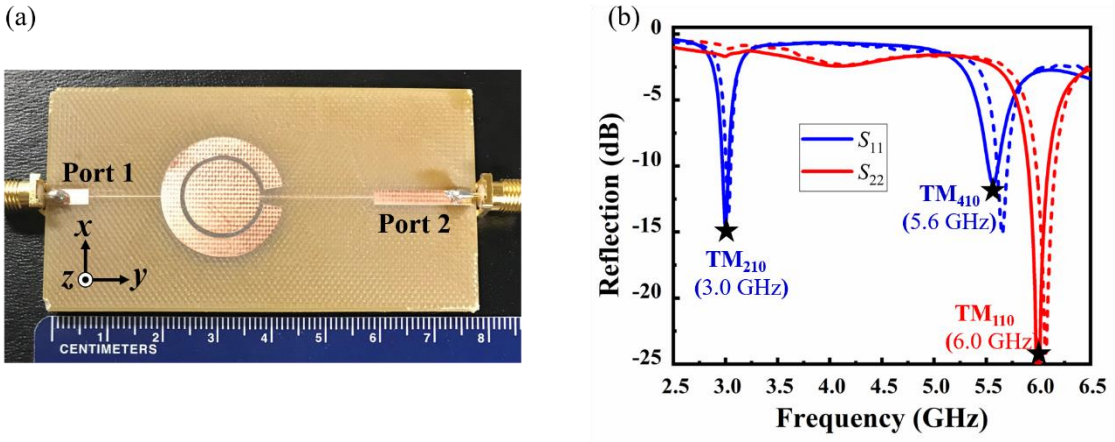


Figure 3. (a) Photograph of the hybrid-fed microstrip antenna with the $TM_{210}$ mode at 3GHz excited in the outer split-ring patch and the $TM_{110}$ mode at 6 GHz excited in the inner circular patch. (b) The simulated and measured $S_{11}$ and $S_{22}$ of the antenna in (a).

We should note that as can be clearly seen in Fig. 3(b), there exist some higher-order modes in the inner circular patch, such as $TM_{410}$ mode. However, its operating frequency is far from the fundamental frequency and second harmonics. Consequently, it will not affect the port isolations. Even though the hybrid-fed microstrip antenna discussed in Fig. 3 exhibits the desired resonant frequencies, geometry and radiation efficiency of 32% at 3 GHz and 54% at 6 GHz, the radiation pattern has been measured tilted away from broadside, due to the asymmetric current distributions on the split patch, induced by the perturbation of the microstrip feeding lines. To adjust the broadside pattern and achieve a maximum gain, the patch geometry should be modified, for example, with geometry perturbation by introducing truncated corners. Fig. 5(a) reports the refined geometry of

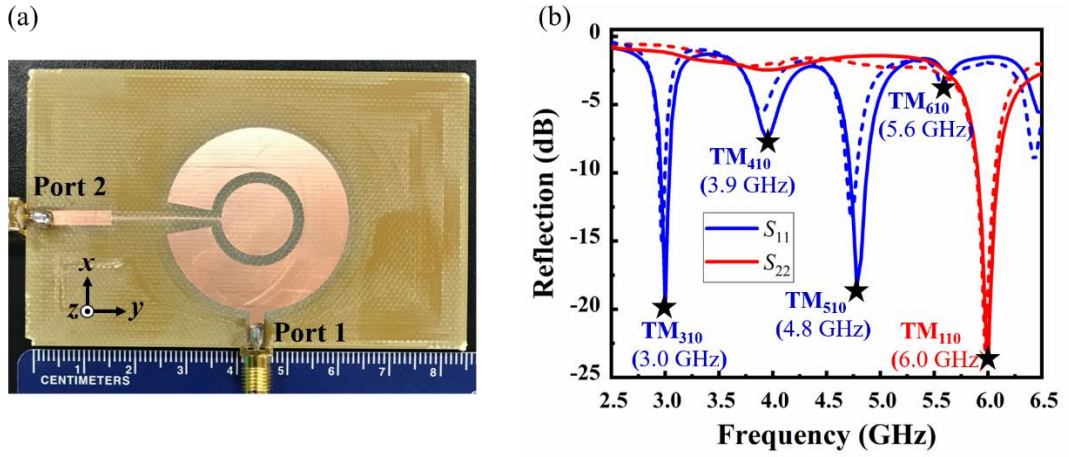


Figure 4. (a) Photograph of the hybrid-fed microstrip antenna with $TM_{110}$ -$TM_{310}$ modes. (b) The simulated and measured $S_{11}$ and $S_{22}$ of the antenna in (a)

the $TM_{110}$-$TM_{210}$ hybrid-fed antenna. Here, we should note that the geometric perturbation will not only adjust the broadside radiation pattern, but optimize the impedance matching and increase the realized gain of the antennas, as well as maintaining the radiation efficiency constant of 35% at 3 GHz and of 57% at 6 GHz, respectively. Fig. 5(b) reports the simulated and measured reflection coefficients versus frequency, presenting a good impedance matching at 3 GHz and 6 GHz with a high isolation. Fig. 6 reports the measured radiation patterns at the operating frequencies of the antennas. At 3 GHz for $TM_{210}$ mode, this antenna displays a maximum gain of 1.03 dBi, with a half-power beamwidth (HPBW) of 55° on the E-plane, and a HPBW of 93° on H-plane. At 6 GHz for $TM_{110}$ mode, this antenna shows a maximum realized gain of 2.83 dBi and a HPBW of

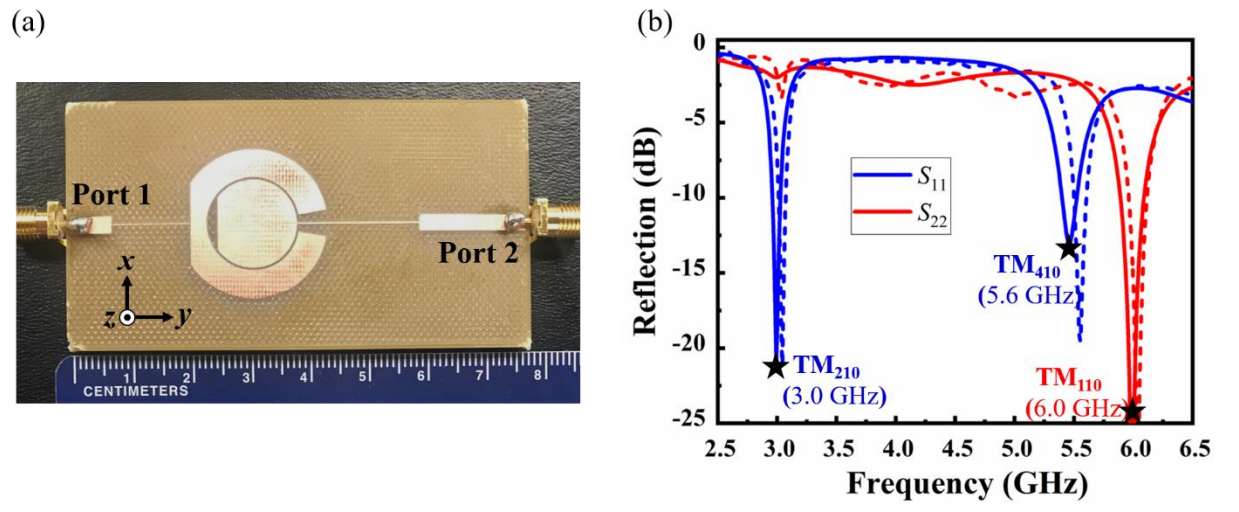


Figure 5. (a) Photograph of the hybrid-fed microstrip antenna similar to Fig. 3, but with geometric perturbations for refining the radiation pattern. (b) The simulated and measured $S_{11}$ and $S_{22}$ of the antenna in (a)

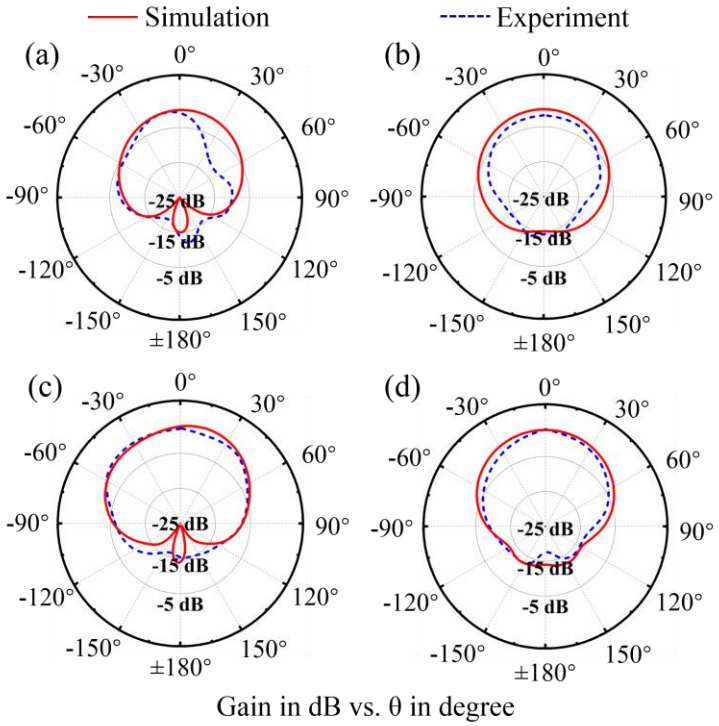


Figure 6. Radiation patterns for the antenna shown in Fig. 5. (a) and (b) are the E-plane and H-plane radiation patterns at 3 GHz, respectively. (c) and (d) are similar to (a) and (b), but for antenna at 6 GHz.

100° (74°) on the E-plane (H-plane), respectively. It should be noted that the smaller radiated patch and the symmetrical geometry of the $TM_{110}$-$TM_{210}$ mode antenna could provide feasibility for various size-restricted harmonic tags in harmonic radars or passive radio-frequency identification (RFID) applications.

### 2.3.2 Hybrid-fed $TM_{110}$-$TM_{310}$ microstrip patch antennas

In contrast to the $TM_{210}$ mode antenna, Figs. 4(a) and 4(b) present the manufactured $TM_{110}$-$TM_{310}$ microstrip patch [Fig. 2(f)] and its measured reflection coefficients. It is apparently seen that the measured results agree quite well with the simulated ones, where the resonance frequencies could be precisely estimated by the analytical solutions (stars). We should note that in this structure, some extra higher-order modes, accurately predicted by Eqs. (1)-(2), are also excited in the split-ring patch. However, with properly designed geometry of the patch, a good isolation and impedance matching could still be obtained simultaneously shown in Fig. 4(b). More straightforwardly, there are no resonant modes overlap, especially at the frequency bands of interest. The measured -10 dB bandwidth is 165 GHz at 6 GHz and is 50 MHz at 3 GHz. Again, the measured radiation pattern exhibits that the main beam is somehow tilted away from the broadside direction.

Similar to the $TM_{110}$-$TM_{210}$ hybrid-fed one, we also used geometric perturbations to the antenna in Fig. 4, aiming to improve the directivity toward the broadside and enhance the symmetricity of the radiation pattern of the antenna. The optimized results are shown in Fig. 7(a) with an improved radiation efficiency of 44% at 3 GHz and up to 56% at 6 GHz, maintaining nearly constant in contrast to the design in Fig. 6. Fig. 7(b) shows the simulated and measured reflection coefficients for this refined hybrid-fed antenna, exhibiting a consistent agreement for all resonant modes. The -10 dB bandwidth is measured as 50 MHz at 3 GHz and 240 MHz at 6 GHz, respectively,

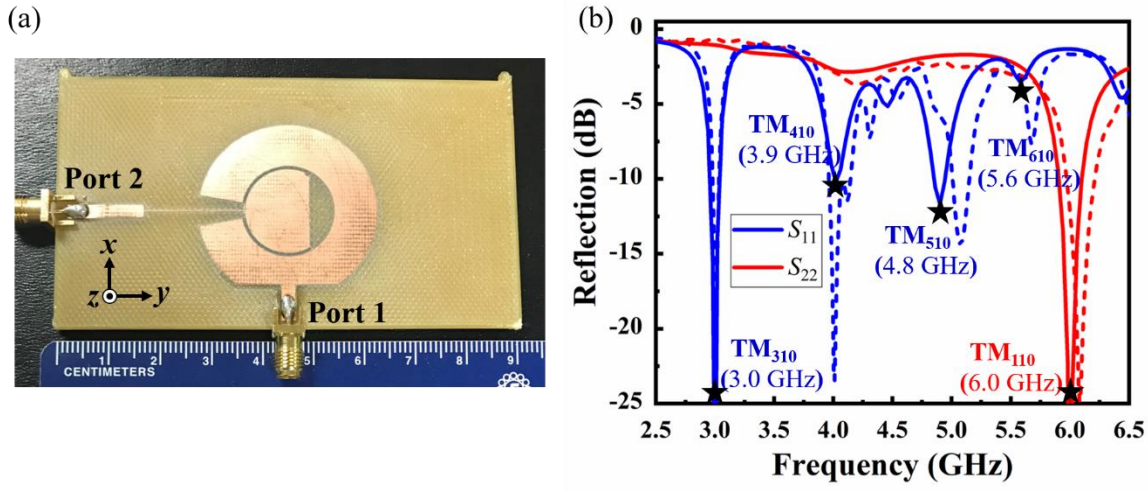


Figure 7. (a) Photograph of the hybrid-fed microstrip antenna with a perturbated geometry. (b) The simulated and measured reflection coefficient of the antenna.

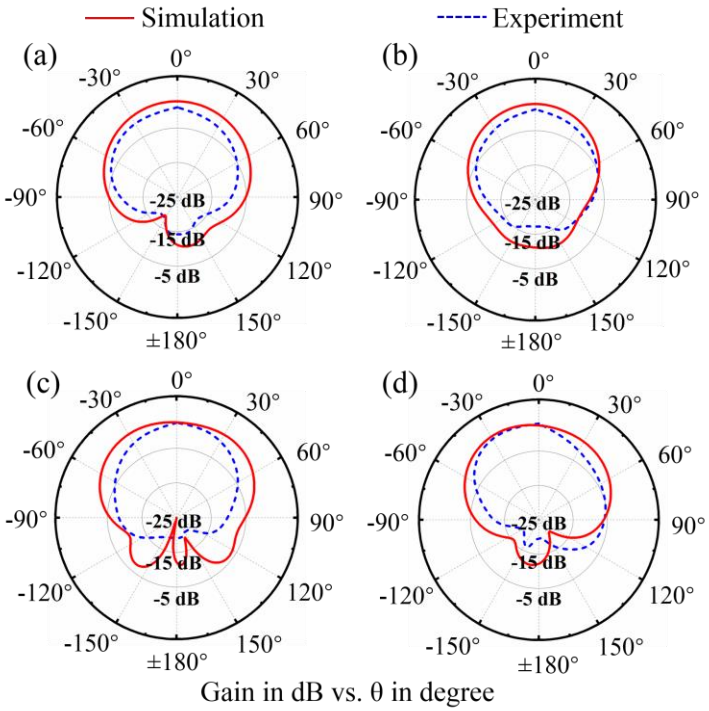


Figure 8. Radiation patterns for the hybrid-fed antenna in Fig. 7 with (a) and (b) are respectively the E and H-plane radiation patterns at 3 GHz. (c) and (d) are the E- and H-plane radiation patterns at 6 GHz, respectively.

almost unaltered compared to the bandwidth of the original design. Fig. 8 presents the radiation patterns for the antenna in Fig. 7. The maximum gain at 3 GHz for $TM_{310}$ mode is 1.17 dBi at 3 GHz, while the realized gain is slightly improved to 3.33 dBi at 6 GHz for $TM_{110}$ mode.

### 2.4 Conclusion

In this chapter, we have proposed a type of conformal and low-profile microstrip antenna for compact harmonic transponder applications. The proposed hybrid-fed geometry have apparently isolated resonances between the fundamental and second harmonic frequencies, which could be predicted analytically by solving transcendental equations. Additionally, we have demonstrated that the $TM_{110}$ and $TM_{210}$ (or $TM_{310}$) modes could be excited at 3 GHz and 6 GHz, respectively, by tailoring the feeding, as well as the antenna geometry. Our measurement results exhibit a satisfactory realized gain of the antennas with symmetrical broadside radiation patterns, along with good impedance matching and port isolation. The proposed hybrid microstrip patch antennas could benefit various size-restricted harmonic-based transponders used for harmonic sensors, harmonic radars, passive radio-frequency identification (RFID), medical implants, and internet-of-things (IoT) applications.

## REFERENCES


[1] J. Zhang, G. Y. Tian, A. M. J. Marindra, A. I. Sunny, and A. B. Zhao, "A Review of Passive RFID Tag Antenna-Based Sensors and Systems for Structural Health Monitoring Applications," *Sensors*, vol. 17, no. 265, 2017.

[2] X. L. Jia, Q. Y. Feng, T. H. Fan, and Q. S. Lei, "RFID technology and its applications in Internet of Things (IoT), "*2012 2nd International Conference on Consumer Electronics, Communications and Networks (CECNet)*, pp. 21-23, Yichang, China, 2012.

[3] S. Amendola, R. Lodato, S. Manzari, C. Occhiuzzi, and G. Marrocco, "RFID Technology for IoT-Based Personal Healthcare in Smart Spaces," *IEEE Internet Of Things Journal*, vol. 1, no. 2, pp. 144-152, 2014.

[4] J. R. Riley, A. D. Smith, D. R. Reynolds, A. S. Edwards, J. L. Osborne, I. H. Williams, et al, "Tracking bees with harmonic radar," *Nature*, vol. 379, pp. 29-30, 1996.

[5] L. Chioukh, H. Boutayeb, D. Deslandes, and K. Wu,, "Noise and sensitivity of harmonic radar architecture for remote sensing and detection of vital signs," *IEEE Trans. Microw. Theory. Techn*, vol. 62, no. 9, 2014.

[6] B. Kubina, J. Romeu, C. Mandel, M. Schüßler, and R. Jakoby, "Quasi-chipless wireless temperature sensor based on harmonic radar," *Electron. Lett*, vol. 50, no. 2, pp. 86-88, 2014.

[7] K. Rasilainen, J. Ilvonen, A. Lehtovuori, J. M. Hannula, and V. Viikari, "On design and evaluation of harmonic transponders," *IEEE Trans. Antennas Propag*, vol. 63, no. 1, pp. 15-23, 2015.

[8] K. Rasilainen, J. Ilvonen, J. M. Hannula, and V. Viikari, "Designing Harmonic Transponders Using Lumped-Component Matching Circuits, " *IEEE Antennas and Wireless Propag. Lett.*, vol. 16, pp. 246-249, 2017.

[9] Z. M. Tsai, P. H. Jau, N. C. Kuo, J. C. Kao, K. Y. Lin, F. R. Chang, et al, "A High-Range-Accuracy and High-Sensitivity Harmonic Radar Using Pulse Pseudorandom Code for Bee Searching," *IEEE Trans. Microw. Theory. Techn*, vol. 61, no. 1, pp. 666-675, 2012.

[10] D. Psychoudakis, W. Moulder, C. C. Chen, H. P. Zhu, and J. L. Volakis, "A portable low-power harmonic radar system and conformal tag for insect tracking," *IEEE Antennas and Wireless Propag. Lett.*, vol. 7, pp. 444-447, 2008.

[11] H. Y. Huang, L. Tao, F. Liu, L. Ji, Y. Hu, M. C. Cheng, et al, "Chemical-sensitive graphene modulator with a memory effect for internet-of-things applications," *Microsystems & Nanoengineering*, vol. 2, p. 16018, 2016.

[12] H. Huang, P. Y. Chen, C. H. Hung, R. Gharpurey, and D. Akinwande, "A zero power harmonic transponder sensor for ubiquitous wireless μL liquid-volume monitoring," *Sci. Rep*., vol. 6, p. 18795, 2016.

[13] M. Hajizadegan, M. Sakhdari, L. Zhu, Q. S. Cui, H. Y. Huang, M. C. Cheng, et al, "Graphene Sensing Modulator: Toward Low-Noise, Self-Powered Wireless Microsensors," *IEEE Sens*. J., vol. 17, no. 22, pp. 7239 - 7247, 2017.

[14] H. Y. Huang, M. Sakhdari, M. Hajizadegan, A. Shahini, D. Akinwande, and P. Y. Chen, "Toward transparent and self-activated graphene harmonic transponder sensors," *Appl. Phys. Lett.*, vol. 108, no. 17, p. 173503, 2016.

[15] F. Alimenti, and L. Roselli, "Theory of zero-power RFID sensors based on harmonic generation and orthogonally polarized antennas," *Progress in Electromagnetics Research*, vol. 134, pp. 337-357, 2013.

[16] A. Lazaro, R. Villarino, and D. Girbau, "A Passive Harmonic Tag for Humidity Sensing," *International Journal of Antennas and Propagation*, vol. 2014, 670345, 2014.

# III. A ZERO-POWER UBIQUITOUS WIRELESS LIQUID-LEVEL SENSOR BASED ON MICROFLUIDIC-INTEGRATED MICROSTRIP ANTENNA

Parts of this chapter have been presented in (Liang et al., 2020, IEEE JRFID) CC BY 4.0.

Harmonic sensors, capable of receiving radio-frequency signal and converting to a modulated harmonic signal, have been demonstrated efficient for signal interrogation in environments filled with strong clutters. In this chapter, we studied a dual-resonance microstrip antenna constituted by an elliptical patch perturbed by shorting pins. In principle, this antenna uses $TM_{e110}$ mode to intercept the fundamental tone at 2.86 GHz, and uses the $TM_{o110}$ mode to retransmit the second harmonics at 5.72 GHz. Furthermore, we have manufactured a wireless liquid sensor that comprises the proposed antenna and a liquid channel. Our results state that even in the rich-scattering environment full of clutters, echos, or electromagnetic interference, the second harmonics can still accurately indicate the dielectric properties of the liquid injected in the fluidic tank, e.g., acetone-water mixtures with various concentrations. The proposed dual-resonance antenna with low-profile and sensing capabilities could pave the way for nonlinear RFID tags and harmonic sensors.

## 3.1 Background

Compact and battery-free wireless sensors have become a subject of intense research in recent years due to their great potentials in many practical engineering applications, including smart cities , internet-of-things (IoTs), wireless healthcare and environmental monitoring, and industrial 4.0, to name a few [1]-[3]. In most wireless sensing systems, a reader will transmit a continuous-wave signal to power up the passive tag and then intercept with the backscattered signal that is generally modulated by an integrated chemical or physical sensor tuning the input impedance of the antenna [4]-[7]. In such systems, the continuous-wave signal that powers the tags will be inevitably coupled

to the receivers, showing a strong self-interference, which poses a challenge to the design of the receivers. Further, these systems are relatively vulnerable to the surrounding reflections or noises, which also limits their applications in the rich-scattering indoor environment filled with clutters, echos, and crosstalks [8]-[10]. Most recently, nonlinear tracking and sensing techniques have begun to gain popularity because they have capability to eliminate these crosstalks between the receiver and transceiver antennas (i.e., $R_x$ and $T_x$), and the unwanted echoes and clutters from a surrounding noisy environment, which is schematically shown in Fig. 1 [11]-[14]. In contrast to the traditional passive wireless sensing systems, where the readers and sensors working at the same frequency band [15]-[17], the passive harmonic systems with nonlinear tags or harmonic transponders could receive the fundamental tone, modulating it, and then retransmitting a sub-harmonic signal (i.e., second harmonic) to the interrogator (Fig. 1) [18], [19]. Thanks to the orthogonality of the frequencies between the transmitted and backscattered signals, these harmonic sensor systems could remarkably suppress the electromagnetic interferences, including clutter and crosstalk [20], [21]. According to this concept, Huang et al have successfully demonstrated a battery-free harmonic sensing scheme for liquid detection in the healthcare applications. Their technique is on the basis of the received signal strength indicator (i.e., RSSI) data in the harmonic band and the frequency-hopping spread spectrum (i.e., FHSS) analysis [22]. Especially, this technique is extremely useful for interrogating electrically-small or low RCS signature sensors or tags typically suffering from the electromagnetic interferences in noisy environments, such as the indoor areas or dense urban.

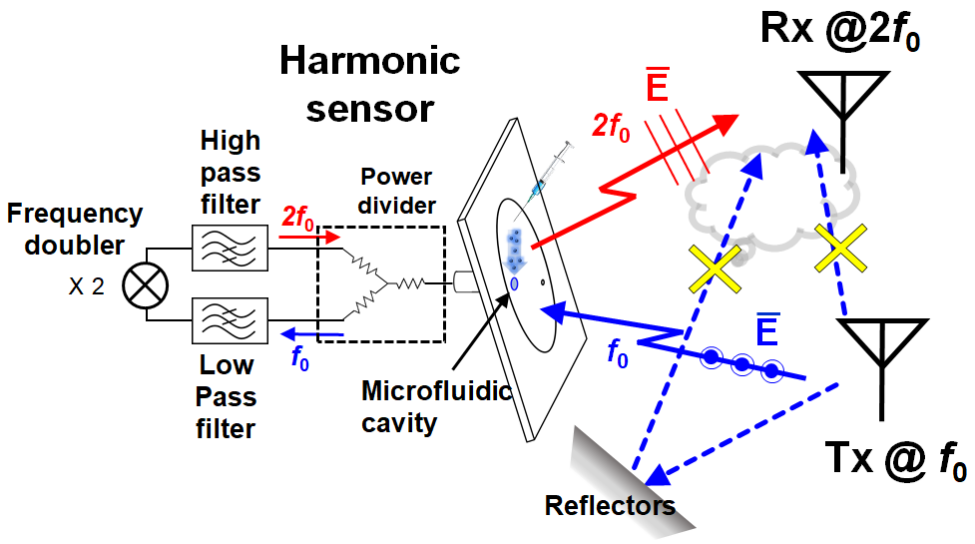


Figure 9. Schematics of the compact harmonic sensor based on the fluidic channel integrated, dual-resonance elliptical antenna connected to a diplexer and a frequency doubler. This sensor could receive and retransmit signals with orthogonal frequencies for suppressing clutter and cross talk.

Although theses harmonic-based wireless sensor systems have several advantages such as higher signal-to-noise ratio (SNR) and relatively longer interrogation distance, these sensors typically have two antennas integrated together to serve as the fundamental tone receiver and high/sub-harmonic frequencies re-transmitter, respectively [23], [24]. This structure, in turn, will inevitably increases the complexity in sensors' minimization and integration. Attempting to develop a compact and low-profile harmonic sensor, we proposed in this chapter a dual-resonance elliptical microstrip antenna, enabling a single feeding line but simultaneously excite the first even $TM_{e110}$ mode at $f_0$ and the first odd $TM_{o110}$ mode at $2f_0$, as shown in Fig. 1. Additionally, these two modes exhibit different polarizations that are perpendicular to each other, which reduces one more stage of interference. For making a compact harmonic tag, this single-feed microstrip patch antenna can be connected to the diplexer and frequency doubler. Except from the device miniaturization offered by the hybridization of the receiver and transmitter on tag ($R'_x$ and $T'_x$), the proposed

antenna could be readily loaded with extra sensing elements, forming a platform for a harmonic sensors. As an example, if a fluidic channel is mounted on this elliptical patch, the resonance of the $TM_{o110}$ mode will be sensitively detuned, while the resonant frequency of the $TM_{e110}$ mode may remain the same. In this case, the sensor will always receive the input signal at same frequency, whereas the output harmonic signal that is received by the reader could have a magnitude controlled by the dielectric properties or volume of the sample under test.

This chapter is organized as below. In Section 3.2, we first derive the analytical soluation for resonant modes and electric field distributions regarding the proposed dual-resonance antenna. In Section 3.3, we report the experimental results for the antenna, in terms of its impedance matching and also radiation performance. We will introduce a shorting-pin tuning approach to decouple the hybrid $TM_{e210}$ and $TM_{o110}$ modes, which can have similar resonant frequencies. We also demonstrate a fully-passive compact harmonic sensor consisting of the proposed microstrip antenna loaded with a fluidic channel, aiming for practical liquid monitoring in rich-scattering environments. At last, we draw a short conclusion.

### 3.2 Theoretical Modeling of Dual-Band Elliptical Patch Antenna

Figure 9 illustrates the geometry of the elliptical antenna with a major semi-axis length $a$ and minor semi-axis length $b$. This elliptical patch layer is separated from its ground plane by a FR4 substrate with the thickness $d$ = 1.5 mm, the relative permittivity $\varepsilon_r$ = 4.25, and the loss tangent $\delta$ = 0.015. The excited modes within the elliptical antenna could be computed by the cavity model with properly assigned boundary conditions [25], [26], i.e., a perfect electric conductor (PEC) boundary condition applied at the top and bottom, and a perfect magnetic conductor (PMC) assumed on the sidewalls. Under this assumption, Maxwell's equations is reduced to the following set of formulas in the elliptical coordinates ($\xi$, $\eta$) [27], [28]:

$$
\begin{aligned}
&\frac{1}{c^2(\cosh^2\xi-\cos^2\eta)}\left(\frac{\partial^2 E_z}{\partial\xi^2}+\frac{\partial^2 E_z}{\partial\eta^2}\right)+k^2E_z=0,\\
&H_\xi=j\frac{1}{\omega\mu c(\cosh^2\xi-\cos^2\eta)^{1/2}}\frac{\partial E_z}{\partial\eta},\\
&H_\eta=-j\frac{1}{\omega\mu c(\cosh^2\xi-\cos^2\eta)^{1/2}}\frac{\partial E_z}{\partial\xi},\\
&H_z=0,\ E_\xi=0,\ \text{and } E_\eta=0.
\end{aligned}
\tag{3}
$$

Therefore, the electric field in this elliptical cavity could be expanded in the format of elliptical wave functions:

$$
\begin{aligned}
E_{e,z}(\xi,\eta)&=\sum_{n=0}^{n=\infty}M_{e,n}^{(1)}(\xi,q)C_{e,n}(\eta,q),\\
E_{o,z}(\xi,\eta)&=\sum_{n=1}^{n=\infty}M_{o,n}^{(1)}(\xi,q)S_{e,n}(\eta,q),
\end{aligned}
\tag{4}
$$

where $q=c^2k^2/4$, $k=\omega\sqrt{\varepsilon_r\varepsilon_0\mu_0}$, $c=\sqrt{a^2-b^2}$, $\varepsilon_0$ and $\mu_0$ are free space permittivity and permeability, $M_{e,n}^{(1)}(\xi,q)$ and $M_{o,n}^{(1)}(\xi,q)$ are the even and odd radial Mathieu functions of the first kind, respectively, $n$ is the order of the angular Mathieu functions $C_{e,n}(\eta,q)$ and $S_{e,n}(\eta,q)$, which is used for determining the azimuthal variation [29], [30]. By matching the aforementioned boundary conditions at the magnetic wall $\xi=\xi_0$, the transcendental equations are derived as:

$$
\begin{aligned}
&M_{e,n}'^{(1)}(\xi_0,q)=0 \quad \text{for } n\text{-th even mode}\\
&M_{o,n}'^{(1)}(\xi_0,q)=0 \quad \text{for } n\text{-th odd mode}
\end{aligned}
\tag{5}
$$

After solving these transcendental equations (Eq. (5)), if $\xi_0 = 0.497$ is chosen, i.e., $b/a = 0.46$, the first $TM_{e110}$ mode and the $TM_{o110}$ mode could be excited at $f_0$ and $2f_0$, respectively, as can be seen

in Fig. 10. When designing an elliptical patch antenna for harmonic transponders or sensors, one should decide a major semi-axis length $a$ first, ensuring a resonance at $f_0$ with $TM_{e110}$ mode. Then,

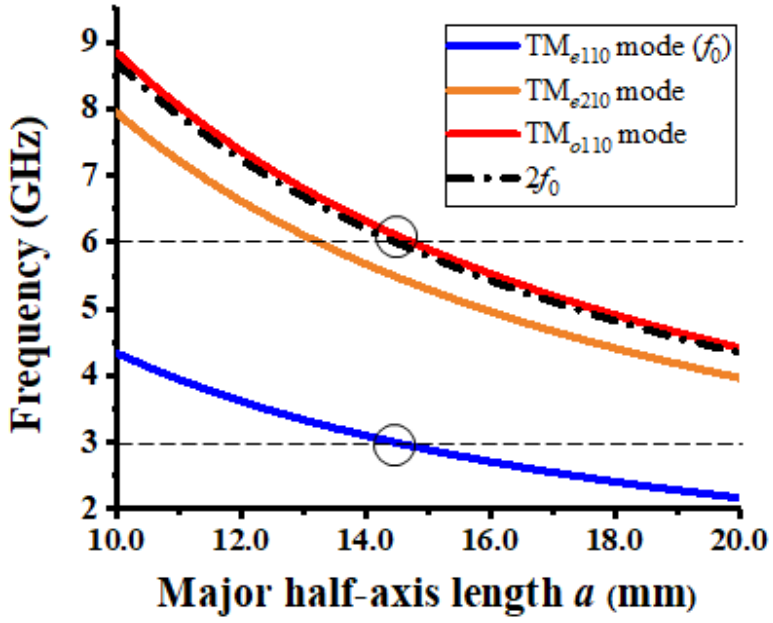


Figure 10. Resonant frequencies of the elliptical patch antenna for different modes.

the minor semi-axis length $b$ will be automatically determined by Eq. (5), since $b = 0.46a$ is required, achieving a resonance at $2f_0$.

### 3.3 Fabrication and measurement results

#### 3.3.1 Dual-resonant elliptical microstrip antenna without shorting pins

We have manufactured an elliptical patch antenna using printed-circuit board technique, with the FR4 substrate and the copper microstrips. Fig. 11(a) presents the fabricated dual-resonance elliptical antenna with some important design parameters as: $a = 14.4$ mm, $b = 6.336$ mm, and a 50 ohms feeding point is located at coordinate $x = -3$ mm, $y = -3.5$ mm. By suitably designing the

feeding position, one can simultaneously excite these $TM_{e110}$ and $TM_{o110}$ modes, yielding a orthogonal, linearly-polarized far-field radiation.

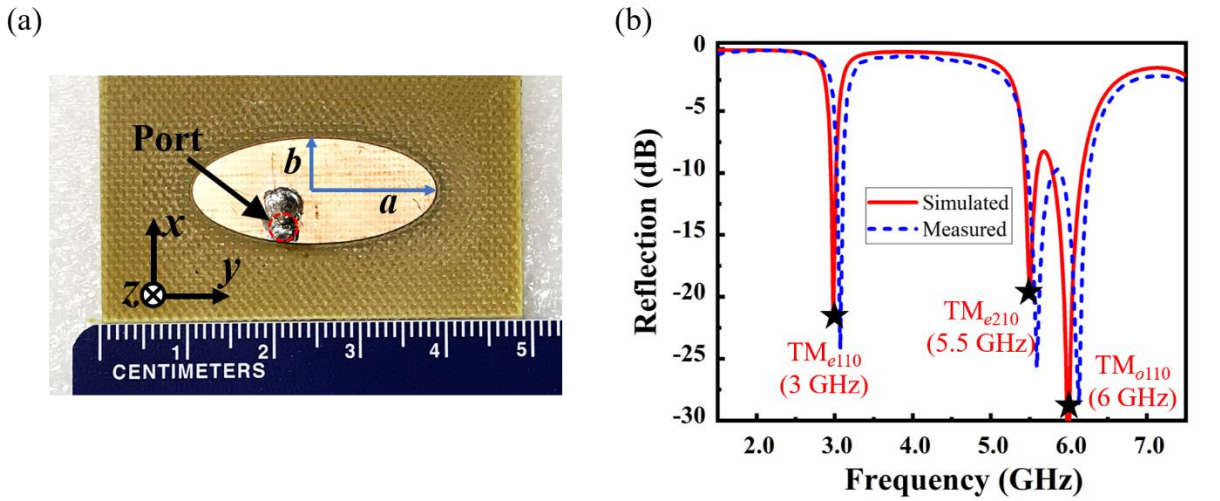


Figure 11. (a) Photograph of the dual-resonance elliptical antenna. (b) The simulated and measured reflection coefficient of the elliptical antenna. Note that the solid and dash lines respectively represent the simulated and measured results.

Fig. 11(b) shows the measured and simulated [31] reflection coefficients ($S_{11}$) for the microstrip antenna in Fig. 11(a). It can be seen that these results are in good agreement, with noticeable dips at 3 GHz and at 6 GHz, respectively, confirming the proposed dual-resonance behaviors of this elliptical structure. In addition, a good impedance matching is received, with the –10 dB bandwidth of 80 MHz at the center frequency of 3.07 GHz and of 350 MHz at the center frequency of 6.13 GHz, which are closed to the simulated results, i.e., 70 MHz and 380 MHz, respectively .

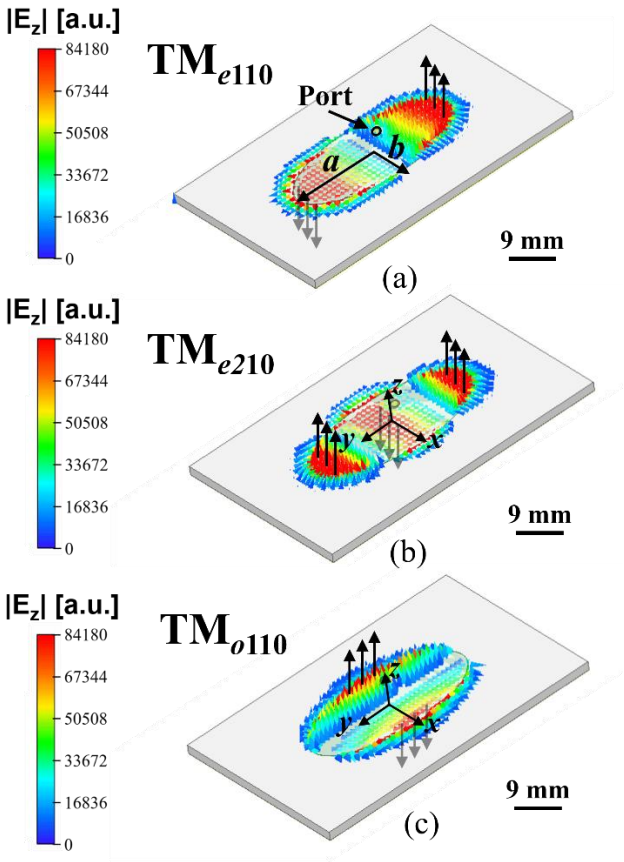


Figure 12. Snapshots of electric field distributions for (a) $TM_{e110}$ mode at 3 GHz, (b) $TM_{e210}$ mode at 5.5 GHz and (c) $TM_{o110}$ mode at 6 GHz of the proposed dual-resonance elliptical antennas.

Figs. 12(a) and 12(c) respectively present the simulated snapshots of electric field distributions of $TM_{e110}$ and $TM_{o110}$ modes. These field profiles agree quite well with the assumption mad by the cavity model. Here, we should note that a extra mode, i.e., $TM_{e210}$ mode is also excited in the vicinity of the $TM_{o110}$ mode. Such a higher-order mode must be suppressed or detuned, to avoid the potential modal coupling that could deteriorate the sensing sensitivity. Toward this goal, a simple but effective solution is to insert shorting-pin loads inside this elliptical cavity to redshift the $TM_{e210}$ mode, which will be discussed in the next section.

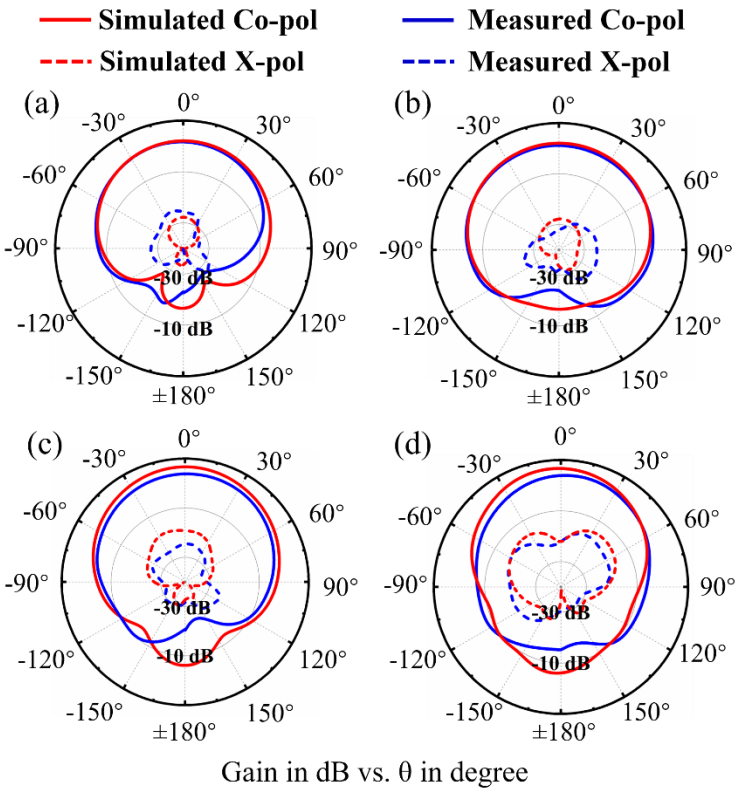


Figure 13. Radiation patterns of the dual-resonance patch antenna, with (a), (b) for the E-plane (y-z plane) and the H-plane (x-z plane) at 3 GHz, and (c), (d) for the E-plane (x-z plane) and the H-plane (y-z plane) at 6 GHz.

Fig. 13 presents the measured and simulated radiation patterns of this elliptical patch antenna on the E- and H-planes at two resonant frequencies (3 GHz and 6 GHz). Here, the E- and H-planes for the $TM_{e110}$ ($TM_{o110}$) modes are respectively referring to *y-z* and *x-z* (*x-z* and *y-z*) planes. A broadside radiation pattern is observed for both modes, agreeing well with the simulation results. At 3 GHz under $TM_{e110}$ mode, this elliptical patch exhibits a maximum gain of 2.66 dBi and a half-power beamwidth (HPBW) of 92° on the E-plane and 106° on H-plane. At 6 GHz under $TM_{o110}$ mode, the antenna displays a maximum realized gain of 4.84 dBi, and a HPBW of 84° (66°) on the E-plane (H-plane). A high co-polarization was apparently seen, with a cross-polarization < -20 dB

(–10 dB) on the E-plane (H-plane), respectively. Here, it should be noted that due to the relatively high dielectric losses of the FR4 substrate, the radiation efficiencies are 45% at 3 GHz and 83% at 6 GHz. The efficiency discrepancy may be explained as follows. As we know, the efficiency of microstrip antennas will decrease with the increase of the substrate thickness or permittivity due to the potential loss related to the surface waves. On the other hand, the efficiency may also be decreased if the substrate becomes too thin because of the more severe dielectric loss caused by the stronger localized electric field in thinner substrate [32], [33]. This could help explain the radiation efficiency difference in the 3 GHz band and that in the 6 GHz band, as the thickness of the substrate versus the operating wavelength decreases, and therefore, resulting in a relatively high dielectric loss within the microstrip cavity. We also note that this issue can be mitigated by using a high-quality PCB substrate with a smaller loss tangent.

### 3.3.2 Elliptical microstrip antenna loaded with shorting pins

Even though the proposed dual-resonance elliptical patch antenna has good impedance matching and radiation properties at the frequencies of interest, the spectral overlap must be mitigated. Typically, it is impossible to directly decouple the $TM_{e210}$ and $TM_{o110}$ modes by simply varying the antenna shape or dimension. Therefore, we propose a shorting pin method to perturbate the antenna geometry, so as to decouple these two modes. It is known that inserting shorting pin (i.e., vias) inside the antenna cavity can perturb the current distributions on the microstrip antenna, which has been developed for designing dual-band patch antennas [34]-[36] or for miniaturizing the dimension of microstrip antenna [37]-[39]. Fig. 14(a) shows the proposed structure, in which two shorting pins are placed on the major axis of the patch. The dimension of this perturbated elliptical patch is slightly modified as $a$ = 19.5 mm and $b$ = 6.63 mm, in order to obtain a fixed

resonant frequencies. We have swept the separations between the two shorting vias along the *y*-axis. The simulated

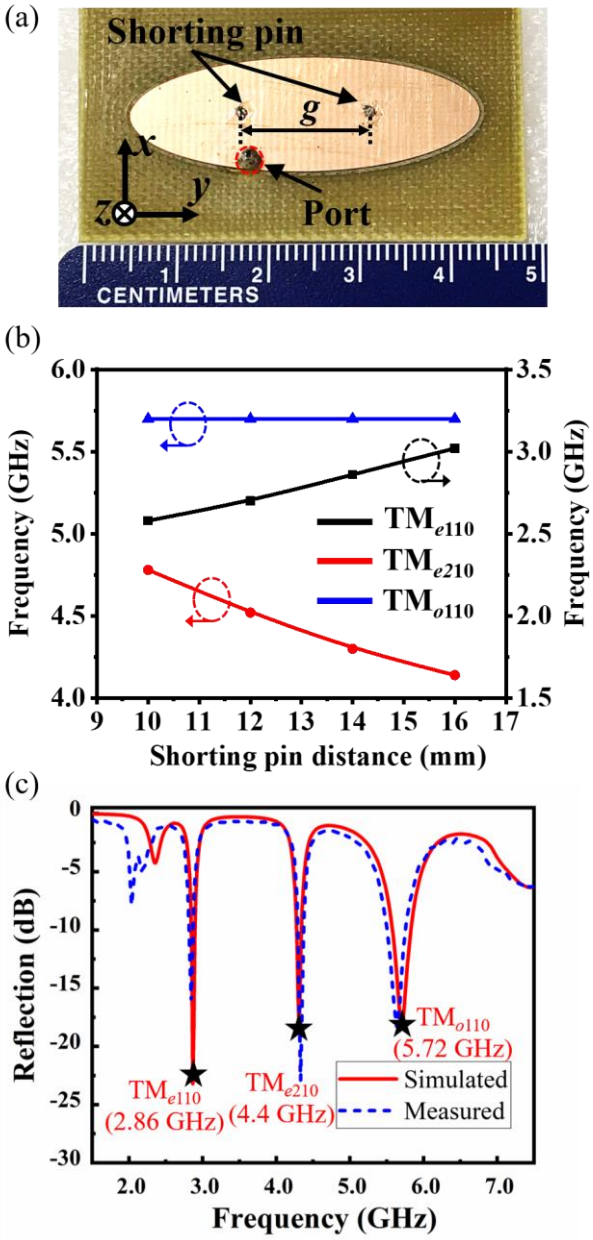


Figure 14. (a) Photograph of the dual-resonance elliptical antenna perturbated with two shorting vias. (b) Resonant frequencies of the proposed antenna in response to different distance *g*. (c) Simulation and measurement reflection coefficients of the antenna.

resonant frequencies for three modes, i.e., $TM_{e110}$, $TM_{e210}$ and $TM_{o110}$, are illustrated in Fig. 14(b). It can been obviously seen that increasing the gap between two shorting pins, the resonances of $TM_{e110}$ mode will be upshifted from 2.58 GHz to 3.02 GHz, whereas that of the $TM_{o110}$ will remain unchanged. Interestingly, the resonance of the $TM_{e210}$ mode will be downshifted from 4.78 GHz to 4.14 GHz, so that the $TM_{o110}$ and $TM_{e210}$ could be further separated from each other. The existence of these shorting pins along *y*-axis can only affect electric field distributions of the $TM_{e210}$ and $TM_{e110}$ (see Fig. 4), resulting in the resonance frequency offsets, but has no effects on the $TM_{o110}$ mode. In fact, increasing the separation gap between the two shorting vias will shorten the $TM_{e110}$ mode's current path, while it enlarges the current path of $TM_{e210}$ mode. Consequently, introducing the shorting-pins would upshift the frequency related to $TM_{e110}$ mode, whereas downshifting that of the $TM_{e210}$ mode in the spectrum. On the other hand, as the electrical field of the $TM_{o110}$ mode is keeping null on the plane with $x = 0$, implying that the two shorting pins will have no effects on current distribution and also center frequency of the $TM_{o110}$ mode.

According to the results obtained in Fig. 14(b), we have refined the elliptical patch with a decoupled $TM_{o110}$ and $TM_{e210}$ modes, with the important design parameters as: $a$ = 19.5 mm, $b$ = 6.63 mm, $g$ = 14 mm and the radius of shorting pin $r_{pin}$ = 0.4 mm. Figs. 14(a) and 6(c) present the photograph of the fabricated microstrip antenna and its reflections. It is evidently seen that introducing the shorting pins could effectively isolate the $TM_{e210}$ and $TM_{o110}$ modes. Nevertheless, a dual-resonance (i.e., $f_0$ = 2.86 GHz and $2f_0$ = 5.72 GHz) can be still achieved in refined elliptical

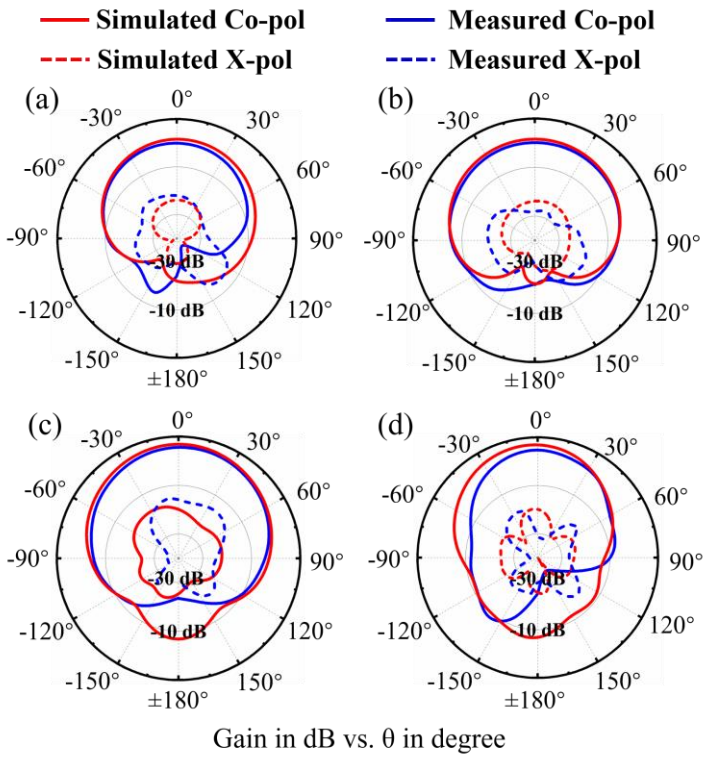


Figure 15. Simulated and measured radiation patterns of the refined elliptical antenna.

antenna. The measured impedance bandwidth is 50 MHz with the center frequency at 2.845 GHz , and is 270 MHz at the center frequency of 5.65 GHz, which agree well with the simulation results. Fig. 15 reports the measured radiation patterns of this antenna on both E- and H-planes at 2.86 GHz and 5.72 GHz. We find that introducing the shorting pins will not affect the radiation properties and co- or cross-polarization of the elliptical patch. At 2.86 GHz, the antenna displays a maximum gain of 1.55 dBi, with a HPBW of 85° on the E-plane and 120° on the H-plane. At 5.72 GHz, the antenna shows a maximum realized gain of 6.7 dBi, with the HPBW of 80° (55°) on the E-plane (H-plane), respectively. Note that the measured cross-polarization radiation pattern is still less than –15 dB (–15 dB) on the both planes. Moreover, the radiation efficiency is 43% at 2.86 GHz and 83% at 5.72 GHz, even comparable to the one of the unperturbed elliptical patch. It should be noted that inserting

the shorting pins into the antenna cavity could also be visualized as a resistive perturbation, which will inevitably increase the conduction loss a bit and reduce the overall radiation efficiency of the corresponding mode. On the other hand, since the position of the pins are located in the null field region of the $TM_{o110}$ mode at 5.72 GHz, it will not affect the radiation efficiency of this mode.

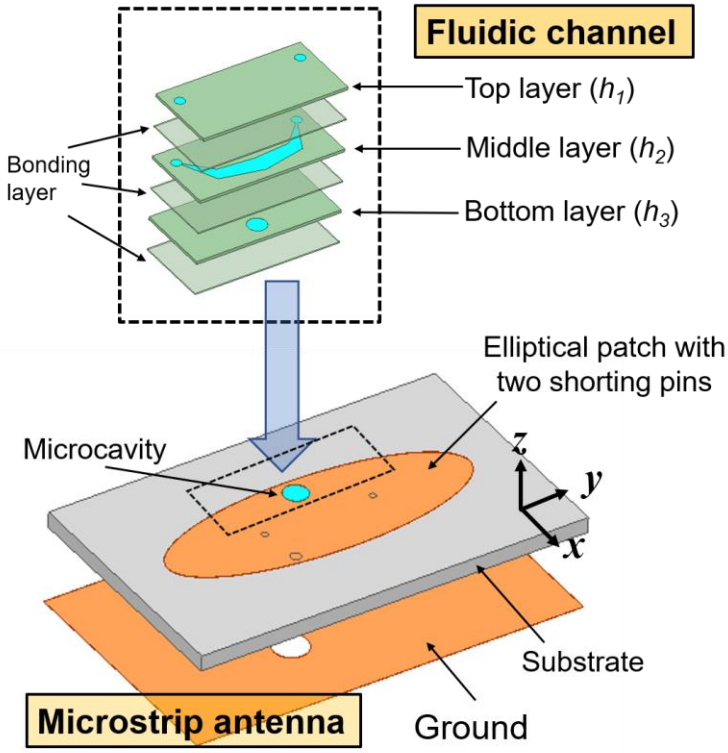


Figure 16. Schematic of the harmonic sensor comprising the dual-band elliptical patch and an integrated acrylic based fluidic channel.

### 3.4 Practical Wireless Mixture Monitoring

#### 3.4.1 Dual resonance elliptical harmonic transponder

Next, we developed a harmonic sensor prototype that combines this dual-resonance microstrip antenna and an acrylic fluidic channel, as schematically illustrated in Fig. 16. A liquid cavity with

radius $r_{tank}$ = 1.5 mm is designed and located at position with coordinate $x$ = 5 mm and $y$ = 0 mm, and the important parameters of the fluidic channel is $L$ = 25 mm, $W$ = 12 mm with the height of three layers as $h_1$ = 1 mm, $h_2$ = 1 mm and $h_3$ = 0.1 mm, respectively. We should emphasize that at the center of the fluidic tank, the resonant mode of $TM_{o110}$ would exhibit a localized electric field, while the resonant mode of $TM_{e110}$ has nearly null electric field. Therefore, according to the perturbation theory [40], [41], if the dielectric properties of the fluidic channel is varied, the resonance frequency of $TM_{o110}$ mode (at $2f_0$) will experience a relevant shift, owning to the strong electric fields localized at the liquid reservoir region. However, the $TM_{e110}$ mode at $f_0$ could remain the same due to the null electric field at that region, where this liquid reservoir is located. Fig. 17 reports the photograph of the manufactured harmonic sensor with a fluidic channel connected to two liquid tubes for guiding medium in and out, respectively.

Fig. 18 reports the measured reflection coefficients for this antenna sensor, exhibiting three dominant modes at 2.86 GHz ($TM_{e110}$), 4.4 GHz ($TM_{e210}$), and 5.76 GHz ($TM_{o110}$), respectively. From Fig. 18, we find that the existence of this fluidic channel would slightly shift the resonant frequency of the $TM_{o110}$ mode to 5.76 GHz. Nevertheless, it still has a sufficient bandwidth to cover the second-harmonic band. Fig. 19 reports the measured radiation patterns of the fluidic channel loaded antenna on the E- and H-planes at both 2.86 GHz and 5.76 GHz, exhibiting a quite similar broadside radiation property as before without fluidic channel. This antenna has a maximum realized gain of 0.7 dBi at 2.86 GHz, with a HPBW of 85° on the E-plane and 110° on H-plane. When compared to the elliptical antenna without fluidic channel loading (1.55 dBi), this realized gain is slightly decreased because of the errors in fabrication and also package. At 5.76 GHz, this antenna displays a maximum realized gain of 6.5 dBi, with the HPBW of 90° and 50° on the *E*-plane and H-plane, respectively.

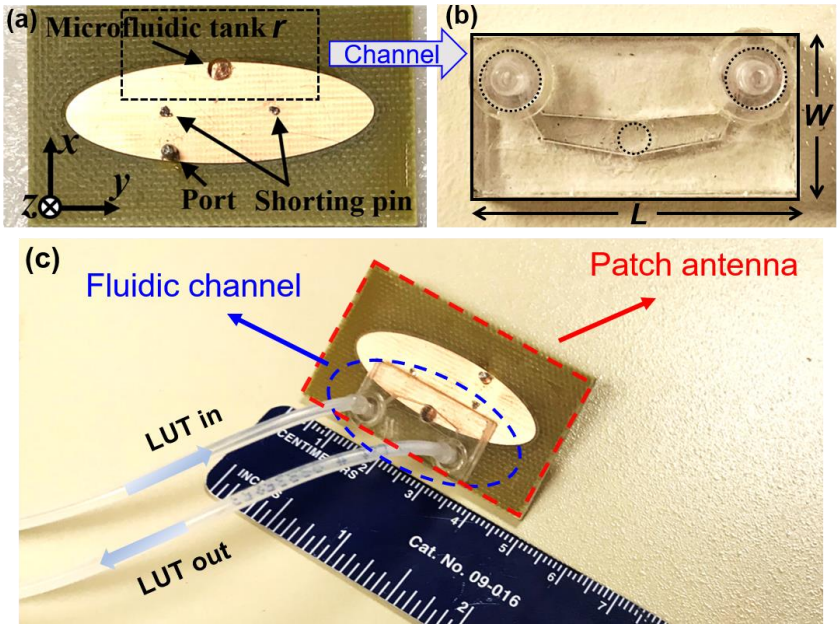


Figure 17. Photograph of the dual-resonance elliptical patch antenna integrated with a fluidic channel.

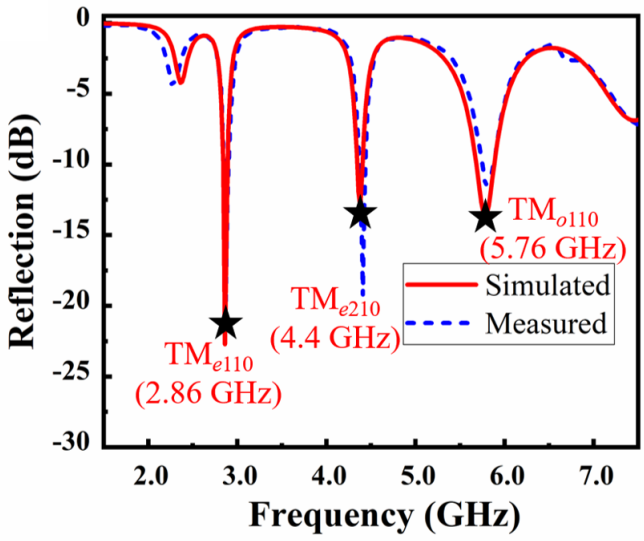


Figure 18. The reflection coefficient of the antenna in Fig. 17.

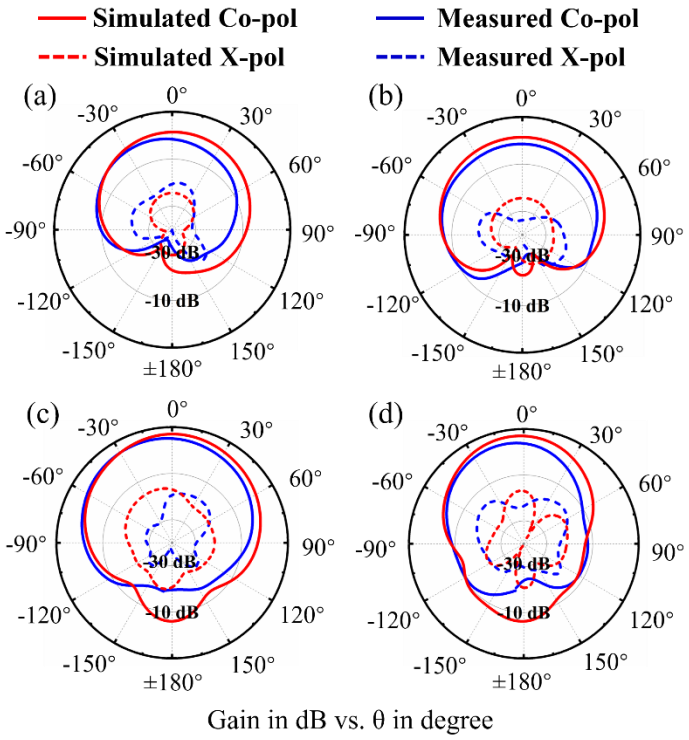


Figure 19. Radiation patterns of the dual-resonance elliptical patch antenna integrated with fluidic channels.

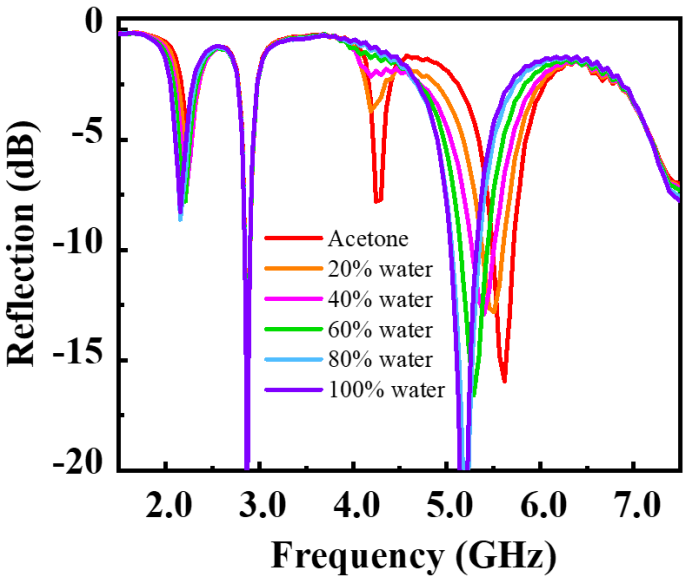


Figure 20. Measured reflection coefficients of this harmonic sensor that comprises the microstrip antenna injected with acetone and water mixtures at various concentrations.

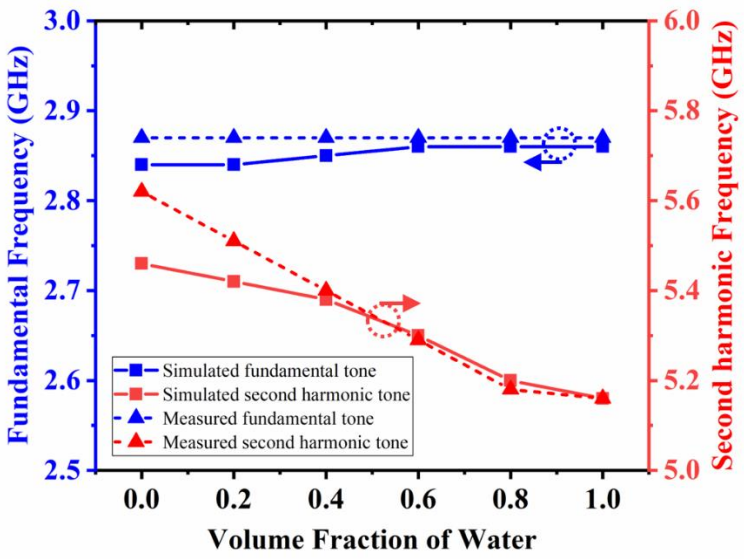


Figure 21. Measured and simulated frequency responses for the elliptical patch antenna in response to different volume fraction of water injected in the fluidic channel.

### 3.4.2 Binary liquid mixture measurement

In this section, the harmonic sensor is used for the practical wireless monitoring of concentration and dielectric properties of the acetone-water mixtures. For this purpose, acetone and water mixtures at different concentrations were prepared with their complex effective permittivities summarized in Table I.

Table I: Complex permittivities of various acetone-water mixtures.

| Mixtures | 0 % (acetone) | 20% | 40% | 60% | 80% | 100 % (water) |
|---|---|---|---|---|---|---|
| $\varepsilon'_r$ | 20.7 | 25 | 35 | 45 | 66 | 80 |
| $\varepsilon''_r$ | 0.5 | 1 | 1.65 | 2.5 | 4.3 | 6 |

Such effective relative permittivity $\varepsilon_r$ could be computed by the formula related to different mixtures [42], [43], given by:

$$\varepsilon_r = \varepsilon_{acetone}\left[\frac{(2\varepsilon_{acetone}+\varepsilon_{water})+2V_f(\varepsilon_{water}-\varepsilon_{acetone})}{(2\varepsilon_{acetone}+\varepsilon_{water})-V_f(\varepsilon_{water}-\varepsilon_{acetone})}\right] \quad (6)$$

where $\varepsilon_{water}$ [43] and $\varepsilon_{\text{acetone}}$ [44] are respectively the complex permittivities of the water and acetone, and $V_f$ is the volume fraction of water solution in the mixture. Fig. 20 decribes the measured reflection coefficients in response to different acetone/water mixtures, showing that increasing the dielectric constants of the mixture, namely, effectively decreasing the volume ratio of acetone to water, can shift the frequency of $TM_{o110}$ resonant mode from 5.64 to 5.16 GHz,

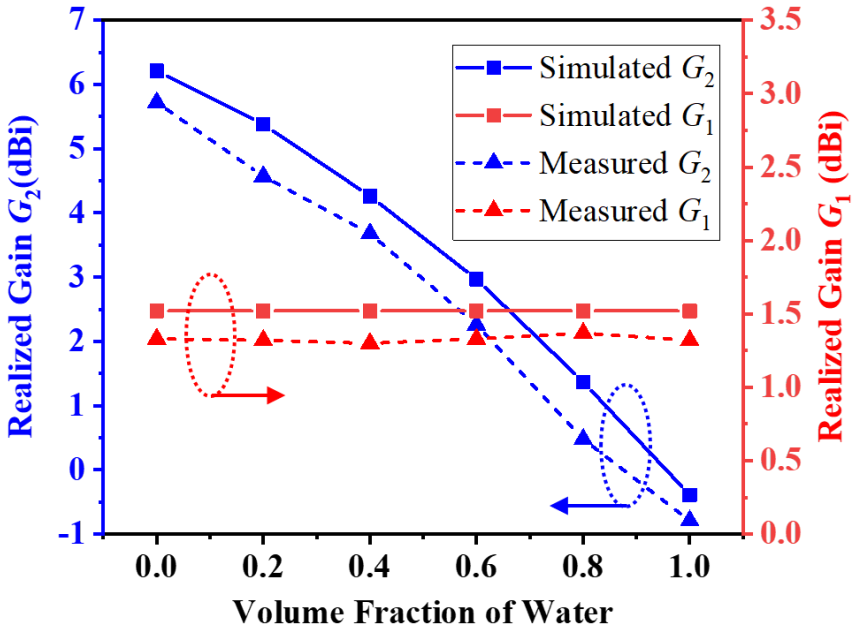


Figure 22. The simulated and measured realized gain of the dual-resonance harmonic sensor at 2.86 GHz (G1) and 5.72 GHz (G2).

while the resonant frequency of the $TM_{e110}$ mode is rather unchanged around 2.86 GHz. Based on these results, Fig. 21 concludes the resonance frequency shifts with regard to the $TM_{e110}$ and $TM_{o110}$ modes, in response to different volume fraction of water. Apparently, the proposed harmonic sensor exhibits good linearity and sensitivity for measuring the liquid concentrations, and a good agreement could be achieved between the measured and simulated results. Moreover, we have measured the realized gain of this elliptical patch as a function of different volume fractions of water, and the results are shown in Fig. 22. The small discrepancy between the experimental and simulated results can be attributed to the errors in the fabrication or assembly processes, and the fluctuations of the substrate permittivity. It can be seen clearly that the gain $G_2$ at 5.72 GHz would decrease dramatically from 5.8 dBi to –0.7 dBi, when the type of mixture is varied from pure acetone (0 %), to acetone-water mixture (20 % - 80 %), and at last, to pure water (100 %), whereas the gain $G_1$ at 2.86 GHz is still fixed to 1.33 dBi. Such results suggest that the incident RF signal would have a constant strength, while the output second harmonic tone could be detuned by different density of the mixtures.

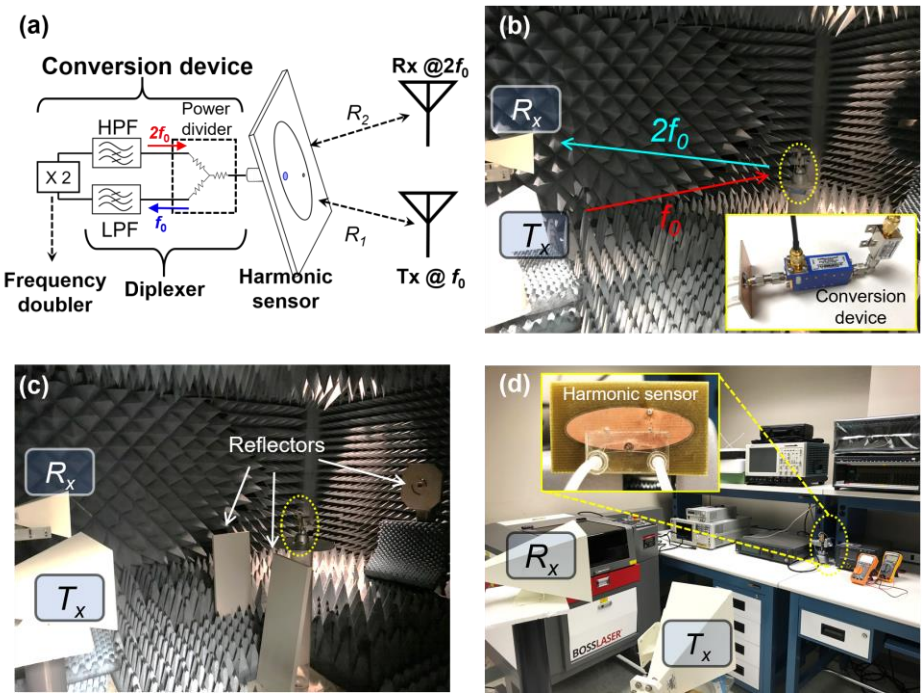


Figure 23. Measurement configuration for characterizing the harmonic sensor and the conventional linear backscatter sensor.

Next, we consider a battery-free harmonic sensor prototype formed by the fluid-integrated, dual-band patch antenna, a diplexer [45] and a frequency multiplier [46]. In our configuration, the bistatic setup is used for telemetry (see Fig. 23(a)). First, the harmonic sensor was measured inside the anechoic chamber without any multipath reflection, removing all the effects in terms of clutters, echoes, and multipath reflections, as illustrated in Fig. 23(b). Next, some metal reflectors were intentionally introduced in the vicinity of the harmonic sensor, for testing its immunity to clutter and echo noises (Fig. 23(c)). In Fig. 23(d), we repeat this measurement in a rich-scatting indoor environment full of electromagnetic interferences. In general, regarding this setup, the transceiver launched a continuous wave fundamental signal to the under test harmonic sensor. Later, the backscattered second harmonic tone, whose strength is determined on the concentration of the

mixture injected into the fluidic channel, would be recorded and analyzed by the receivers. According to the Friis' transmission formula [47], the power ratio of the second harmonic to the transmitted fundamental tone is given by:

$$\frac{P_r}{P_t} = \left(\frac{\lambda_0}{4\pi R_1}\right)^2 \left(\frac{\lambda_0 / 2}{4\pi R_2}\right)^2 \frac{G_1 G_2 G_T G_R}{L_{sys}} \tag{7}$$

where $G_T$ and $G_R$ are respectively the antenna gain of the $T_x$ and $R_x$, $G_1$ and $G_2$ are the gain of the receiving and re-transmitting modes of the harmonic sensor, $R_1$ is the distance between the $T_x$ and the sensor, $R_2$ is the distance between the $R_x$ and antenna sensor, $L_{sys}$ is the overall system loss primarily due to the conversion loss of frequency multiplier, the return and insertion losses of diplexer, and some other factors such as cable losses. From Fig. 22, we find that the realized gain $G_1$ that is associated with the signal strength of the fundamental tone, keeps almost constant, while the realized gain $G_2$ that is related to the second harmonic signal, decreases linearly with the reduction of the acetone concentration. Such measurement results suggest that the RSSI at the second-harmonic frequency will gradually diminish and can ultimately vanish if keeping reducing the acetone concentration, as shown in Fig. 24.

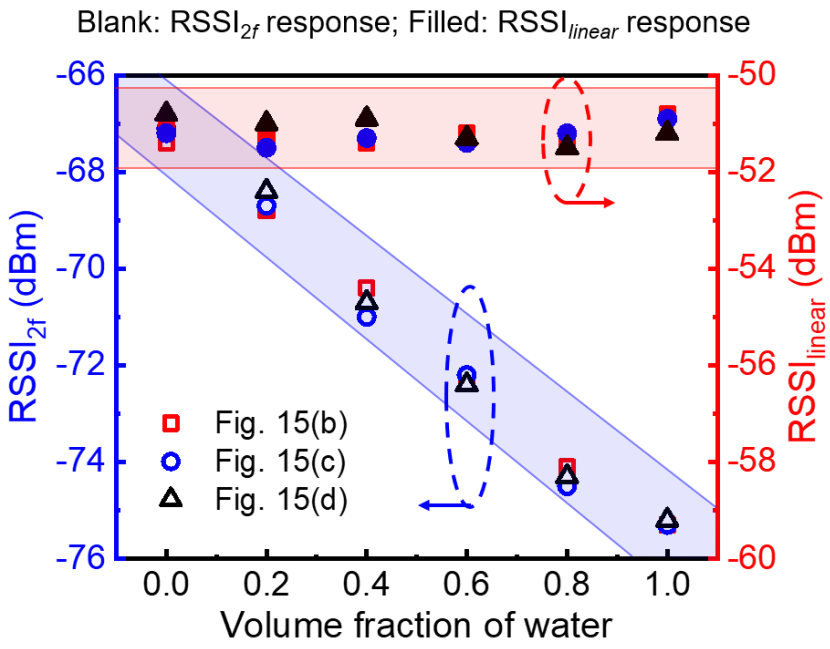


Figure 24. The measured RSSI of the proposed harmonic sensor (blue zone) and a conventional passive backscatter sensor (red zone).

In this measurement, the important setup parameters are: $P_t$ = 25 dBm, $R_1$ = $R_2$ = 1.2 m, $G_T$ = 17.5 dBi at 2.86 GHz, $G_R$ = 19.5 dBi at 5. 72 GHz and $L_{doubler}$ is around 20 dB at a 0 dBm input power level. Furthermore, for making a fair comparison, we also utilized the linear interrogating approach , namely, using a traditional passive backscatter wireless sensor, to readout the same antenna sensor. In this manner, our elliptical antenna is disconnected from the frequency multiplier, but instead, connected to a 50 ohm match load. The measured backscattered signal at 5.72 GHz is presented also in Fig. 24, from which it can be seen obviously that in the conventional linear interrogating scheme without the frequency conversion devices, even though the antenna is still modulated by the mixture, the backscattered responses could hardly be recognized under different dielectric materials, ascribed to the existing electromagnetic interferences sourced from crosstalks

between $T_x$ and $R_x$ antennas and also environmental clutters. By contrast, the passive harmonic sensor based on the proposed dual-resonance, dual-polarization microstrip antennas could provide a more robust and reliable far field sensing performance in all scenarios, compared with conventional linear backscatter sensors/tags. We should emphasize that the application of this harmonic sensor is not limited to sensing acetone/water mixtures, but can be generalized to identification of any type of aqueous solution/mixture (e.g., ethanol, glucose, oil, etc) in chemical, biological and environmental monitoring systems. The interrogating distance can be further increased by utilizing an active frequency doubler with a conversion gain [48].

Here, we also validate the repeatability and the continuity of our harmonic sensing platform by performing a real-time measurement in the rich-scattering environment. In this measurement, different acetone-water mixtures (different concentration) were injected into the fluidic channel every 80 seconds, with the interval of 20 seconds for empty state as a reference. The experimental results shown in Fig. 25(a) exhibit a good robustness and sensitivity, as well as the capability to performance the real-time wireless sensing. We also find that from Fig. 25(a), after the injection of different acetone and water mixtures, the harmonic sensor with the amplitude modulation could always be reset to the initial state, i.e., the state with a peak RSSI value of –64 dBm. In Fig. 25(b), the pure water sample was injected in the fluidic channel with the random time intervals, presenting that the existence of solution could effectively modulate the RSSI between “0” and “1” that is received in the far zone, while the conventional backscatter one fails to elaborate. It should be also noted that the proposed elliptical antenna can be even integrated with a more sophisticated microfluidic-channel network and be further miniaturized by adopting coplanar diplexer and frequency multiplier.

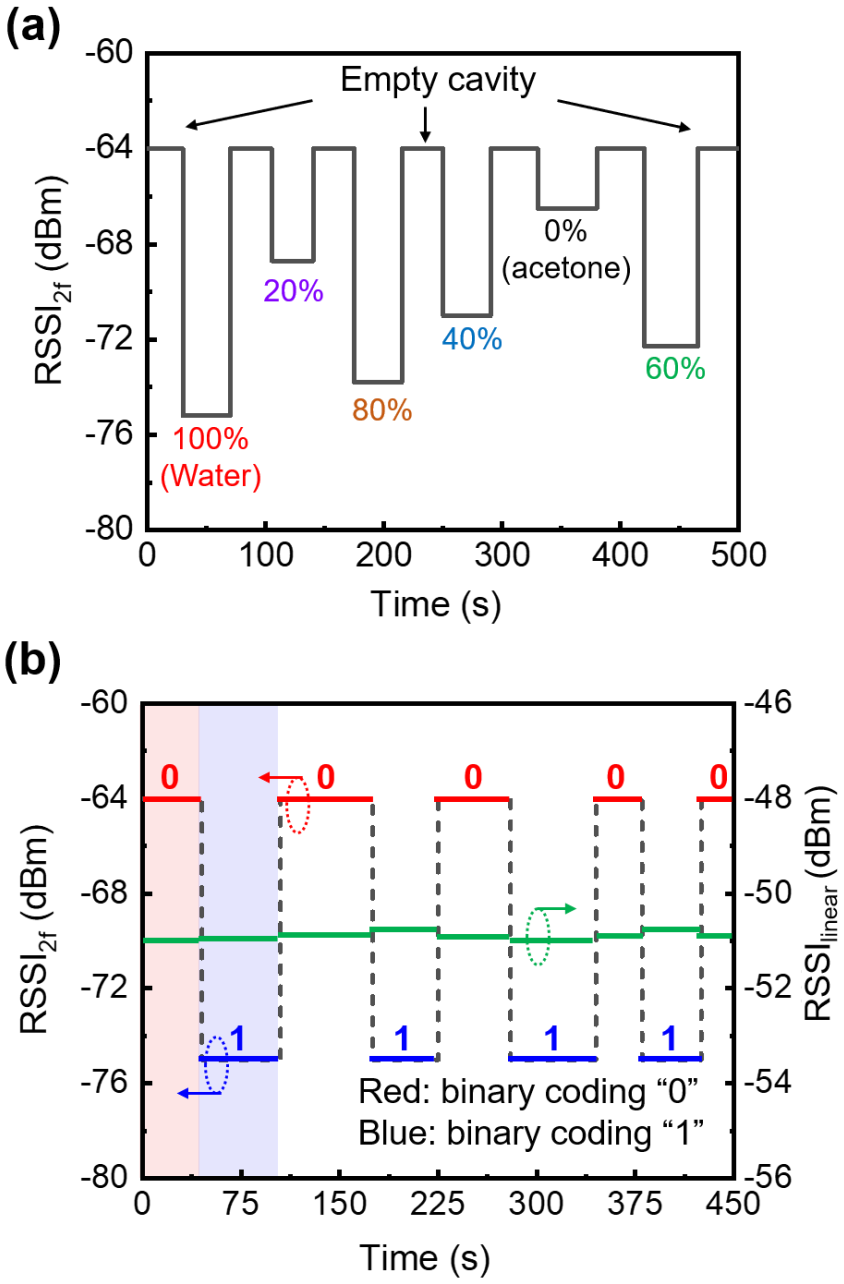


Figure 25. Real-time results of the proposed harmonic sensor in response to (a) different acetone and water mixture for wireless sensing, and (b) pure water solution for binary coding with "0" and "1".

## 3.5 Conclusion

We have introduced a compact elliptical microstrip patch antenna for harmonic sensing applications that demand dual resonance excited simultaneously at the fundamental frequency ($f_0$) and second-harmonic frequency ($2f_0$). Specifically, we have studied an elliptical patch perturbated with shorting vias, thereby exhibiting an even order $TM_{e110}$ mode at $f_0$ and an odd order $TM_{o110}$ resonant mode at $2f_0$, not coupling to the rest higher-order modes. Moreover, these two operating modes have been demonstrated with the orthogonal linear polarizations, further minimizing the background electromagnetic interferences. We have also integrated this dual-resonance antenna with a fluidic channel, and developed a harmonic liquid sensor, which could successfully detect different concentration of the acetone-water mixtures, without being interrupted by multiple scattering generated from the surrounding clutters. This compact, dual-resonance antenna and its usage for the development of battery-free, clutter-immune harmonic liquid sensing platforms show great potential in remote sensing of moisture, humidity and also other physiological factors, which may have diverse applications in environmental, industrial and also wearable healthcare areas.

## REFERENCES


[1] J. Zhang, G. Y. Tian, A. M. J. Marindra, A. I. Sunny, and A. B. Zhao, "A review of passive RFID tag antenna-based sensors and systems for structural health monitoring Applications," *Sensors,* vol. 17, no. 265, 2017.

[2] X. L. Jia, Q. Y. Feng, T. H. Fan, and Q. S. Lei, "RFID technology and its applications in Internet of Things (IoT)," in *2012 2nd Int. Conf. Consum. Electron, Commun. Netw,*, China, 2012.

[3] S. Z. Chen, H. Xu, D. Liu, B. Hu, and H. C. Wang, "A vision of IoT: Applications, challenges, and opportunities with China perspective," *IEEE Internet Things J.,* vol. 1, no. 4, pp. 349-359, 2014.

[4] A. Vena, L. Sydanheimo, M. M. Tentzeris, L. Ukkonen, "A fully inkjet-printed wireless and chipless sensor for $CO_2$ and temperature detection." *IEEE Sens. J.* 2014, 15, 89–99.

[5] L. Yang, R. Zhang, D. Staiculescu, C. P. Wong, M. M. Tentzeris, "A novel conformal RFID-enabled module utilizing inkjet-printed antennas and carbon nanotubes for gas-detection applications," *IEEE Antennas Wireless Propag. Lett.* 2009, 8, 653-656.

[6] B. S. Cook, J. R. Cooper, M. M. Tentzeris, "An inkjet-printed microfluidic RFID-enabled platform for wireless lab-on-chip applications." *IEEE Trans. Microw. Theory Tech.,* 2013, 61 (12), 4714-4723.

[7] W. Su, B. S. Cook, Y. Fang, M. M. Tentzeris, "Fully inkjet-printed microfluidics: a solution to low-cost rapid three-dimensional microfluidics fabrication with numerous electrical and sensing applications," *Scientific Reports,* 2016, 6, 35111.

[8] P. Y. Chen, H. Huang, C. H. Hung, "Compact metamaterial-enclosed wireless sensors with subtle perception of internal physical events," *Appl. Phys. Lett.*, vol. 107, 194101, 2015.

[9] P. Y. Chen et al., "Generalized parity–time symmetry condition for enhanced sensor telemetry, " *Nature Electron.*, vol. 1, no. 5, p. 297, May 2018.

[10] M. Hajizadegan, M. Sakhdari, S. Liao, and P. Y. Chen, "High-sensitivity wireless displacement sensing enabled by PT-symmetric telemetry, " *IEEE Trans. Antennas Propag.*, vol. 67, no. 5, pp. 3435–3449, 2019.

[11] J. R. Riley, A. D. Smith, D. R. Reynolds, and A. S. Edwards, "Tracking bees with harmonic radar," *Nature,* vol. 379, pp. 29-30, 1996.

[12] H. Y. Huang, L. Tao, F. Liu, L. Ji, Y. Hu, M. C. Cheng, et al, "Chemical sensitive graphene modulator with a memory effect for internet-of-things applications," *Microsyst. Nanoeng.*, vol. 2, p. 16018, 2016.

[13] H. Y. Huang, M. Sakhdari, M. Hajizadegan, A. Shahini, D. Akinwande, and P. Y. Chen, "Toward transparent and self-activated graphene harmonic transponder sensors," *Appl. Phys. Lett.*, vol. 108, no. 17, p. 173503, 2016.

[14] M. Hajizadegan, M. Sakhdari, L. Zhu, Q. S. Cui, H. Y. Huang, M. C. Cheng, et al, "Graphene sensing modulator: Toward low-noise, self-powered wireless microsensors," *IEEE Sens. J.*, vol. 17, no. 22, pp. 7239-7247, 2017.

[15] S. Kim, B. Cook, J. Copper, A. Traille, A. Georgiadis, H. Aubert, M. M. Tentzeris, "Inkjet-printed substrate integrated waveguide (SIW) passive dual-band retro-directive array on paper substrate for chipless RFID Tag and sensor applications." *In Proceedings of the IEEE MTT-S International Microwave Symposium (IMS)*, Seattle, WA, USA, 2–7 June 2013.

[16] S. Bouaziz, F. Chebila, A. Traille, P. Pons; H. Aubert, M. M. Tentzeris, "Novel microfluidic structures for wireless passive temperature telemetry medical systems using radar interrogation techniques in Ka-band." *IEEE Antennas Wireless Propag. Lett.*, 2012, 11, 1706–1709.

[17] B. S. Cook, R. Vyas, S. Kim, T. Thai, T. Le, A. Traille, H. Aubert, M. M. Tentzeris, "RFID-based sensors for zero-power autonomous wireless sensor networks," *IEEE Sens. J.*, vol. 14, no. 8, pp. 2419-2431, 2014.

[18] X. Gu, S. N. N, L. Guo, S. Hemour, and K. Wu, "Diplexer-based fully passive harmonic transponder for sub-6-GHz 5G-compatible IoT applications," *IEEE Trans. Microw. Theory Tech.*, vol. 67, no. 5, pp. 1675-1687, 2019.

[19] K. Rasilainen, J. Ilvonen, J. M. Hannula, and V. Viikari, “Designing harmonic transponders using lumped-component matching circuits,” *IEEE Antennas Wireless Propag. Lett.*, vol. 16, pp. 246–249, 2017.

[20] V. Palazzi, F. Alimenti, C. Kalialakis, P. Mezzanotte, A. Georgiadis, and L. Roselli, “Highly integrable paper-based harmonic transponder for low-power and long-range IoT applications,” *IEEE Antennas Wireless Propag. Lett.*, vol. 16, pp. 3196–3199, 2017.

[21] X. Gu, L. Guo, S. Hemour, and K. Wu, “Analysis and exploitation of diplexer-based fully passive harmonic transponder for 5G applications,” in *Proc. IEEE MTT-S Int. Microw. Workshop Ser. 5G Hardw. Syst. Technol.*, Dublin, Ireland, Aug. 2018, pp. 1–3.

[22] H. Huang, P. Y. Chen, C. H. Hung, R. Gharpurey, and D. Akinwande, "A zero power harmonic transponder sensor for ubiquitous wireless μL liquid-volume monitoring," *Sci. Rep.*, vol. 6, p. 18795, 2016.

[23] L. Zhu, N. Alkhaldi, H. M. Kadry, S. L. Liao, and P. Y. Chen, "A compact hybrid-fed microstrip antenna for harmonics-based radar and sensor system," *IEEE Antennas Wireless Propag. Lett.*, vol. 17, no. 12, pp. 2444-2448, 2018.

[24] D. Ahbe, S. Beer, T. Zwick, Y. Wang, and M. M. Tentzeris,, "Dual-band antennas for frequency-doubler-based wireless strain sensing," *IEEE Antennas Wireless Propag. Lett.*, vol. 11, pp. 216-219, 2012.

[25] K. R. Carver and J. W. Min, "Microstrip antenna technolog," *IEEE Trans. Antennas Propag.*, vol. 29, no. 1, pp. 2-24, 1981.

[26] W. F. Richards, Y. T. Lo, and D. D. Harriso, "An improved theory of microstrip antennas with applications," *IEEE Trans. Antennas Propag.*, vol. 29, no. 1, pp. 34-46, 1981.

[27] P. Y. Chen and A. Alu, "Dual-mode miniaturized elliptical patch antenna with μ-negative metamaterials," *IEEE Antennas Wireless Propag. Lett.*, vol. 9, pp. 351 - 354, 2010.

[28] P. Y. Chen and A. Alu, "Sub-wavelength elliptical patch antenna loaded with μ-negative metamaterials," *IEEE Trans. Antennas Propag.*, vol. 58, no. 9, pp. 2909-2919, 2010.

[29] J. C. Gutierrez-vega, R. M. Rodriguez-Dagnino, M. A. Meneses-Nava, and S. Chavez-Cerda, "Mathieu functions, a visual approach," *Am. J. Phys.*, vol. 71, no. 3, pp. 233-242, 2003.

[30] D. A. Goldberg, L. J. Laslett and R. A. Rimmer, "Modes of elliptical waveguides: a correction," *IEEE Trans. Microw. Theory Tech.*, vol. 38, no. 11, pp. 1603-1608, 1990.

[31] ANSYS® Academic Research Electromagnetics Suite, Release 19.0.

[32] D. Jackson, "Introduction to Microstrip Antennas," in *IEEE Internetional Symposium on Antennas and Propagation and USNC-URSI National Radio Science Meeting*, Orlando, Florida, USA, 2013.

[33] D. C. Nascimento and J. C. S. Lacava, "Design of low-cost probe-fed microstrip antennas, " in *Microstrip Antennas*, Nasimuddin, Ed. Rijeka, Croatia: InTech, 2011, pp. 1–26

[34] S. S. Zhong and Y. T. Lo, "Single-element rectangular microstrip antenna for dual-frequency operation,," *Electron. Lett.*, vol. 19, pp. 298-300, 1983.

[35] R. B. Waterhouse and N. V. Shuley, "Dual frequency microstrip rectangular patches," *Electron. Lett.*, vol. 28, no. 7, pp. 606-607, 1992.

[36] D. Schaubert, F. G. Farrar, A. Sindoris, and S. T. Hayes, "Microstrip antennas with frequency agility and polarization diversity," *IEEE Trans. Antennas Propag.*, vol. 29, no. 1, pp. 118-123, 1981.

[37] H. K. Kan and R. B. Waterhouse, "Size reduction technique for shorted patches," *Electron. Lett.*, vol. 35, no. 12, pp. 948-949, 1999.

[38] R. B. Waterhouse, S. D. Targonski, and D. M. Kokotoff,, "Design and performance of small printed antennas," *IEEE Trans. Antennas Propag.*, vol. 46, no. 11, pp. 1629-1633, 1998.

[39] X. Zhang and L. Zhu, "Patch antennas with loading of a pair of shorting pins toward flexible impedance matching and low cross polarization," *IEEE Trans. Antennas Propag.*, vol. 64, no. 4, pp. 1226-1233, 2016.

[40] C. Gao, T. Wei, F. Duewer, Y. Lu,and X. D. Xiang, "High spatial resolution quantitative microwave impedance microscopy by a scanning tip microwave near-field microscope," *Appl. Phys. Lett.*, vol. 71, pp. 1872-1874, 1997.

[41] H. Huang, P. S. Zhao, P. Y. Chen, Y. Ren, X. Liu, M. Ferrari, Y. Hu, and D. Akinwande, "RFID tag helix antenna sensors for wireless drug dosage monitoring, " *IEEE J. Transl. Eng. Health Med.*, vol. 2, pp. 1–8, 2014.

[42] K. Saeed, R. D. Pollard, and I. C. Hunter, "Substrate integrated waveguide cavity resonators for complex permittivity characterization of materials," *IEEE Trans. Microw. Theory Tech.*, vol. 56, no. 10, pp. 2340-2347, 2008.

[43] C. Malmberg and A. Maryott, "Dielectric constant of water from 0” to 100°C," *J. Res. Nat. Bureau of Standards*, vol. 56, pp. 1-8, 1956.

[44] G. Akerlöf, "Dielectric constants of some organic solvent-water mixtures at various temperatures," *J. Am. Chem. Soc.*, vol. 54, p. 4125, 1932.

[45] Connectorized Diplexer ZDSS-3G4G-S+ from Mini-Circuit. Available: https://www.minicircuits.com/WebStore/dashboard.html?model=ZDSS-3G4G-S%2B.

[46] MULTIPLIER ZX90-2-36-S+ from Mini-Circuit. Available: https://www.minicircuits.com/WebStore/dashboard.html?model=ZX90-2-36-S%2B.

[47] J. A. Shaw, "Radiometry and the Friis transmission equation," *Am. J. Phys.*, vol. 81, no. 1, pp. 33-37, 2013.

[48] F. Amato and S. Hemour, "The Harmonic Tunneling Tag: a Dual-Band Approach to Backscattering Communications," 2019 *IEEE International Conference on RFID Technology and Applications (RFID-TA)*, Pisa, Italy, 2019, pp. 244-247.

# IV. A COMPACT, PASSIVE FREQUENCY-HOPPING HARMONIC SENSOR BASED ON A MICROFLUIDIC RECONFIGURABLE DUAL-BAND ANTENNA



In this chapter, we describes a battery-free wireless liquid sensor enabled by a harmonic transponder that comprises a dual-band antenna reconfigured by different sample under test (SUT) injected in the fluidic cavity. This microstrip antenna has the hybrid-feed geometry, in which an inner elliptical antenna exhibits wideband resonance at $2f_0$ enabled by hybridization of $TM_{o110}$ and $TM_{e110}$ modes, and an outer split-ring antenna displays a narrow band resonance at the fundamental frequency $f_0$. Particularly, the outer patch is mounted with a fluidic channel for controlling the resonance of the $TM_{310}$ mode at $f_0$. Our results demonstrate the potential of employing this passive wireless sensor in rich-scatting environments filled with crosstalks, clutters and multiple reflections.

## 4.1 Introduction to wireless sensors

Wireless and remote sensing are essential technologies that enable various applications in the scope including wireless healthcare, internet-of-things (IoT), and smart city [1]-[4]. Typically in the wireless sensing platforms, a reader or interrogator will transmit a continuous wave to power a tag and then receives the backscattered RF signals modulated by a actuator or sensor integrated on the tag [5]-[7]. Along with the development of ubiquitous sensors, the ongoing increased wireless nodes and their combinations with heterogeneous networks have generated a rich-scattering environment filled with various electromagnetic interference sources such as clutters, echoes, and crosstalks. To mitigate this issue, a concept named harmonic sensor was explored and has gained numerous attention as it could provide a relatively longer detection range and the enhanced signal-to-noise ratio for electrically small wireless sensors [8]-[12]. This type of

harmonic sensor could be classified as the nonlinear antenna sensor, whose resonant frequency could be sensitively detuned and manipulated by the dielectric properties of the liquid under test [13]-[16]. Different from the traditional radio-frequency identification based sensors, a compact harmonic sensor could receive the monotone signal at fundamental frequency ($f_0$) and next retransmit the modulated higher harmonic signal ($nf_0$) to the bistatic readers. By transmitting and receiving signals at orthogonal frequency, the harmonic wireless sensing scheme has the capability for greatly suppressing echo noises, crosstalks, and clutters, although this nonlinear sensor has a smaller footprint and relatively low radar cross-section (RCS). To date, harmonic sensors have been proved to be efficient in searching RECCO avalanche victim, in tracking small RCS signature insects or frogs [17]-[21], [22], and in real-time continuous recording of biological parameter [23]-[27]. Despite the widespread usages and applications, harmonic sensing still suffer from pitfalls. As an example, they commonly requires dual antennas, namely, a receiver antenna to catch the fundamental tone signal and a transmitter antenna for transmitting the modulated harmonic signal [28], [29], inevitably increasing the overall tag size and fabrication cost. In addition, typical wireless readout that relies on recognizing the amplitude of the backscattered signal may still struggle with the errors and the data misinterpretation generated form the path loss and multipath reflections of the harmonic signals. Even though wide-spectrum absolute sensing can address the aforementioned issue, microstrip antennas utilized in conventional RFID designs are usually exhibiting narrow bandwidth [28], [29], and, therefore, not applicable for wide-spectrum applications.

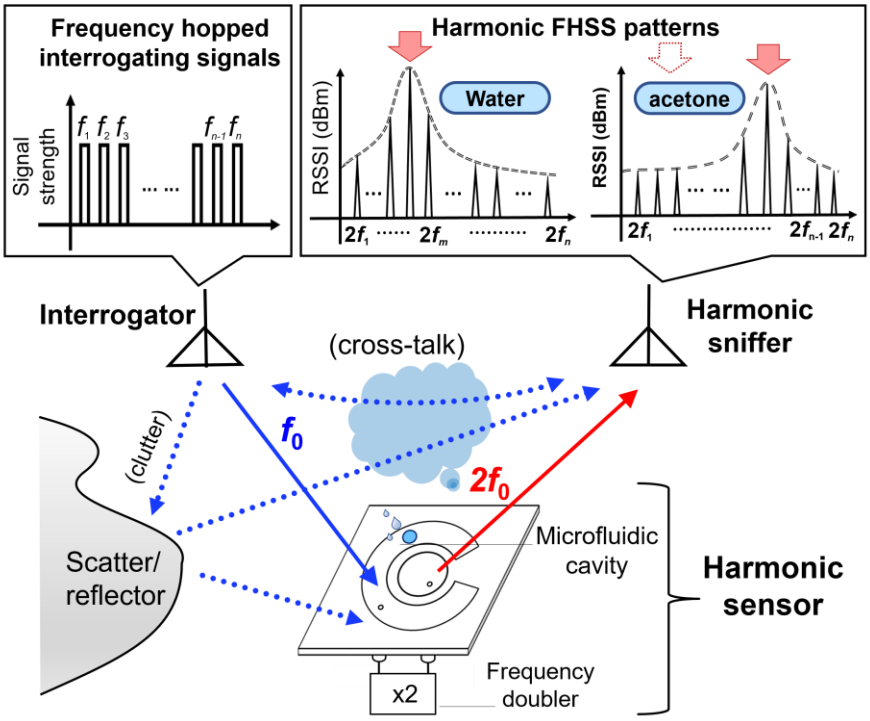


Figure 26. Schematics of a frequency-hopping based harmonic sensor constituted by the proposed dual-band microstrip antenna. This antenna exhibits a liquid-reconfigured narrow-band resonance at its fundamental frequency and another insensitive wideband resonating centered at second-harmonic band.

In this chapter, we study a compact, reconfigurable hybrid dual-band microstrip antenna that could be used for making a fully-passive harmonic sensor to real-time monitor liquid concentration. In principle, this harmonic sensor utilizes a robust wide-spectrum sensing [Fig. 26], which has not yet been explored in the existing RFID systems. The proposed antenna could excite a narrowband resonance at fundamental frequency $f_0$ and a broadband operation at second harmonic $2f_0$, necessary for the frequency-hopping harmonics-based sensing. In addition, as understood from the eigenmodal analysis, the proposed microstrip antenna will be properly loaded with a fluidic channel such that the perturbations caused by the liquid could shift the resonant frequency $f_0$, whereas it is not affecting the broadband resonance at $2f_0$. As a result, a nonlinear, wide-spectrum

absolute sensing configuration could be achieved by analyzing the FHSS pattern of the reader, as shown in Fig. 26.

In this proposed wireless system, the transceiver of the reader could transmit a fixed-strength frequency-hopping sequence with the 20 channels [$f_1$, $f_2$,…, $f_{20}$] to the harmonic tag loaded with the dual-band antenna. These hopping signals will be received continuously by the harmonic sensor, experiencing a frequency doubling process, i.e., [$f_1$, $f_2$,…, $f_{20}$] → [$2f_1$, $2f_2$,…, $2f_{20}$], and then being re-transmitted to the portable sniffers, e.g. smart phone with LTE and 5G antenna including the frequency band of interest. The dielectric constants of the SUT could effectively detune the antenna's resonant frequency, which can be extracted by analyzing the high-dimensional FHSS pattern [$2f_1$, $2f_2$… $2f_{20}$], as described in Fig. 26. This FHSS pattern analysis could provide an accurate and robust absolute resonance sensing scheme, which is not even possible with the one dimensional data received from the traditional non-hopping harmonic RFID sensors.

### 4.2 Theoretical Modeling of Dual-Band Patch Antenna

In this section, I have studied a compact, dual-resonance microstrip patch antenna constituted by an outer split-ring patch cavity and another inner circular patch antenna, respectively resonating at $f_0$ (corresponding to $TM_{310}$ mode of the split-ring cavity) and $2f_0$ (i.e., $TM_{110}$ mode of the circular cavity), with the feeding points suitably located [30]. However, it is known that both resonant modes would have a narrow bandwidth. In order

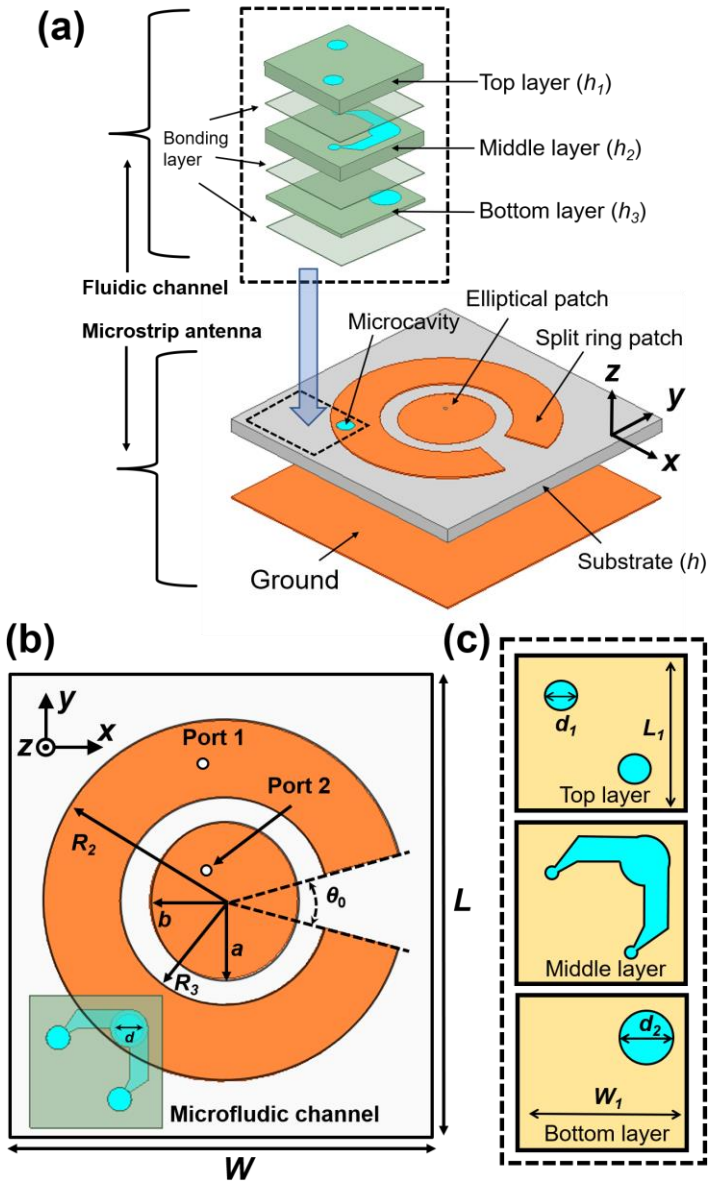


Figure 27. Geometry and the associated dimensions of the proposed dual-resonance microstrip antenna with the integrated fluidic channel: (a) 3-D view and (b) top view of the microstrip patch antenna. (c) Top view of the fluidic channel with three layers.

to perform a FHSS analysis, this inner circular patch is demanded to be replaced by a wideband resonance geometry. In this case, an elliptical patch antenna with simultaneously excited even and odd resonant modes can be the simplest design for enhancing the bandwidth at the second harmonic

band $2f_0$. Besides, unlike our previous studies adopting a rectangular patch loaded with a micro-tank to perturbate the $TM_{010}$ mode [31], we herein mounted the dual-resonance microstrip antenna with a more practical fluidic channel for guiding with different sample-under-tests (SUTs) in and out. Fig. 27 illustrates the geometry of the proposed dual-band microstrip patch antenna comprising an elliptical patch antenna, a concentric split-ring patch antenna, and a fluidic channel fabricated on top. Note that the antenna patch layer is separated from its ground plane by a FR4 substrate with the relative permittivity $\varepsilon_r = 4.2$, loss tangent $\delta = 0.015$, and thickness $h = 1.6$ mm. Given the fact that this antenna has a rather negligible thickness in contrast to its operating wavelength, the resonances could be derived and predicted by cavity model [32]-[34]. In our design, two open cavities are considered, referring to a concentric split-ring cavity and another elliptical one, respectively. The PEC boundaries are assumed to the top and bottom layers of each cavity, and the PMC is applied for their sidewalls. Consequently, the associated transcendental equations for the outer split-ring resonant cavity could be calculated as [30]:

$$J_n'(kR_2)Y_n'(kR_3) - J_n'(kR_3)Y_n'(kR_2) = 0,$$
$$n = \frac{m\pi}{2\pi - \theta_0} \text{ for } m = 1, 2, 3\ldots, \tag{8}$$

where $J_n(\cdot)$ and $Y_n(\cdot)$ are the Bessel functions of the first and the second kinds, $k = \omega\sqrt{\varepsilon_r\varepsilon_0\mu_0}$, $\varepsilon_0$ and $\mu_0$ are the free-space permittivity and permeability. According to Eq. (8), I have designed a split-ring patch with $TM_{310}$ mode of $m = 3$, $R_2 = 38.2$ mm, $R_3 = 22$ mm, and also $\theta_0 = 30°$, providing a narrow resonance at the fundamental frequency of 1.31 GHz. As for the elliptical cavity with the elliptical coordinate ($\xi$, $\eta$), where $\xi \in [0, \infty]$ and $\eta \in [0, 2\pi]$, its transcendental

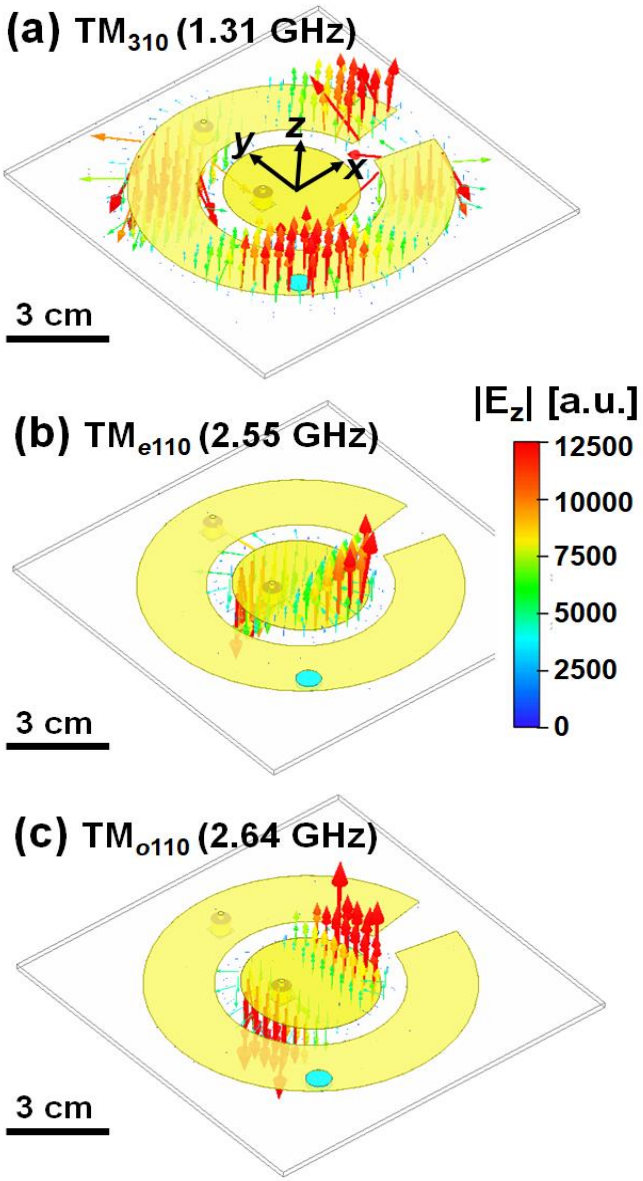


Figure 28. Simulation results for snapshots of electric field Ez: (a) TM310 mode at 1.31 GHz, (b) TMe110 mode at 2.55 GHz, and (c) TMo110 mode at 2.64 GHz.

equations could be reduced to the following set, after applying PMC boundary conditions at the sidewall $\xi = \xi_0$ [35], [36]:

$$\begin{aligned} M'^{(1)}_{e,n}(\xi_0, q) &= 0 \quad \text{for } n\text{-th even mode} \\ M'^{(1)}_{o,n}(\xi_0, q) &= 0 \quad \text{for } n\text{-th odd mode} \end{aligned} \tag{9}$$

where $q = c^2k^2/4$, the semi-focal length $c = \sqrt{a^2 - b^2}$, $M^{(1)}_{e,n}(\xi, q)$ and $M^{(1)}_{o,n}(\xi, q)$ are the even and odd radial Mathieu function of the first kind, respectively, *n* is the order of the angular Mathieu functions $C_{e,n}(\eta, q)$ and $S_{e,n}(\eta, q)$, which can determine the azimuthal variation along $\eta$ [37], [38]. By solving the aforementioned transcendental equations with $\xi_0$ = 1.83 (i.e., *a* = 16.5 mm, and *b* = 15.675 mm), we find that the first even-order mode, namely, $TM_{e110}$ at 2.55 GHz and the first odd-order mode referring to $TM_{o110}$ at 2.64 GHz could be simultaneously excited in the second-harmonic band, thereby achieving a relatively wideband resonance. We also conducted full-wave numerical simulations [39] based on commercial HFSS software to validate the analytical assumptions. Figs. 28(a)-(c) report the snapshots of the electric field distributions for different modes of interest, i.e., $TM_{310}$, $TM_{e110}$ and $TM_{o110}$ modes, respectively. The simulated electric field distributions match quite well with the results achieved from the cavity model, proving that the excited $TM_{e110}$ and $TM_{o110}$ modes could exhibit a orthogonal modal pattern.

### 4.3 Experimental results

Based on the theoretical analysis, I have fabricated a dual-band microstrip patch antenna with the FR4 substrate and copper strips, as described in Fig. 29. Some important parameters are concluded

in Table II. Here, we should noted that, in order to simultaneously excite the $TM_{e110}$ mode at 2.55 GHz and $TM_{o110}$ mode at 2.64 GHz for the elliptical patch, we placed a 50 ohms coaxial cable at the coordinate $x$ = -5 mm, $y$ = 4.5 mm. In addition, a fluidic cavity with the radius $r$ = 2 mm is drilled at the position of $x$ = -27 mm and $y$ = -20 mm, near which the $TM_{310}$ resonance displays a maximum electric field distribution [see Fig. 28(a)]. To precisely control the volume in the drilled cavity, a fluidic channel

Table II: Parameters of the fabricated patch antenna in Fig. 29 (Unit: mm)

| | | | | |
|---|---|---|---|---|
| $L$ = 85 | $L_1$ = 22 | $W$ = 85 | $W_1$ =22 | $h_1$ = 1.5 |
| $h_2$ = 1.5 | $h_3$ = 0.1 | $a$ = 16.5 | $b$ =15.675 | $\theta_0$ = 30 |
| $R_2$ = 38.2 | $R_3$ = 22 | $d$ = 4 | $d_1$ = 3.2 | $d_2$ = 5 |

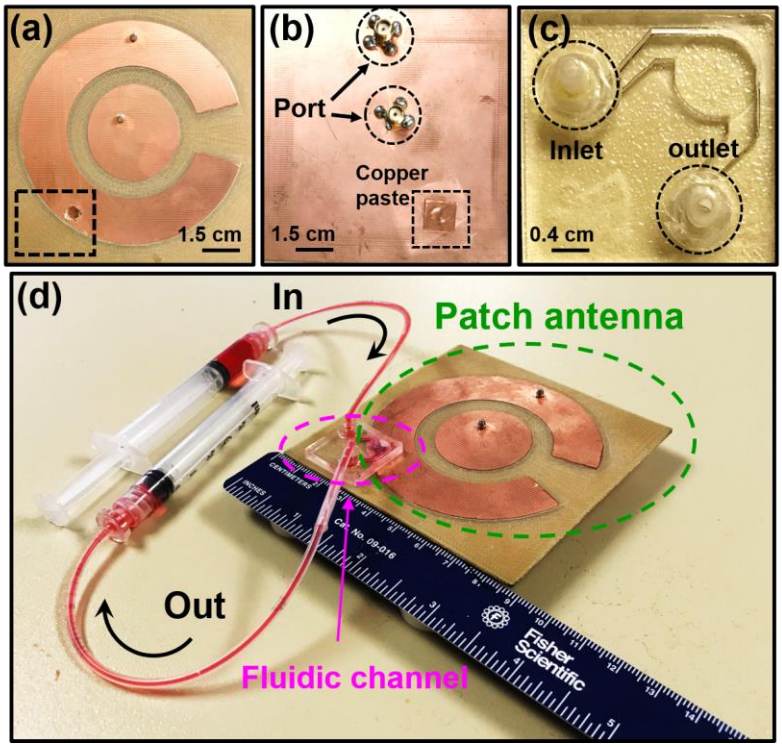

Figure 29. Photograph of the dual-resonance patch antenna with (a) top view, (b) bottom view and (c) top view of the fluidic channel. (d) Photograph of the integrated harmonic sensor with a fluidic channel guiding sample under test in and out.

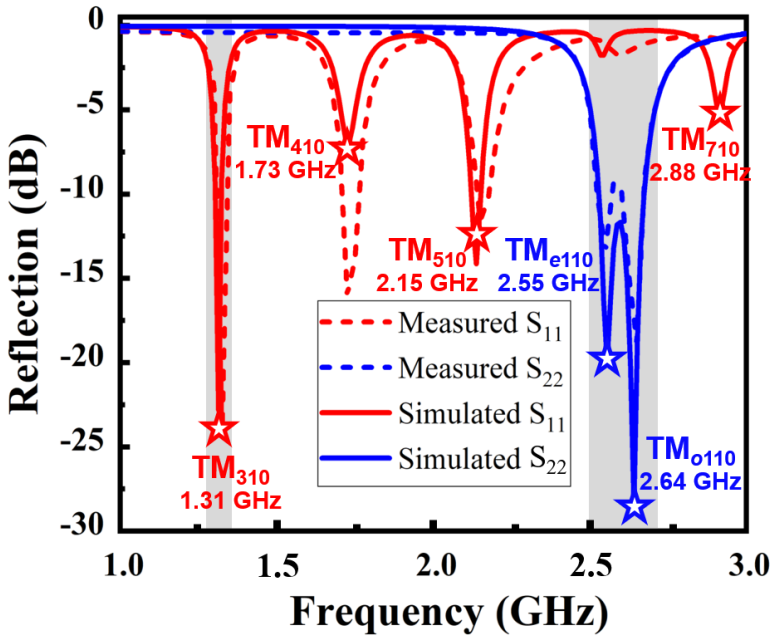


Figure 30. Measured and simulated reflection coefficient for the proposed microstrip antenna in Fig. 29. Here, the analytical results obtained from Eqs. (8) and (9) are also highlighted by stars.

formed by three acrylic layers with the thickness $h_1$, $h_2$ and $h_3$ was fabricated, with each laser thickness detailed in Table II. Here, different layers were etched into the specific shapes [Fig. 27] by utilizing Epilog Mini 24 laser-cutter, followed by mechanical bonding with the double-sided adhesive tape. Next, the assembled fluidic channel was loaded onto the patch antenna and connected to two plastic tubes to serve as the inlet and outlet for the sample under test [Fig. 29]. Fig. 30 presents the simulated and measured reflection coefficients for this dual-band microstrip

patch antenna, in which the resonant modes derived by Eqs. (8) and (9) are also highlighted, which agree quite well with our full-wave numerical simulation results. Our measurement results validate the dual-band resonating behavior of the microstrip antenna, with one reflection dip at 1.33 GHz for fundamental tone and another broadband resonance at its corresponding harmonic frequency (i.e., 2.5 GHz - 2.7 GHz). Even though this harmonic sensor is refined to work in the S-band ranging from 2 GHz to 4 GHz, this concept and design strategy could be easily transferred to any frequency bands. Fig. 31 presents

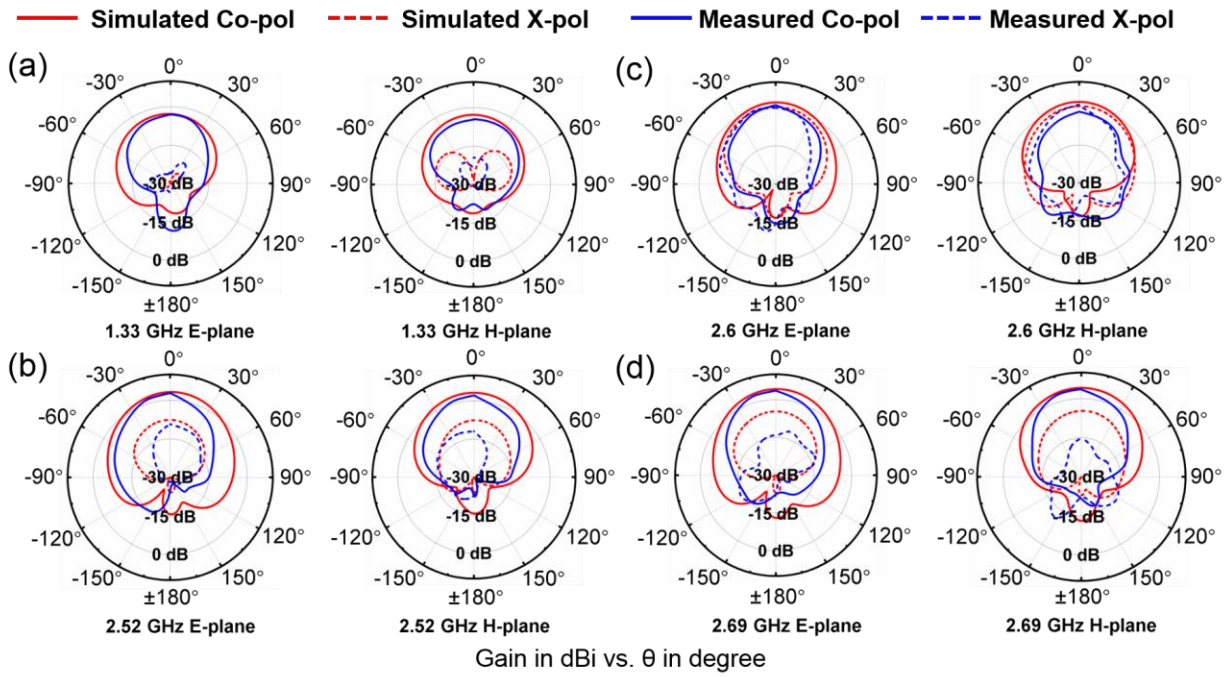


Figure 31. Radiation patterns for the microstrip antenna on the E- and H-planes at: (a) 1.33 GHz, (b) 2.52 GHz, (c) 2.6 GHz, and (d) 2.69 GHz.

the simulated and measured radiation patterns of the dual-resonance microstrip antenna on the E- and H-planes at its frequency band of interest. We note that for the $TM_{310}$ mode, the E-plane is the *yz*-plane and the H-plane is referring to *xz*-plane in the 3D space, different from those for the $TM_{e110}$

($TM_{o110}$) modes with *yz*- and *xz*-planes (*xz*- and *yz*-planes). The measured co-polarization patterns exhibiting broadside radiation are in excellent agreement with the simulation ones. Specifically at 1.33 GHz under $TM_{310}$ mode, this antenna displays a maximum measured gain of -1.5 dBi, with a HPBW of 72° and 106° on the E-plane and H-plane, respectively. For the second-harmonic band, the $TM_{e110}$ mode at 2.52 GHz and $TM_{o110}$ mode at 2.69 GHz display the orthogonal linear polarizations, while a circular polarization can be obtained between the two modes at 2.6 GHz. At 2.52 GHz, the antenna exhibits a maximum realized gain of 4.5 dBi and a HPBW of 84° (120°) on the E-plane (H-plane). At 2.69 GHz, the achieved gain is 5.7 dBi and a HPBW of 77° (115°) on the E-plane (H-plane). In these two scenarios, an extremely high co-polarization discrimination is obviously seen, with the cross-polarization <-15 dB and -10 dB on the E-plane and H-plane, respectively. As for 2.6 GHz, the proposed antenna displays a maximum antenna gain of 5.3 dBi and a HPBW of 86° (116°) on the E-plane (H-plane). In this manner, the cross-polarization radiation pattern is quite similar to its co-polarization pattern, demonstrating the intrinsic circular polarization properties of the proposed elliptical patch antenna. Here, it should be noted that due to the relatively high dielectric losses in the FR4 substrate, the measured radiation efficiency is around 27 % at 1.31 GHz and greater than 80 % for the wideband antenna. The efficiency of the proposed microstrip antennas could be further improved by using a high-quality substrate with smaller power dissipation.

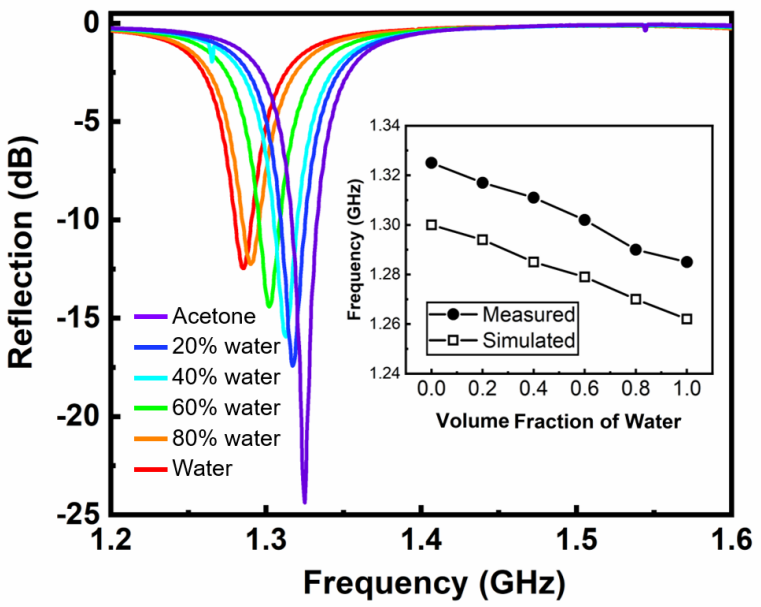


Figure 32. Measured reflection spectrum with regard to TM310 mode for the microstrip patch antenna, injected with different concentrations of acetone-water mixture. Here, the inset concludes the measured and calculated resonance frequencies in response to different volume fraction of water.

Next, we develop a sensing functionality of this proposed reconfigurable dual-band antenna with regard to its reflection spectrum. To the end of this chapter, acetone and water mixtures with different concentrations were adopted with their permittivities shown in Table III [40]-[42]. Based on proven perturbation theory [43], [44], the dielectric properties of the SUT injected into the fluidic channel could be characterized by the up- or down-shift of the resonance frequencies at $f_0$. In this measurement, to track the variation of the resonant frequency of the dual-band antenna, we used a the Agilent N5222A PNA network analyzer to record and monitor the reflection spectrum, i.e., $S_{11}$ and also $S_{22}$, of the antenna, and the results for acetone-water mixtures are depicted in Fig. 32. We find that with the increase of the volume ratio of water in the mixtures, that is to say, increasing the dielectric constants of the SUT, the resonance frequency of the $TM_{310}$ mode will downshift from 1.325 to 1.287 GHz, whereas the second-harmonic frequency with the

coupled $TM_{e110}$ and $TM_{o110}$ modes could remain the same. The inset of Fig. 32 concludes the resonance frequency variations in response to different volume fractions of water in the mixture, from which it can be clearly seen that the simulations and measurements are in accordance with each other, both showing excellent linearity and sensitivity in the applications of determination of volume fraction in binary liquid mixtures.

Table III: Permittivities of acetone-water mixtures with different concentration.

| Mixtures | 0 % (acetone) | 20% | 40% | 60% | 80% | 100 % (water) |
|---|---|---|---|---|---|---|
| $\varepsilon'_r$ | 20.7 | 25 | 35 | 45 | 66 | 80 |
| $\varepsilon''_r$ | 0.5 | 1 | 1.65 | 2.5 | 4.3 | 6 |

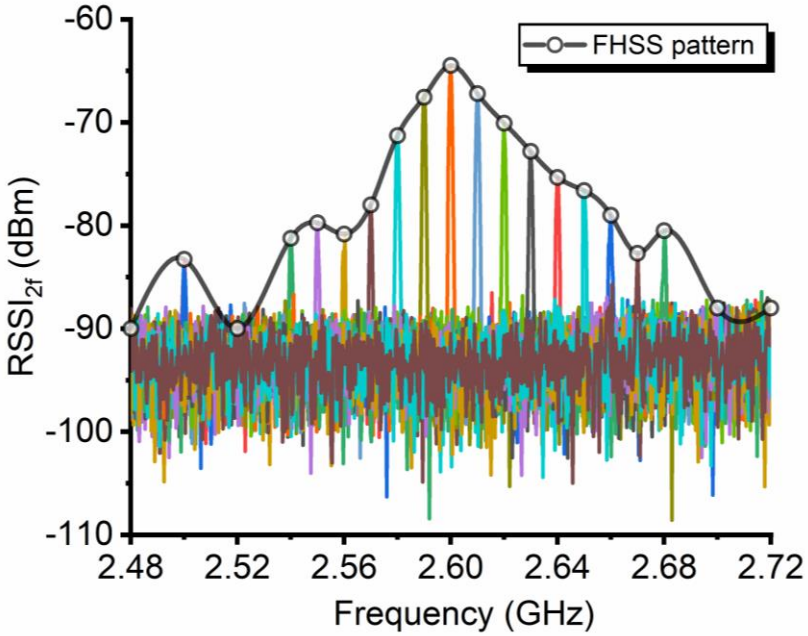


Figure 33. Measured harmonic RSSI array under the water-acetone mixture (60 %). The envelope of this RSSI could form the FHSS pattern, which contains important sensing information for recognizing the SUT.

By assembling the fabricated reconfigurable microstrip antenna with a passive frequency multiplier [45], a fully-passive wireless sensing scheme could be built, referring as a compact harmonic sensor. In this measurement, a bistatic radar measurement configuration was adopted for the wireless telemetry. In brief, our transceiver will continuously transmit a frequency-hopped signal divided into 20 channels to the under test harmonic sensor, which then modulates the signal and finally resends the second harmonic tones back to a sniffer devices. Note that the envelope of these backscattered harmonic tones could form a FHSS pattern, whose peak position versus frequency is controlled by the effective permittivity of the injected SUT, as described in Fig. 33. This wireless and far-field sensing mechanism could be comprehensively explained in the following. According to the widely known Friis equation [46], the ratio of the received power to the launched one is determined by:

$$\frac{P_r}{P_t} = \left(\frac{\lambda_0}{4\pi R_1}\right)^2 \cdot \left(\frac{\lambda_0/2}{4\pi R_2}\right)^2 \cdot \frac{G_1 G_2 G_T G_R}{L_{sys}} \cdot \left|\hat{\rho}_1 \cdot \hat{\rho}_t\right|^2 \cdot \left|\hat{\rho}_2 \cdot \hat{\rho}_r\right|^2, \qquad (10)$$

where $G_1$ ($G_2$) respectively represent the realized gain of the dual-band antenna at $f_0$ ($2f_0$), $G_T$ ($G_R$) denotes the realized gain of the transceiver (sniffer) utilized to interrogate the passive sensor, $R_1$ ($R_2$) is the distances between $T_x$ ($R_x$) and the harmonic sensor, $L_{sys}$ is the overall system loss containing the frequency-conversion loss of the frequency conversion device and parasitics caused by cable or connectors. Here, some important parameters are: $P_t$ = 25 dBm, $R_1 = R_2$ = 1.0 m, $G_T$ = 5.5 dBi at 1.1 GHz and $G_R$ = 12 dBi at 2.6 GHz. In Eq. (10), $\left|\hat{\rho}_1 \cdot \hat{\rho}_t\right|^2$ is referring to the polarization coupling factor between the transmitter antenna and the proposed harmonic sensor,

approximately equal to unity if the two antennas are aligned well to each other. On the other hand, $\left|\hat{\rho}_2 \cdot \hat{\rho}_r\right|^2$ is accounting for the polarization mismatch between the receiver antenna and the antenna sensor. As the $TM_{e110}$ and $TM_{o110}$ modes have been proved with orthogonal polarizations, the $R_x$ antenna is necessary to be titled by 45° to capture the radiation generated by both modes, and thus, $\left|\hat{\rho}_2 \cdot \hat{\rho}_r\right|^2$ is equal to ~ 50 % in the entire harmonic band of interest. In conclusion, based on Eq. (10), the RSSI will be proportional to the realized gain $G_1$ and $G_2$ of the dual-band antenna, where $G_2$ remains almost constant with only ±0.5 dB fluctuation, while $G_1$ is demonstrated quite sensitive to the concentration of different acetone-water mixtures. As a results, when the acetone concentration decreases, which means the increase of the dielectric constant of the mixture, the frequency of the peak $G_1$ will be shifted from 1.325 to 1.287 GHz, resulting in the FHSS pattern downshifting as depicted in Fig. 34(c) (in an anechoic chamber) and Fig. 34(d) (in a rich-scattering indoor environment). It is obviously seen that the peak RSSI of the FHSS pattern is sensitively detuned from 2.642 to 2.58 GHz and such a trend is rather independent of the density of the electromagnetic environment, i.e., various electromagnetic interferences. In this chapter, for comparison, we also utilized the conventional passive backscatter sensor for wirelessly monitoring the same SUT. In this experiment, the microstrip antenna is disconnected from the

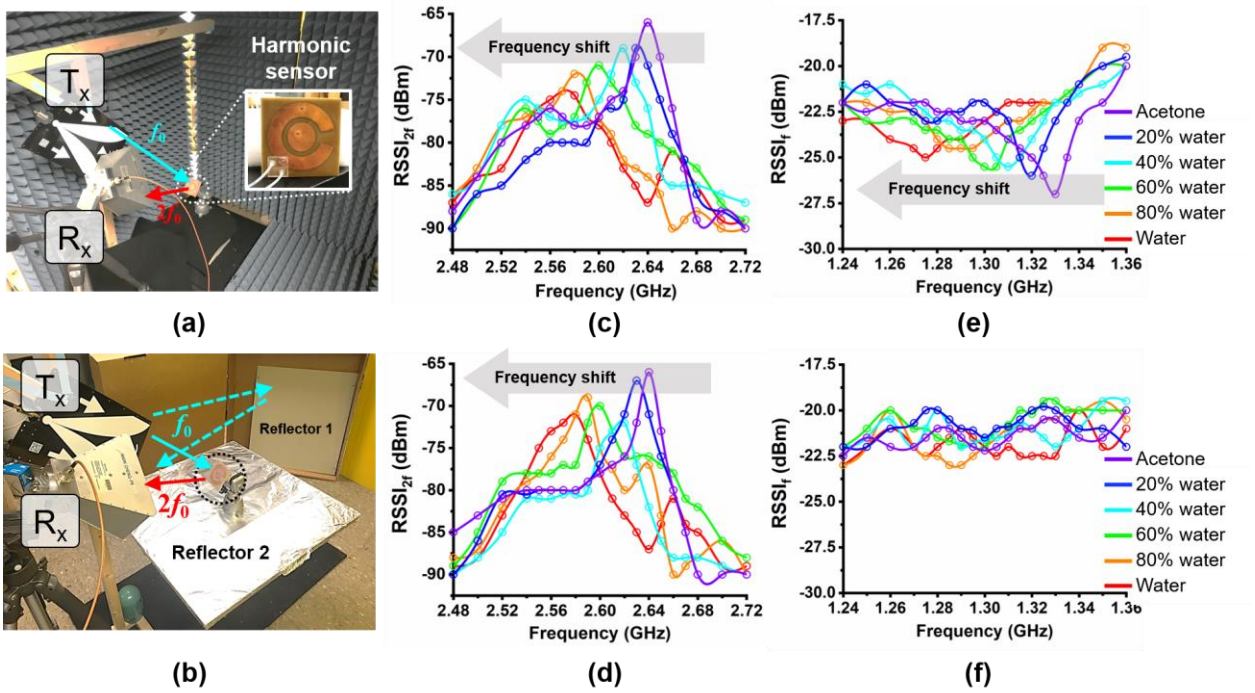


Figure 34. Experimental configuration for characterizing the wireless harmonic sensors in (a) anechoic chamber and (b) rich-scattering indoor environment. Measured FHSS pattern for the harmonic sensor in (c) anechoic chamber and (d) rich-scattering indoor environments. (e), (f) are similar to (c), (d), but for the backscatter antenna sensor.

frequency multiplier and its port 1 is connected to a 50 Ω match load. We note that in this passive scattering scheme, the extinction cross section will be the sum of the absorption and scattering cross sections. A significant dip in RSSI and RCS spectrum may be observed at the resonance. In this case, the incident power may be absorbed without causing significant scattering, in other words, the absorption cross section is greater than the scattering cross section [47]. Figs. 34(e) and 34(f) present the measured FHSS pattern for the backscatter antenna sensor in the anechoic chamber and also rich-scattering environment, respectively. Notice that even though the backscatter sensor could function well in the

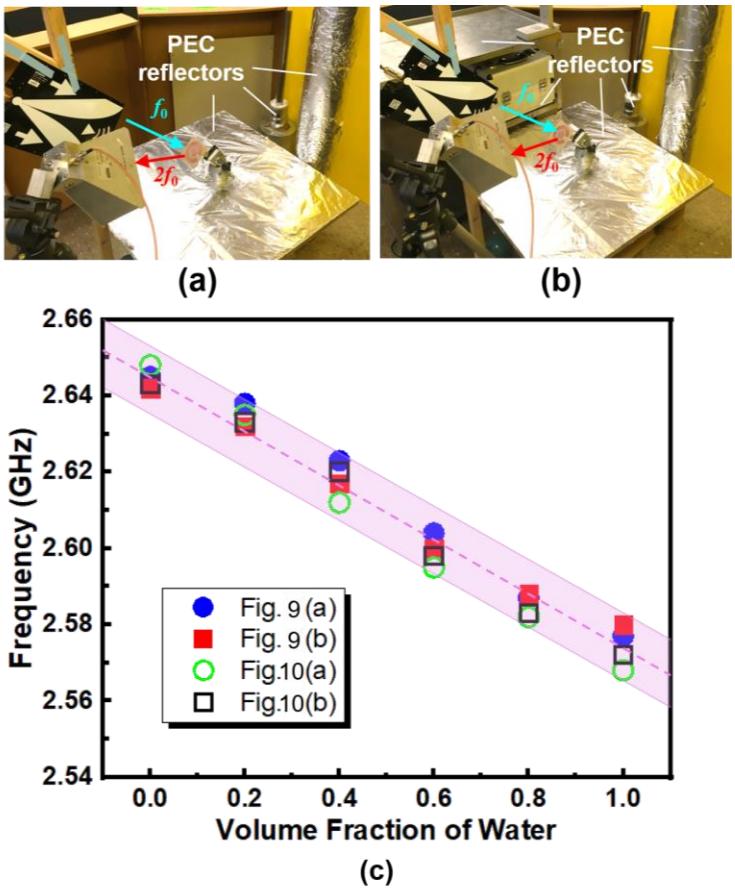


Figure 35. Experimental configurations in rich-scattering environments with (a) two more metal reflectors and (b) six metal reflectors. (c) Peak RSSI frequency in response to different volume fraction of water in the mixtures.

noise-free anechoic chamber, it fails to detect the properties of SUT in a rich-scattering environment associated with various clutters, echoes and multipath scattering. By constrast, our proposed frequency-hopping harmonic sensor could sensitively and robustly detect dielectric properties of SUT, regardless of these environmental interferences. Fig. 35 concludes the measured values of FHSS pattern in response to the water volume fraction in different environments. It is evidently seen that increasing the number of PEC reflectors around the harmonic sensor would not affect its sensing performance, further demonstrating the effectiveness and robustness of our

frequency-hopping harmonic sensor. Furthermore, we could also define the sensitivity of our harmonic sensor as the slope of the curve, i.e., -0.62 MHz/1%, denoting that if the volume fraction of water is increased by 1%, the peak of the FHSS pattern will be downshifted by 0.62 MHz. Such resolvability and sensitivity could even allow us to differentiate two SUT with a difference of 5%.

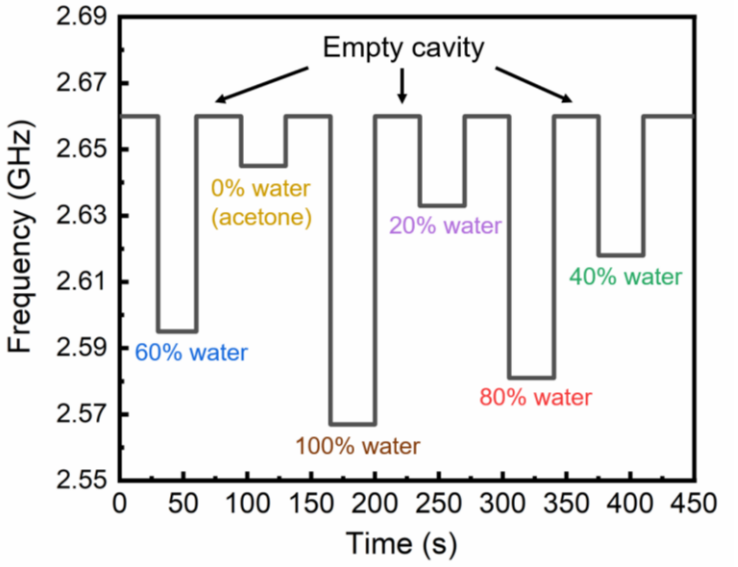


Figure 36. Transient response for the passive harmonic sensor operating in a rich-scattering environment; here, different mixtures were injected in and emptied from the fluidic channel every minute, with a 30 s interval.

Finally, we validated the repeatability and also the transient response of this harmonic sensor operating in the noisy environment. In this measurement, different acetone-water mixtures were injected in and emptied from the fluidic channel every minute, with a 30 s interval referring to empty state. Our results shown in Fig. 36 clarify that this harmonic sensor could always restore to its initial state, namely, with a peak RSSI at 2.66 GHz after several operating cycles. This

repeatable and stable wireless sensing ability could enable various healthcare and biological monitoring applications, for example, the wireless lab-on-chip platform. It should be also noted that the proposed compact harmonic sensor could even be integrated with more sophisticated fluidic channels or diagnostic assays for maximizing its potential for high-performance wireless sensing and telemetering.

### 4.4 Conclusion

I have also developed a reconfigurable dual-band antenna for realizing far-field wireless frequency-hopping sensing. The proposed antenna, loaded properly with a fluidic channel, is able to exhibit a reconfigurable narrow resonance of the fundamental frequency and an unvaried wideband resonance of the second-harmonic band. I have demonstrated that this dual band antenna is useful for frequency-hopping telemetry scheme, allowing for robust wireless mixture sensing in rich-scattering environments. The implementation of this compact zero-power harmonic sensors with a capability of noise suppression will pave the way for future integrated internet-of-things sensors and battery-less smart nonlinear tags.

## REFERENCES


[1] X. L. Jia, Q. Y. Feng, T. H. Fan, and Q. S. Lei, "RFID technology and its applications in Internet of Things (IoT)," in *2012 2nd Int. Conf. Consum. Electron, Commun. Netw,*, China, 2012.

[2] E. Welbourne, et al., "Building the Internet of Things using RFID: the RFID ecosystem experience." *IEEE Internet Computing*, vol. 13.3, pp. 48-55, 2009.

[3] G. Bedi, G. K. Venayagamoorthy, R. Singh, R. R. Brooks, K. K. Wang, "Review of Internet of Things (IoT) in electric power and energy systems," *IEEE Internet Things J.*, vol. 5, no. 2, pp. 847-870, 2018.

[4] S. Amendola, R. Lodato, S. Manzari, C. Occhiuzzi, and G. Marrocco, "RFID technology for IoT-based personal healthcare in smart spaces," *IEEE Internet Things J.*, vol. 1, no. 2, pp. 144-152, 2014.

[5] S. Preradovic, I. Balbin, N. C. Karmakar, and G. F. Swiegers, "Multiresonator-based chipless RFID system for low-cost item tracking," *IEEE Trans. Microw. Theory Tech.*, vol. 57, no. 5, pp. 1411- 1419, 2009.

[6] K. G. Ong, K. F. Zeng, and C. A. Grimes, "A wireless, passive carbon nanotube-based," *IEEE Sens. J.*, vol. 2, no. 2, pp. 82-88, 2002.

[7] R. Bhattacharyya, C. Floerkemeier, and S. Sarma, "Low-cost, ubiquitous RFID-tag-antenna-based sensing," *Proc. IEEE*, vol. 98, no. 9, pp. 1593 -1600, Sep. 2010.

[8] F. Alimenti, and L. Roselli, "Theory on zero-power RFID sensors based on harmonic generation and orthogonally polarized antennas, " *Progress In Electromagnetics Research*, Vol. 134, 337-357, 2013.

[9] K. Rasilainen, J. Ilvonen, A. Lehtovuori, J. M. Hannula, and V. Viikari, "Harmonic transponders: Performance and challenges," *Progress In Electromagnetics Research*, Vol. 134, 337-357, 2013.

[10] K. Rasilainen, J. Ilvonen, and V. Viikari, "Antenna matching at harmonic frequencies to complex load impedance," *IEEE Antennas Wireless Propag. Lett.*, vol. 14, pp. 535-538, 2014.

[11] K. Rasilainen, J. Ilvonen, A. Lehtovuori, J. M. Hannula, V. Viikari, "On design and evaluation of harmonic transponders" *IEEE Trans. Antennas Propag*., vol. 63 no. 1 pp. 15-23 Jan. 2015

[12] X. Q. Guo, S. N. N, L. Guo, S. Hemour, and K. Wu, "Diplexer-based fully passive harmonic transponder for sub-6-GHz 5G-compatible IoT Applications," *IEEE Trans. Microw. Theory Tech.,* to be published, pp. 1-3, 2019.

[13] Y. Feng, Y. Li, L. Li, B. Ma, H. Hao, and L. Li, "Tissue-dependent comatching method for dual-mode antenna in implantable neurostimulators," *IEEE Trans. Antennas Propag.*, vol. 67, no. 8, pp. 5253–5264, Aug. 2019.

[14] Y. Li, Z. Zhang, W. Chen, Z. Feng, and M. F. Iskander, "A switchable matching circuit for compact wideband antenna designs," *IEEE Trans. Antennas Propag.*, vol. 58, pp. 3450–3457, Nov.2010

[15] Y. Li, Z. Zhang, W. Chen, Z. Feng, and M. F. Iskander, "A compact DVB-H antenna with varactor-tuned matching circuit," *Microw. Opt. Technol. Lett.*, vol. 52, no. 8, pp. 1786–1789, 2010.

[16] Y. Feng, Y. Li, L. Li, B. Ma, H. Hao, and L. Li, "Design and system verification of reconfigurable matching circuits for implantable antennas in tissues with broad permittivity range," *IEEE Trans. Antennas Propag.*, Nov.2019

[17] B. G. Colpitts, G. Boiteau, "Harmonic radar transceiver design: miniature tags for insect tracking," *IEEE Trans. Antennas Propag.*, vol. 52, no. 11, pp. 2825-2832, 2004.

[18] D. Mascanzoni and H. Wallin, "The harmonic radar: A new method of tracing insects in the fields," *Ecol. Entomol.*, vol. 11, pp. 387-390, 1986.

[19] J. R. Riley, A. D. Smith, D. R. Reynolds, and A. S. Edwards, "Tracking bees with harmonic radar," *Nature*, vol. 379, pp. 29-30, 1996.

[20] D. Psychoudakis, W. Moulder, C.-C. Chen, H. Zhu, and J. L. Volakis, "A portable low-power harmonic radar system and conformal tag for insect tracking, " *IEEE Antennas Wireless Propag. Lett.*, vol. 7, pp. 444-447, 2008.

[21] J. L. Osborne et al., "A landscape-scale study of bumble bee foraging range and constancy using harmonic radar," *J. Appl. Ecol.*, vol. 36, pp. 519-533, Sep. 1999.

[22] C. Van Tilburg et al., "Wilderness Medical Society practice guidelines for prevention and management of avalanche and nonavalanche snow burial accidents," *Wilderness Environ. Med.*, vol. 28, no. 1, pp. 23-42, Mar. 2017.

[23] M. Hajizadegan, M. Sakhdari, L. Zhu, Q. Cui, H. Huang, M. C. Cheng, and P. Y. Chen, "Graphene sensing modulator: Toward low-noise, self-powered wireless microsensors," *IEEE Sens. J.*, vol. 17, no. 22, pp. 7239-7247, 2017.

[24] H. Huang, P. Y. Chen, C. H. Hung, R. Gharpurey, and D. Akinwande, "A zero power harmonic transponder sensor for ubiquitous wireless μL liquid-volume monitoring," *Sci. Rep.*, vol. 6, p. 18795, 2016.

[25] H. Huang, M. Sakhdari, M. Hajizadegan, A. Shahini, D. Akinwande, and P. Y. Chen, "Toward transparent and self-activated graphene harmonic transponder sensors," *Appl. Phys. Lett.*, vol. 108, no. 17, p. 173503, 2016.

[26] A. Lazaro, R. Villarino, and D. Girbau, "A Passive Harmonic Tag for Humidity Sensing," *International Journal of Antennas and Propagation*, vol. 2014, Article ID 670345, 11 pages, 2014.

[27] H. Huang, L. Tao, F. Liu, et al, "Chemical sensitive graphene modulator with a memory effect for internet-of-things applications," *Microsyst. Nanoeng.*, vol. 2, p. 16018, 2016.

[28] D. Ahbe, S. Beer, T. Zwick, Y. Wang, and M. M. Tentzeris, "Dual-band antennas for frequency-doubler-based wireless strain sensing," *IEEE Antennas Wireless Propag. Lett.*, vol. 11, pp. 216-219, 2012.

[29] C. Cho, X. H. Yi, D. Li, Y. Wang, and M. M. Tentzeris, "Passive wireless Frequency doubling antenna sensor for strain and crack sensing," *IEEE Sens. J*, vol. 16, no. 14, pp. 5725-5733, 2016.

[30] L. Zhu, N. Alkhaldi, H. M. Kadry, S. L. Liao, and P. Y. Chen, "A compact hybrid-fed microstrip antenna for harmonics-based radar and sensor system," *IEEE Antennas Wireless Propag. Lett.*, vol. 17, no. 12, pp. 2444-2448, 2018.

[31] L. Zhu, and P. Y. Chen, "A compact, zero-power and low-noise harmonic-transponder for liquid and moisture sensing," in 2019 *IEEE International Symposium on Antennas and Propagation and USNC-URSI Radio Science Meeting*, Atlanta, GA, USA, USA, 2019.

[32] K. R. Carver and J. W. Min, "Microstrip antenna technolog," *IEEE Trans. Antennas Propag.*, vol. 29, no. 1, pp. 2-24, 1981.

[33] W. F. Richards, Y. T. Lo, and D. D. Harriso, "An improved theory of microstrip antennas with applications," *IEEE Trans. Antennas Propag.*, vol. 29, no. 1, pp. 34-46, 1981.

[34] D. M. Pozar, Microwave Engineering, 4th Edition, John Wiley & Sons, 2012.

[35] J. C. Gutierrez-vega, R. M. Rodriguez-Dagnino, M. A. Meneses-Nava, and S. Chavez-Cerda, "Mathieu functions, a visual approach," *Am. J. Phys.*, vol. 71, no. 3, pp. 233-242, 2003.

[36] D. A. Goldberg, L. J. Laslett and R. A. Rimmer, "Modes of elliptical waveguides: a correction," *IEEE Trans. Microw. Theory Tech.*, vol. 38, no. 11, pp. 1603-1608, 1990.

[37] P. Y. Chen and A. Alu, "Dual-mode miniaturized elliptical patch antenna with μ-negative metamaterials," *IEEE Antennas Wireless Propag. Lett.*, vol. 9, pp. 351 - 354, 2010.

[38] P. Y. Chen and A. Alu, "Sub-wavelength elliptical patch antenna loaded with μ-negative metamaterials," *IEEE Trans. Antennas Propag.*, vol. 58, no. 9, pp. 2909-2919, 2010.

[39] ANSYS® Academic Research Electromagnetics Suite, Release 19.0.

[40] C. Malmberg and A. Maryott, "Dielectric constant of water from 0” to 100°C," *J. Res. Nat. Bureau of Standards,* vol. 56, pp. 1-8, 1956.

[41] G. Akerlöf, "Dielectric constants of some organic solvent-water mixtures at various temperatures," *J. Am. Chem. Soc.*, vol. 54, p. 4125, 1932.

[42] C. Gao, T. Wei, F. Duewer, Y. Lu,and X. D. Xiang, "High spatial resolution quantitative microwave impedance microscopy by a scanning tip microwave near-field microscope," *Appl. Phys. Lett.*, vol. 71, pp. 1872-1874, 1997.

[43] K. Saeed, R. D. Pollard, and I. C. Hunter, "Substrate integrated waveguide cavity resonators for complex permittivity characterization of materials," *IEEE Trans. Microw. Theory Tech.,* vol. 56, no. 10, pp. 2340-2347, 2008.

[44] H. Huang, P. S. Zhao, P. Y. Chen, Y. Ren, X. Liu, M. Ferrari, Y. Hu, and D. Akinwande, "RFID tag helix antenna sensors for wireless drug dosage monitoring, " *IEEE J. Transl. Eng. Health Med.*, vol. 2, pp. 1–8, 2014.

[45] FK-3000+ from Mini-Circuit. Availabe: www.minicircuits.com /WebStore/dashboard_html?model=FK-3000%2B.

[46] J. A. Shaw, "Radiometry and the Friis transmission equation," *Am. J. Phys.*, vol. 81, no. 1, pp. 33-37, 2013.

[47] A. M. J. Marindra and G. Y. Tian, “Chipless RFID sensor tag for metal crack detection and characterization,” *IEEE Trans. Microw. Theory Techn.*, vol. 66, no. 5, pp. 2452–2462, May 2018.

# V. ABSOLUTE VALUE WIRELESS SENSING BASED ON NONLINEAR HARMONIC ANALYSIS ASSISTED WITH FREQUENCY-HOPPING SPREAD SPECTRUM



In this chapter, I introduce a wireless sensing platform, which can enable long-range interrogating of compact and passive sensors in complex environments. This telemetry approach requires postprocessing the higher order received signal strength indicator in the frequency hopping spread spectrum (i.e., FHSS), in which the harmonic sensor has a narrow resonance antenna sensor working at fundamental frequency $f_0$ and a wideband circular monopole antenna covering the second harmonic spectrum at $2f_0$. I have proved that the information of the liquid-reconfigured antenna sensor can be encoded in the peak value of the harmonic received signal strength indicator (RSSI) pattern. Therefore, I envision that this lightweight and battery-free harmonic sensing system could be beneficial for widespread usages in healthcare and internet-of-things (IoTs) applications, such as serving as rapid contactless point-of-care (POC) tests and telemedicine.

## 5.1 Introduction

In recent years, passive RFID systems have experienced tremendous growth and been deployed in various applications. As a representative example, in Industry 4.0, retailers and manufacturers have employed the RFID technology to perform medium-range tracking and also identification of objects [1, 2]. Take one step further, battery-less, low-cost and low-profile RFID tags integrated with sensing modulus could further enable the real-time and continuous monitoring of environmental parameters in daily events, e.g., food safety [3-5], material corrosion [6-8], gas leakage [9], drug delivery status [10], and structural health of buildings [11-13], and wirelessly

exchange of data to an RFID reader or portable sniffer devices. Therefore, the RFID based technology may act as important building blocks for the ubiquitous internet-of-things (IoTs) and future 5G communication networks. In addition, RFID-based wireless sensors implemented by textile or wearable technologies could be used for dynamically detecting physiological signals of humans and animals, thereby facilitating a practice of healthcare IoTs, as well as the point-of-care testing (POCT). Since the society now is facing a crisis of global aging and pandemic [14], the rapid, low-cost, disposable and also environmental friendly POCT, and drive-through tests are in highly growing demands.

Generally speaking, a passive RFID system constituted by a reader that emits a modulated RF signal to the passive RFID tag. The tag includes an antenna and a microchip that could collect the received RF power and then strategically modulate the input impedance of antenna, and thus to modulate the backscattered RF signal [15, 16]. In such systems, the continuous-wave radio signal powering up the RFID tag will inevitably couple to the receivers/transmitters of the reader, thus leading to a strong crosstalk. Apart from the self-interference, there will be also other types of electromagnetic interferences that is necessary to be effectively suppressed, for example, the presence of clutters, echoes, and multipath scattering. Removing these noises are particularly crucial for conventional passive sensors since the information is typically encoded in the backscattering properties of the antennas, including resonant frequency shift noticed from the RCS data over a specific frequency range [17] or alternations in the shape of RSSI signatures. When an RFID tag is surrounded by multiple clutter objects, the overall radar cross-section (RCS) pattern becomes the sum of the total field contributions of each individual segments, given by [18]:

$$\sigma = |\sum_{p} \sqrt{\sigma_p} e^{i\phi_p}|^2, \qquad (11)$$

where $\sigma_p$ and $\phi_p$ are the RCS signagures and the relative phase of the *p*-th scatters. If a tag is placed in the vicinity of several clutter objects, such as a large-area metallic plate with $\max(\sigma) = (4\pi / \lambda^2) \times (\text{area})^2$, the backscattered signal from the RFID tag will be screened by the electromagnetic interreferences. To decouple the RCS of the RFID tag from the background noises, a two-step post-processing [see Eq. (12)] is normally conducted, given by [19]:

$$\sigma_{tag} = \left( \frac{S_{21}^{tag} - S_{21}^{isolation}}{S_{21}^{ref} - S_{21}^{isolation}} \right)^2 \sigma_{ref}, \qquad (12)$$

where $\sigma_{ref}$ is the RCS signature of the object that is already known, the scattering parameter $S_{21}^{tag}$ can be obtained in the presence state of the passive RFID tag, and $S_{21}^{isolation}$ is measured in the absence state of the passive RFID tag used for calibration to filter out the unwanted environmental effects in this RCS measurement. Unfortunately, Eq. (12) is only valid for a "static" environment and may be problematic in a dynamic environment involved with the motive clutter objects, for example, moving human bodies that have a time-varying $\sigma_{ref}(t)$.

Inspired by the recent "harmonic radar" platforms capable of tracking low-RCS objects [20-23], the proposed harmonic sensing telemetry shown in Fig. 37(a) has a reader that could transmit a CW signal at frequency $f_i$ to the tag, whereas can receive a modulated RF tone at frequency $2f_i$; such a frequency orthogonality is capable of effectively preventing noises induced by the background clutters and also the transceiver -receiver crosstalks in the reader side [24-26]. Furthermore, we will apply the frequency-hopping spread spectrum (FHSS) method to ensure the absolute value sensing [27, 28]. As illustrated in Fig. 37, the

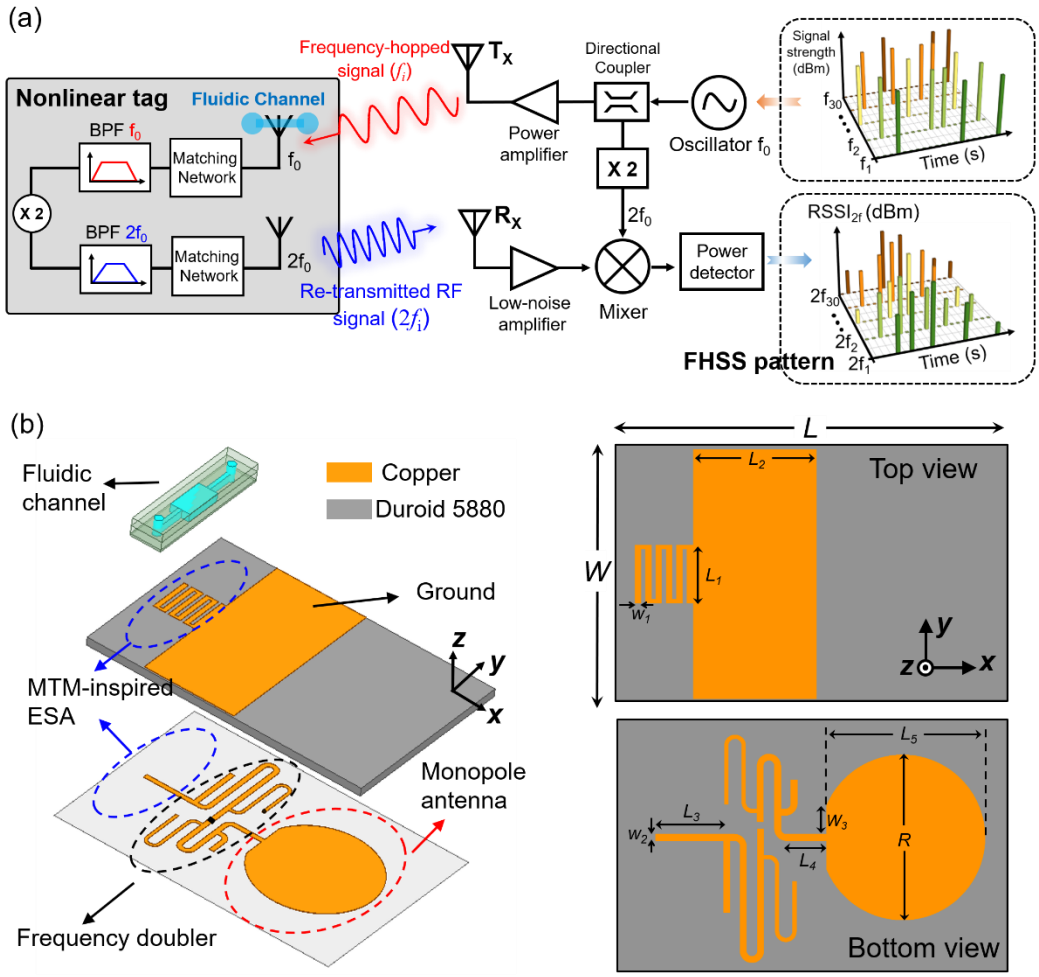


Figure 37. (a) Schematics of the FHSS-assisted harmonic sensing telemetry. (b) 3-D view and geometry of the proposed FHSS-assisted harmonic sensor.

telemetry system has a passive reader transceiver that launches a constant-stable frequency-hopping sequence with 30 channels [$f_1$, $f_2$,…, $f_{30}$] to the passive antenna sensor. Next, the hopped RF signal will be received by the antenna on the sensor, with the signal strength modulated by the SUT in the fluidic channel. Finally, the received RF tones will then undergo the frequency doubling process, i.e., [$f_1$, $f_2$,…, $f_{30}$] → [$2f_1$, $2f_2$,…, $2f_{30}$], and be re-transmitted to the portable sniffers. Figure 37(b) depicts a lightweight, low-cost harmonic sensor whose RCS in the upper frequency band could be tuned by, for instance, a transducer or microfluid cell that alternates the

antenna operating at $2f_0$; here, I will design a harmonic sensor comprising an electrically small narrow-band antenna working at $f_0$ that is reconfigurable by the liquid properties of the integrated microfluidic cell, a integrated frequency doubler, and also a wideband antenna covering the overall second harmonic bands [$2f_1$, $2f_2$,…, $2f_{30}$]. Finally, sensing of chemical or physical parameters in the tag could be retrieved by analyzing the multi-dimensional FHSS pattern among [$2f_1$, $2f_2$,…, $2f_{30}$].

In this chapter, I will first discuss design and practical implementation of the FHSS-assisted harmonic sensing system that will be used for wireless monitoring of liquid mixtures in the fluidic channel. In Section 5.2, I will experimentally study the characteristics of the proposed antennas with regard to reflection coefficient and impedance matching, as well as their radiation properties. Besides, I will assemble this ESA with a fluidic channel to form a antenna sensor and demonstrate its sensing capability with binary mixture containing different volume fraction of ethanol and water. In Section 5.3, I will demonstrate a clutter-resistive nonlinear and also passive telemetry scheme with this fully-passive harmonic sensor for implementing practical liquid monitoring in rich-scattering environments. Finally, I will draw a short conclusion in Section 5.4.

## 5.2 Antenna design and measurement

Fig. 37(b) sketches the geometry of the proposed harmonic transponder, which is constituded by a metamaterial-inspired electrical-small antenna (ESA) [29, 30], a passive frequency doubler, and

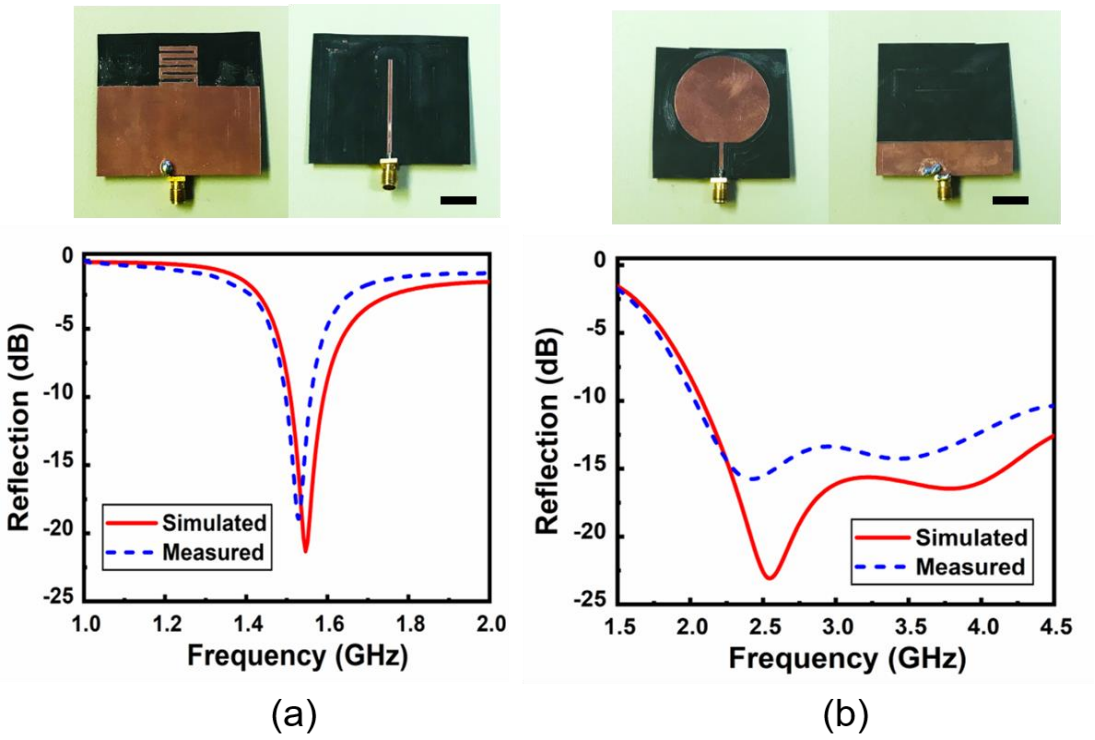


Figure 38. Photograph and measured reflection coefficients for (a) a metamaterial-inspired ESA and (b) a wideband monopole antenna.

Table IV: Summary of the dimensions in this harmonic transponder (unit: mm)

| Par. | $L$ | $W$ | $L_1$ | $L_2$ | $L_3$ | $L_4$ | $W_1$ | $W_2$ | $W_3$ | $R$ |
|---|---|---|---|---|---|---|---|---|---|---|
| Value | 85 | 60 | 14 | 30 | 16 | 9.5 | 1.5 | 1.58 | 6.6 | 38 |

a circular broadband monopole antenna. The summary of important design parameters are listed in Table IV. Inspired by the subwavelength resonant inclusions constituting the metamaterial, the proposed ESA has an inductive meander-line element that could compensate for the capacitive nature of the monopole formed by a short-stub [31]. Importantly, the electrical-based small antenna

coupled to the resonant parasitic elements could be matched to a 50 Ω source, without any introduction of a external matching network. Thanks to this *LC* resonator formed in a small dimension, the electrical size of the overall ESA, which includes the short monopole and its parasitic meander-line element, is still subwavelength, and thus, as could be readily understood according to the Chu limit [32], a narrowband resonance with high Q-factor can be achieved. By optimizing the length of the short stub and the total length of the parasitic meander line, good impedance matching with enhanced bandwidth and radiation efficiency could be simultaneously obtained. We should note that the metamaterial-inspired ESA not only make the antenna design easily and miniaturization, but also offers a narrow resonance linewidth, which is significant for enhancing the sensitivity and resolvability of the antenna sensors. In practice, the ESA is used as the fundamental tone receiver for reducing the overall area occupation of the antenna sensors. From Fig. 37(b), the two metal layers of the harmonic tag are separated by a Roger 5880 substrate with thickness of 0.508 mm, which has an electrical property of $\varepsilon_r = 2.2$ and $\delta = 0.0009$. In this work, the ANASYS High Frequency Structure Simulator (HFSS) [33] was used for simulation of the ESA and the Advanced Design Simulator (ADS) [34] was used for the design of the nonlinear circuit.

Figure 38 presents the photographs and measured reflection spectra for the proposed antennas. We find that the metamaterial-inspired ESA could resonate at 1.55 GHz with a -10 dB bandwidth of 124 MHz [Fig. 38(a)], whereas the circular monopole antenna displays a wideband resonance covering 2– 4.5 GHz for the second-harmonic frequency at 3.1 GHz [Fig. 38(b)]. The measured results agree well with the simulation ones, with a rather small fluctuation generated from fabrication or assembling errors, as well as the potential variations in the permittivity of the substrate.

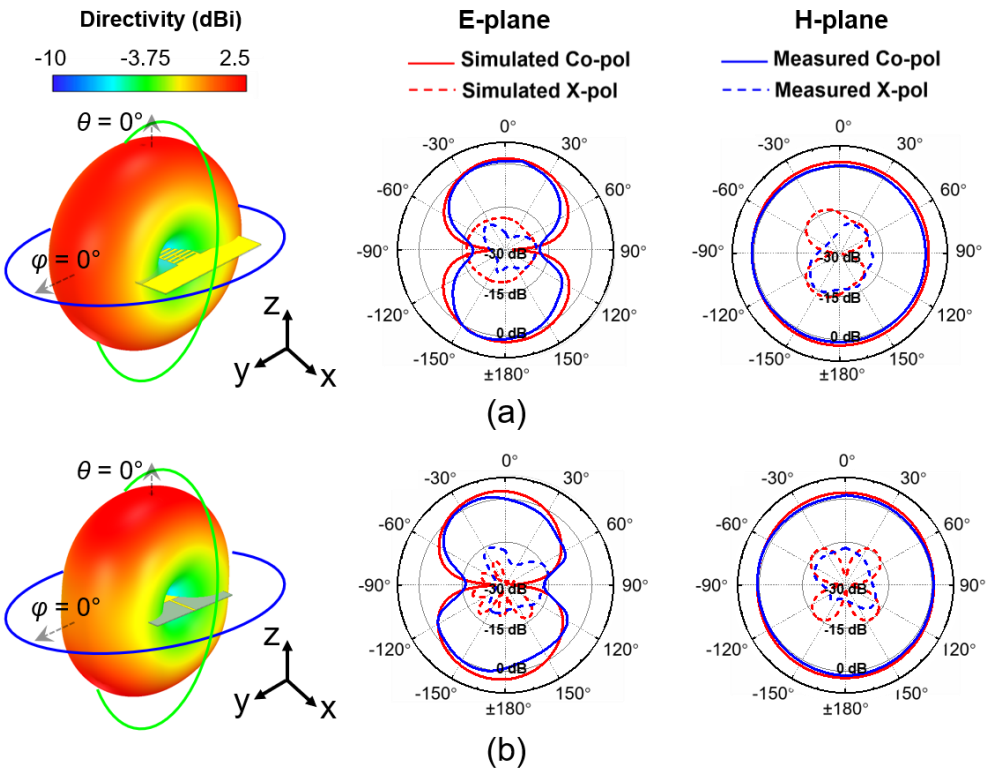


Figure 39. Radiation patterns for (a) the ESA at 1.55 GHz and (b) the monopole antenna at 3.1 GHz.

Figure 39 shows the simulated and measured radiation patterns of the proposed antennas at their resonant frequencies, which are respectively 1.55 GHz and 3.1 GHz. It is seen that in each case, the measured co-polarization radiation patterns maintaining omnidirectional radiation properties are in accordance with the simulated results, with a maximum measured gain of 2.32 dBi at 1.55 GHz for the narrow resonance ESA and 2.35 dBi at 3.11 GHz for the wideband circular monopole; a high co-polarization discrimination could be observed, with the cross-polarization <-15 dB on each plane. It should be also noted that thanks to low dielectric losses in the Roger 5880

substrate with loss tangent δ = 0.0009, the radiation efficiency of the antennas are both higher than 85 % at each frequency band of interest.

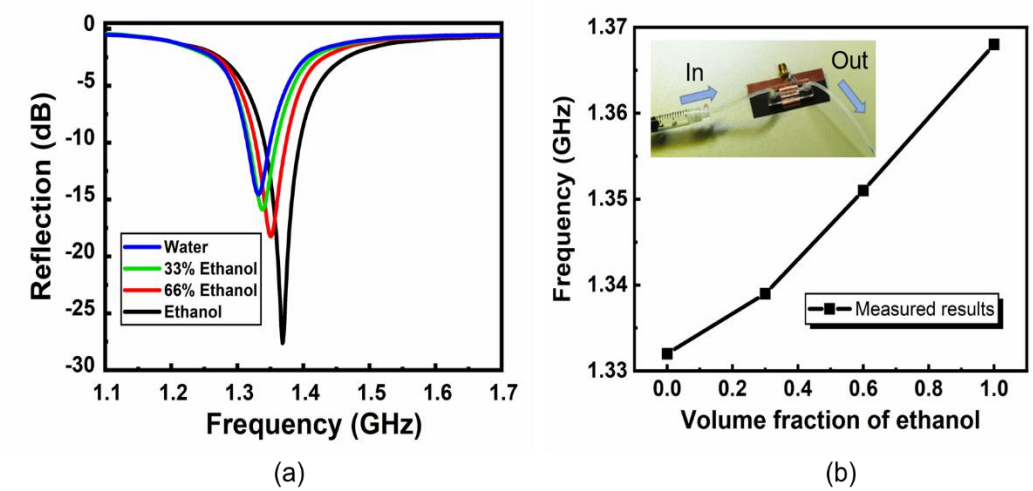


Figure 40. (a) Measured reflection spectra for the ESA integrated with a fluidic channel in response to different ethanol-water mixture. (b) Measured resonant frequency versus different volume fraction of ethanol.

Next, I demonstrate the sensing functionality of the ESA sensor. To precisely control the liquid volume, I fabricated a fluidic channel by means of Epilog Mini 24 laser cutter, which consists of three acrylic layers with thickness 0.1 mm, 1 mm, and 1 mm, respectively, and subsequently integrated onto the ESA and connected to two plastic tubes for serving as mixtures' inlet and outlet [Fig. 40]. Here, we should note that even though a thin channel could allow strong electrical localization, a 1 mm acrylic layer, however, can also provide a sufficient volume to achieve the maximum resonance frequency drift (i.e.

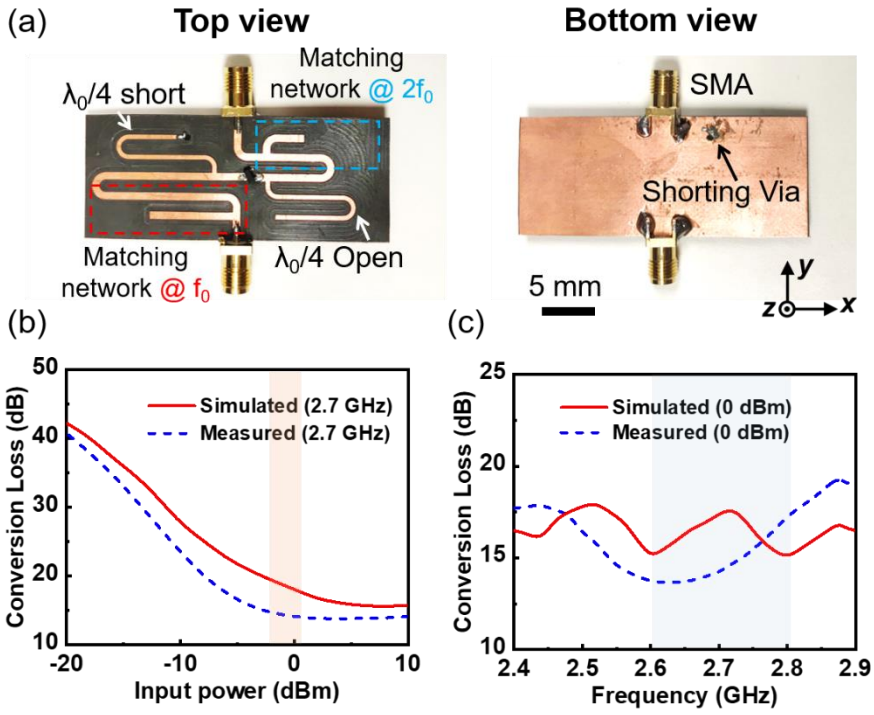


Figure 41. (a) Photographs of a compact passive frequency doubler and its conversion loss as a function of (b) input power level at 2.7 GHz and (c) output frequency at 0 dBm input power level.

sensitivity). As for the SUT, for brevity, we use a binary mixture made of ethanol and water with different volume ratios, namely, ethanol/water = 100 %, 66 %, 33 %, and 0 %, corresponding to (real-part) effective relative permittivity $\varepsilon_r$ = 24.3, 35.3, 61, and 80 [35]. The Agilent N5222A PNA microwave network analyzer was used to record the reflection coefficients of the fluidic-loaded ESA. Fig. 40 reports the measured reflection coefficients, presenting that with the decrease of the volume ratio of ethanol to water, resonance frequency of the ESA can downshift from 1.368 GHz to 1.334 GHz. Such a phenomenon can be comprehensively explained by the proven perturbation theory, which states that the resonant frequency of the antenna can be perturbated in response to the dielectric properties of the SUTs injected into the fluidic channel. Fig. 40(b) summaries the

measurement results for different concentrations of SUTs, exhibiting excellent linearity and sensitivity of this fluidic channel integrated ESA in determination of the volume fraction in binary liquid mixtures.

The antennas studied here were subsequently connected to a passive frequency doubler [Fig. 41] for forming a passive harmonic sensing telemetry. The top and bottom views of the frequency doubler are depicted in Fig. 41(a), where a shunt quarter-wavelength short-circuited (open-circuited) stubs are placed in the front (back)of a Schottky diode to act as bandpass filters (i.e., BPFs). At two ports, compact matching networks are designed to match the impedance into the 50 Ω source and load, such that the injected RF signal at only fundamental frequency could pass through the input network and reach the diode for frequency multiplication, whereas the matching network and BPF at the output will short the fundamental tone, but instead let the harmonics go through. Fig. 41(b) presents the measured conversion loss of the frequency doubler at different input powers, in which we find that at 2.7 GHz, a minimum conversion loss around 13.5 dB at 0 dBm input power level could be achieved. Fig. 41(c) shows the conversion loss versus t frequency at 0 dBm input power level, implying that within the second harmonic frequency band 2.6 GHz – 2.8 GHz, the doubling efficiency is relatively high with a < 5 dB fluctuation. Significantly, a lowest conversion loss ~13.5 dB could be received at 2.7 GHz.

### 5.3 Passive harmonic sensor

In this section, I connect the antennas to the aforementioned passive frequency doubler for assembling a fully passive wireless sensor [Fig. 42] and will adopt the bistatic measurement configuration to demonstrate this clutter-resistive telemetry. In this system, the backscattered second-harmonic RSSI received by the reader could form a FHSS pattern, whose peak frequency may be

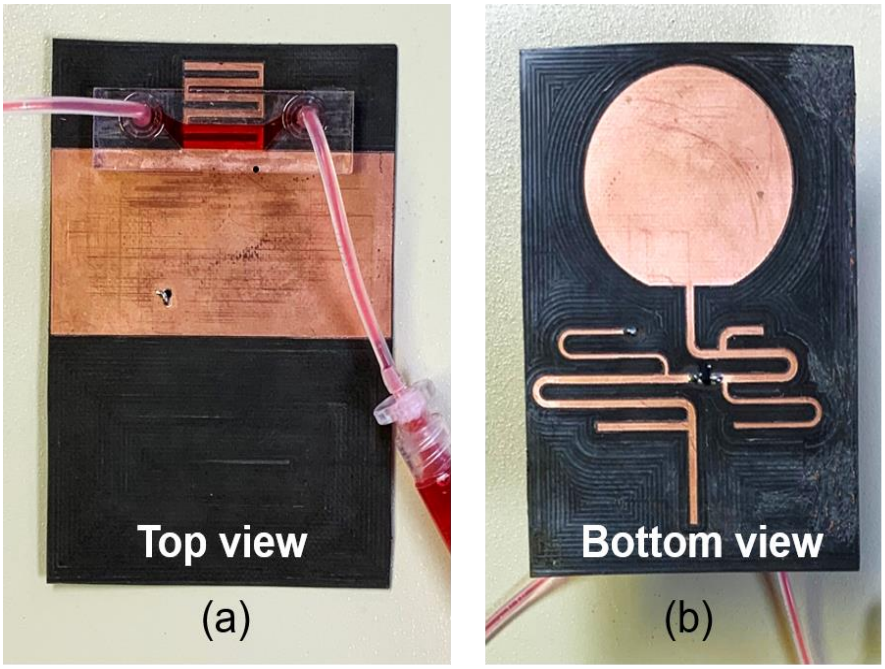


Figure 42. (a) Top and (b) bottom views of the fully-passive low-profile harmonic sensor for wireless binary mixture sensing.

interrelated with the specific properties of the SUTs. Generally speaking, the free-space second-harmonic RSSI could be estimated by the Friis transmission formula, given by[36]:

$$P_r = P_t\left(\frac{\lambda_0}{4\sqrt{2}\pi R}\right)^4 \frac{G_{t,reader}(f_0)G_{r,tag}(f_0)G_{t,tag}(2f_0)G_{r,reader}(2f_0)}{L_{sys}} \tag{13}$$

where $G_{r,tag}$ is the realized gain of the receiver antenna (here, referring to narrowband ESA) of the tag, $G_{t,tag}$ is the realized gain of the transmitter antenna (i.e., broadband circular monopole) of the tag, $G_{t,reader}$ and $G_{r,reader}$ respectively denote the realized gain of transmitter $T_x$ and receiver $R_x$ of

the reader, $R$ is the distance between the tag and the reader, $L_{sys}$ is the total system loss that includes the conversion loss of the frequency doubler and any conduction or dielectric loss in the tag, and $L_p = \left(4\pi\sqrt{2R_1R_2}/\lambda_0\right)^4$ is the free-space path loss. The important setup parameters are summarized here: $P_t$ = 20 dBm, $R$ = 1.5 m, $G_{t,reader}$ = 12.5 dBi at 1.55 GHz, and $G_{r,reader}$ = 15.0 dBi at 3.1 GHz.

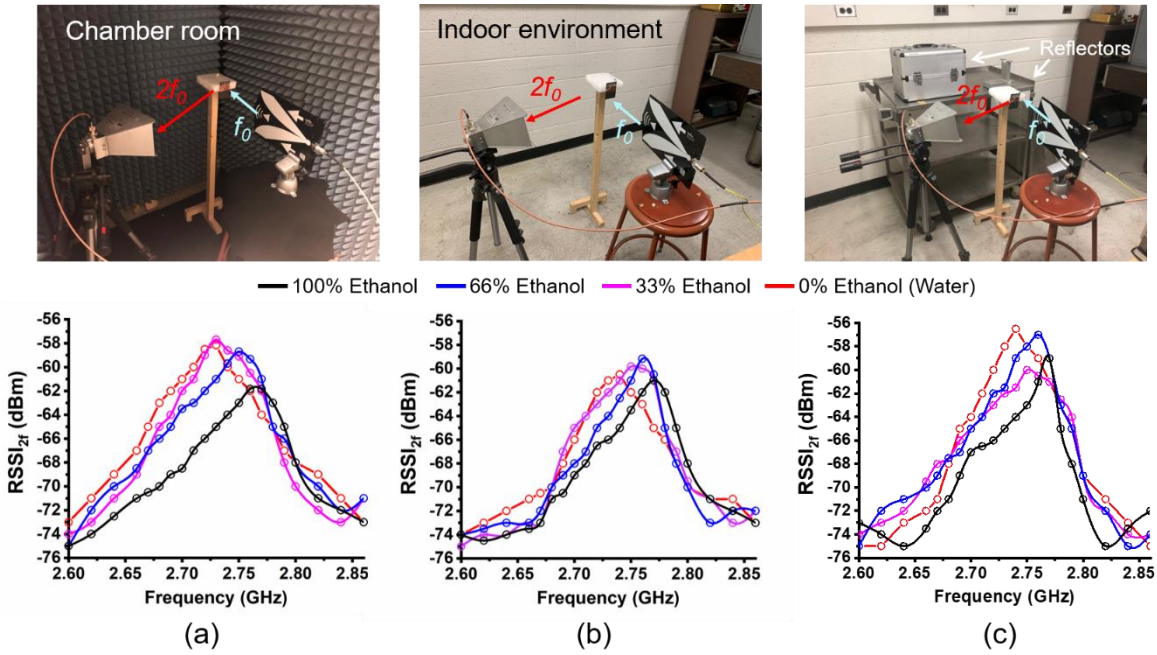


Figure 43. Experimental configuration and received FHSS for the clutter-resistive telemetry technique in the (a) anechoic chamber, (b) noisy indoor environment, and (c) rich-scattering environment with several metal reflectors.

This proposed far-field wireless sensing scheme is detailed in the following. We expect from Eq. (13) that the received power $P_r$ (also referring to the received signal strength indicator (RSSI)) are proportional to the realized gains of the antennas in the harmonic tag, i.e., $G_{r,tag}$ and

$G_{t,tag}$. If binary mixture is injected into the fluidic channel, the gain of the monopole antenna $G_{t,tag}$ remains fairly constant with only a ±0.6 dB fluctuation possibly caused by fabrication or assembly errors, or secondary effects including temperature-dependent dielectric variations, whereas the ESA's gain $G_{r,tag}$ is relatively sensitive to the SUTs' concentration. Consequently, the SUT information will be encoded inside the backscattered harmonic signals, generating the downshift of the FHSS pattern, as illustrated in Fig. 43. It is evidently seen from Fig. 43(a) that the peak RSSI of FHSS pattern could be sensitively configured from 2.772 to 2.731 GHz, at different volume fractions of ethanol. Fig. 43 also reports the FHSS patterns measured in three different environments, such as the noise-free anechoic chamber situation, practical indoor environment filled with clutters and multipath scattering, and rich-scattering environment with several metal reflectors that have large RCS signatures. In this measurement, apart from environmental conditions, all other telemetry parameters such as distance, gain of antennas, etc. keep the same. From Figs. 43(b) and 43(c), we can find that regardless of the electromagnetic interferences, the frequency detuning trend of the FHSS pattern looks unchanged, such that we could conclude that the FHSS-assisted, harmonic-based passive telemetry technique may be able to provide an absolute accurate sensing platform with a good reliability.

For making a comparison, we also wirelessly interrogate the same SUTs adopting a traditional passive sensor, enabled by a similar ESA terminated only with a 50 Ω load without any frequency modulation devices. Figure 44 presents the telemetry diagram and the measured FHSS patterns for the traditional backscattered sensor in the anechoic chamber and also noisy environments, from which we find that even though the RFID sensor could operate well in the noise-free chamber, it fails to monitor the binary mixtures in a rich-scattering environment

involved with metal reflectors. Figures 45(a) and 45(b) conclude the measured values of the FHSS pattern as a function of the different binary mixtures

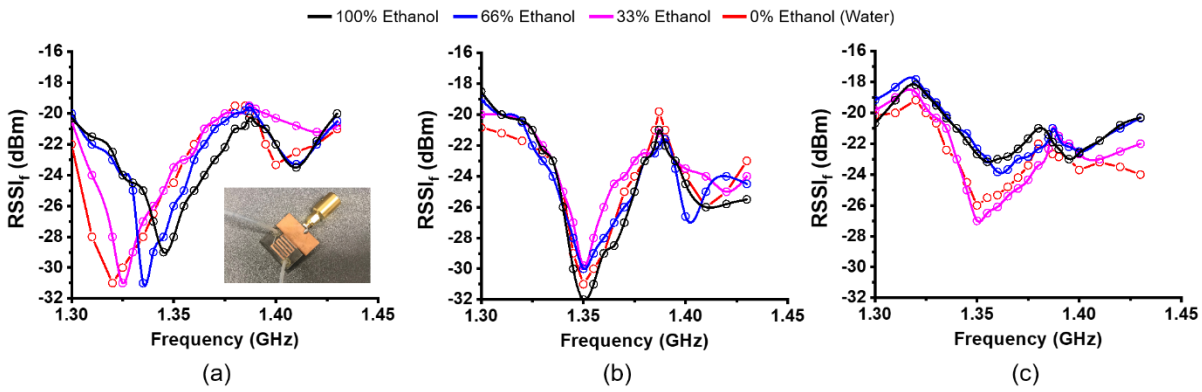


Figure 44. Measured FHSS for the conventional RFID sensor in (a) anechoic chamber, (b) noisy indoor environment and (c) rich-scattered indoor environment with several metal reflectors.

in different environment. Obviously, increasing the number of scatters does not affect the sensing performance of the proposed FHSS-assisted harmonic telemetry scheme, whereas it can considerably deteriorate the sensing capability of the conventional wireless sensing method. From Fig. 45(a), we can also define the sensitivity as the slope of the curve, i.e., 0.4 MHz/1%, which means that a 5 % increase in the volume fraction of ethanol could cause the peak frequency to upshift by 2 MHz.

Next, we consider the influence of the interrogation distance about the RSSI. Figure 46(a) reports the FHSS patterns measured at different distances in the noisy indoor environment. Notice that except the sensor-to-sniffer distance $R_2$, all other measurement conditions remain the same. Apparently, it is seen from Fig. 46(a) that the peak frequency position achieved from FHSS pattern is rather independent of the sensing distance, thus confirming that the proposed harmonic-FHSS

pattern analysis is able to provide an absolute and accuracy sensing scheme. Figures 46(b) and 46(c) present the peak RSSI values at different interrogation distances for the harmonic (2.76 GHz) and fundamental frequencies (1.38 GHz), respectively. We find that from Fig. 46(b), the $RSSI_{2f}$ at 2.76 GHz can decrease linearly if the interrogation distance is increased, and that a robust sensing with a distance of 5.0 m (i.e., $R_1$ = 1.5 m, $R_2$ = 5.0 m) could be still obtained with a -80 dBm noise floor level. By contrast, the $RSSI_f$ at fundamental frequency 1.38 GHz exhibits an uncorrelated relationship with regard to the variations of the interrogation distance. On the other hand, when the conventional backscatter sensor is explored, it would function well in the anechoic chamber, in other words, the peak RSSI could also decrease monotonously with increasing the interrogation distances, obeying to what predicted by the Friis' equations. However, it can not reliably recognize the binary mixture type related to the effective dielectric constant, if the tag is located in the noisy or rich-scattering indoor environments.

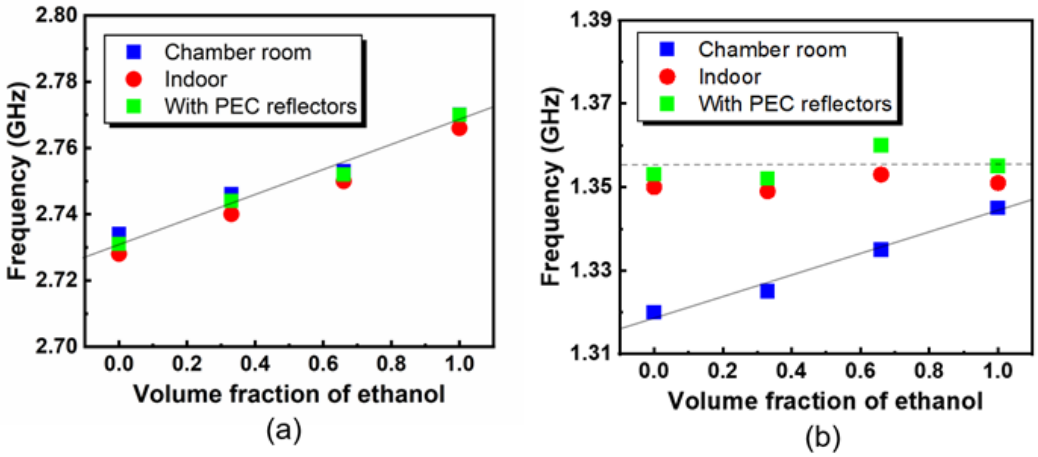


Figure 45. Peak frequency against different binary mixtures for (a) nonlinear harmonic sensor and (b) conventional RFID sensor in different environments.

Finally, it is worthwhile emphasizing that although RF signal attenuation is more pronounced at $2f_0$ that renders a larger path loss in contrast to those in the linear RFID systems, the measured second-harmonic RSSI is somehow independent of the scattering cross section of the tag itself and is therefore insensitive to the complicated environments full of high-clutter objects. Furthermore, in practical wireless interrogation applications, the frequency dependency of path loss may be less obvious. As a representative example, in the two-rays ground-reflection model considering two antennas with different heights (i.e.m $h_{sniffer}$ and $h_{tag}$) above the ground, the path loss for $R \gg 4\pi h_{sniffer} h_{tag} / \lambda$ could be approximately derived as [37]:

$$L_p \approx \left( \frac{h_{sniffer} h_{tag}}{R^4} \right)^4 \left( \frac{\sin \frac{2\pi}{\lambda} \frac{h_{sniffer} h_{tag}}{r^2}}{\frac{2\pi}{\lambda} \frac{h_{sniffer} h_{tag}}{r^2}} \right)^2 \approx \left( \frac{h_{sniffer} h_{tag}}{R^2} \right)^4 . \qquad (14)$$

In this case, the path loss factor is relatively independent of the carrier frequency of radio signal, and consequently, the nonlinear interrogation scheme, i.e., harmonic sensing telemetry may have a path loss comparable to the traditional linear passive RFID systems in free space.

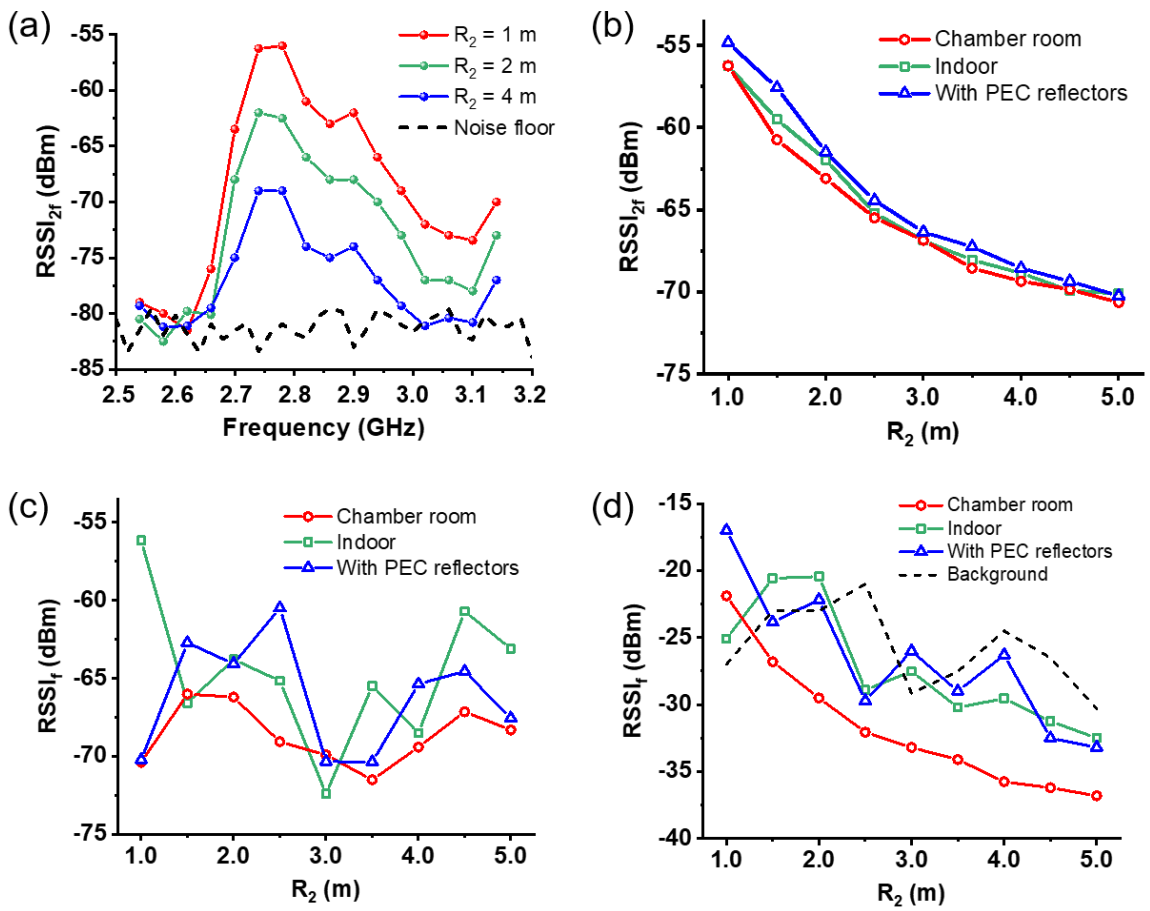


Figure 46. (a) FHSS pattern of the harmonic sensing telemetry versus different interrogation distances. (b) Detected RSSI versus the interrogation distance for the harmonic sensor at (b) the second-harmonic frequency (2.76 GHz) and (c) the fundamental frequency (1.38 GHz). (d) is similar to (c), but for a conventional backscatter RFID sensor at 1.38 GHz.

## 5.4 Conclusion

I have proposed a generalized harmonic sensing platform assisted by FHSS technique for long-range interrogation. As a practical example, I have demonstrated this wireless measurement technique with the interrogation of a fully-passive harmonic transponder having a fluidics-reconfigurable antenna sensor. I have successfully employed the harmonic sensor and this system

for remotely monitoring liquid mixtures in both the anechoic chamber and the noisy indoor environment full of several high-clutter objects. These results show that this FHSS-assisted harmonic RSSI analysis coud be very robust to the presence of background electromagnetic interreferences. However, similar performance is not possible with the traditional approaches like measurement of backscattering from a passive resonant RFID sensor. I envision that this harmonic sensing telemetry scheme and the overall system proposed here may benefit various wireless sensing and telemetering in the future fields of lab-on-a-chip measurements and IoTs, as well as rapid healthcare tests.

## REFERENCES


[1] L. Catarinucci, D. de Donno, L. Mainetti, L. Palano, L. Patrono, M. L. Stefanizzi *et al.*, "An iot-aware architecture for smart healthcare systems," *IEEE Internet of Things Journal,* vol. 2, no. 6, pp. 515-526, Dec 2015.

[2] Y. W. Xu, L. H. Dong, H. D. Wang, X. Z. Xie, and P. Wang, "Surface crack detection and monitoring in metal structure using rfid tag," *Sensor Review,* vol. 40, no. 1, pp. 81-88, Jan 13 2020.

[3] Z. Q. Gao and X. P. Zhao, "Nano-silver conductive ink inkjet printing rfid tag antenna," *Research on Food Packaging Technology,* vol. 469, pp. 322-325, 2014.

[4] R. Raju, G. E. Bridges, and S. Bhadra, "Wireless passive sensors for food quality monitoring: Improving the safety of food products," *IEEE Antennas and Propagation Magazine,* vol. 62, no. 5, pp. 76-89, Oct 2020.

[5] P. Fathi, N. C. Karmakar, M. Bhattacharya, and S. Bhattacharya, "Potential chipless rfid sensors for food packaging applications: A review," *IEEE Sensors Journal,* vol. 20, no. 17, pp. 9618-9636, Sept1, 2020.

[6] S. Soodmand and G. Y. Tian, "Comments on "uhf rfid tag antenna-based sensing for corrosion detection and characterization using principal component analysis"," *IEEE Transactions on Antennas and Propagation,* vol. 66, no. 11, pp. 6465-6465, Nov 2018.

[7] J. Zhang and G. Y. Tian, "Uhf rfid tag antenna-based sensing for corrosion detection & characterization using principal component analysis," *IEEE Transactions on Antennas and Propagation,* vol. 64, no. 10, pp. 4405-4414, Oct 2016.

[8] S. Deif and M. Daneshmand, "Multiresonant chipless rfid array system for coating defect detection and corrosion prediction," *IEEE Transactions on Industrial Electronics,* vol. 67, no. 10, pp. 8868-8877, Oct. 2020.

[9] A. S. Almazyad, Y. M. Seddiq, A. M. Alotaibi, A. Y. Al-Nasheri, M. S. BenSaleh, A. M. Obeid *et al.*, "A proposed scalable design and simulation of wireless sensor network-based long-distance water pipeline leakage monitoring system," *Sensors,* vol. 14, no. 2, pp. 3557-3577, Feb 2014.

[10] H. J. Lu, Y. Hong, Y. Y. Yang, Z. B. Yang, and Y. J. Shen, "Battery-less soft millirobot that can move, sense, and communicate remotely by coupling the magnetic and piezoelectric effects," *Advanced Science,* vol. 7, no. 13, Jul 2020.

[11] A. M. J. Marindra and G. Y. Tian, "Chipless rfid sensor tag for metal crack detection and characterization," *IEEE Transactions on Microwave Theory and Techniques,* vol. 66, no. 5, pp. 2452-2462, May 2018.

[12] S. Caizzone, E. DiGiampaolo, and G. Marrocco, "Wireless crack monitoring by stationary phase measurements from coupled rfid tags," *IEEE Transactions on Antennas and Propagation,* vol. 62, no. 12, pp. 6412-6419, Dec 2014.

[13] A. M. J. Marindra and G. Y. Tian, "Chipless rfid sensor for corrosion characterization based on frequency selective surface and feature fusion," *Smart Materials and Structures,* vol. 29, no. 12, Dec 2020.

[14] Y. Y. Zheng, Y. T. Ma, J. Y. Zhang, and X. Xie, "Covid-19 and the cardiovascular system," *Nature Reviews Cardiology,* vol. 17, no. 5, pp. 259-260, May 2020.

[15] Z. L. Lu, "The application of rfid technology in the internet of things and its development prospect," *2017 7th International Conference on Education and Sports Education (Ese 2017), Vol 3,* vol. 76, pp. 483-487, 2017.

[16] I. Cappelli, A. Fort, M. Mugnaini, E. Panzardi, A. Pozzebon, M. Tani *et al.*, "Battery-less hf rfid sensor tag for soil moisture measurements," *IEEE Transactions on Instrumentation and Measurement,* vol. 70, 2021.

[17] L. Yang, R. W. Zhang, D. Staiculescu, C. P. Wong, and M. M. Tentzeris, "A novel conformal rfid-enabled module utilizing inkjet-printed antennas and carbon nanotubes for gas-detection applications," *IEEE Antennas and Wireless Propagation Letters,* vol. 8, pp. 653-656, 2009.

[18] M. I. Skolnik, *Radar handbook, third edition*. McGraw-Hill Education, 2008.

[19] E. Perret, *Radio frequency identification and sensors: From rfid to chipless rfid*. Wiley, 2014.

[20] D. Mascanzoni and H. Wallin, "The harmonic radar - a new method of tracing insects in the field," *Ecological Entomology,* vol. 11, no. 4, pp. 387-390, Nov 1986.

[21] J. R. Riley, A. D. Smith, D. R. Reynolds, A. S. Edwards, J. L. Osborne, I. H. Williams *et al.*, "Tracking bees with harmonic radar," *Nature,* vol. 379, no. 6560, pp. 29-30, Jan 4 1996.

[22] L. Zhu, N. Alkhaldi, H. M. Kadry, S. Liao, and P. Y. Chen, "A compact hybrid-fed microstrip antenna for harmonics-based radar and sensor systems," *IEEE Antennas and Wireless Propagation Letters,* vol. 17, no. 12, pp. 2444-2448, Dec 2018.

[23] L. Zhu, N. Alsaab, M. M. C. Cheng, and P. Y. Chen, "A zero-power ubiquitous wireless liquid-level sensor based on microfluidic-integrated microstrip antenna," *IEEE Journal of Radio Frequency Identification,* vol. 4, no. 3, pp. 265-274, Sep 2020.

[24] M. Hajizadegan, M. Sakhdari, L. Zhu, Q. S. Cui, H. Y. Huang, M. M. C. Cheng *et al.*, "Graphene sensing modulator: Toward low-noise, self-powered wireless microsensors," *IEEE Sensors Journal,* vol. 17, no. 22, pp. 7239-7247, Nov 15 2017.

[25] L. Zhu, H. Y. Huang, M. M. C. Cheng, and P. Y. Chen, "Compact, flexible harmonic transponder sensor with multiplexed sensing capabilities for rapid, contactless microfluidic diagnosis," *IEEE Transactions on Microwave Theory and Techniques,* vol. 68, no. 11, pp. 4846-4854, Nov 2020.

[26] L. Zhu, M. Farhat, Y. C. Chen, K. N. Salama, and P. Y. Chen, "A compact, passive frequency-hopping harmonic sensor based on a microfluidic reconfigurable dual-band antenna," *IEEE Sensors Journal,* vol. 20, no. 21, pp. 12495-12503, Nov 1 2020.

[27] H. Y. Huang, P. Y. Chen, C. H. Hung, R. Gharpurey, and D. Akinwande, "A zero power harmonic transponder sensor for ubiquitous wireless mu l liquid-volume monitoring," *Scientific Reports,* vol. 6, Jan 6 2016.

[28] L. Zhu, and P. Y. Chen, "A compact, zero-power and low-noise harmonic-transponder for liquid and moisture sensing," in 2019 *IEEE International Symposium on Antennas and Propagation and USNC-URSI Radio Science Meeting,* Atlanta, GA, USA, USA, 2019.

[29] A. Erentok and R. W. Ziolkowski, "Metamaterial-inspired efficient electrically small antennas," *IEEE Transactions on Antennas and Propagation,* vol. 56, no. 3, pp. 691-707, Mar 2008.

[30] R. W. Ziolkowski, P. Jin, and C. C. Lin, "Metamaterial-inspired engineering of antennas," *Proceedings of the IEEE,* vol. 99, no. 10, pp. 1720-1731, Oct 2011.

[31] P. Y. Chen, H. Huang, and C. H. Hung, "Compact metamaterial-enclosed wireless sensors with subtle perception of internal physical events," *Applied Physics Letters,* vol. 107, no. 19, Nov 9 2015.

[32] N. Zhu and R. W. Ziolkowski, "Active metamaterial-inspired broad-bandwidth, efficient, electrically small antennas," *IEEE Antennas and Wireless Propagation Letters,* vol. 10, pp. 1582-1585, 2011.

[33] *ANSYS 2020 R1 Academic Research Electromagnetics Suite.* Released in 2020. ANSYS, Inc., Southpointe 2600 Ansys Drive Canonsburg, PA, USA.

[34] Keysight PathWave Advanced Design System (ADS) 2020. Released in 2020. Keysight Technologies, 1400 Fountaingrove Parkway Santa Rosa, CA, USA.

[35] K. Saeed, R. D. Pollard, and I. C. Hunter, "Substrate integrated waveguide cavity resonators for complex permittivity characterization of materials," *IEEE Transactions on Microwave Theory and Techniques,* vol. 56, no. 10, pp. 2340-2347, Oct 2008.

[36] J. A. Shaw, "Radiometry and the friis transmission equation," *American Journal of Physics,* vol. 81, no. 1, pp. 33-37, Jan 2013.

[37] R. T. S, *Wireless communications: Principles and practice, 2nd edition*. Pearson Education, 2010.

[38] R. Janaswamy, *Radiowave propagation and smart antennas for wireless communications*. Springer US, 2006.

# VI. COMPACT, FLEXIBLE HARMONIC TRANSPONDER SENSOR WITH MULTIPLEXED SENSING CAPABILITIES FOR RAPID, CONTACTLESS MICROFLUIDIC DIAGNOSIS



In this chapter, I discusses a flexible harmonic sensor, which is capable of performing multiplexed fluidic sensing. The harmonic sensor consists of two frequency-reconfigurable electrically-small antennas (ESAs) loaded with fluidic channels that are used for receiving radio-frequency waves at fundamental frequencies, and a broadband monopole antenna for re-transmitting the second-harmonics to a portable sniffer. I show that the injection of liquid samples into the fluidic channels, can dynamically detune the resonant frequencies of the ESAs, which then could be precisely extracted by processing the shift of the RSSI patterns. Additionally, we also demonstrate a prototype of rapid and multiplexed sample detection with the proposed harmonic sensor.

## 6.1 Introduction

In recent years, with the rapid development of smart devices, the power-saving wireless sensing techniques have drawn rapidly growing interest as the integration of wireless networks with the sensing nodes could provide significant advantages such as higher data rate, a real-time monitoring, and the capability to synchronously upload information to the cloud for data analysis [1], [2]. The first wireless smart sensors could be dated back to 2000 [3], and since then, it has been widely developed in monitoring several environment parameters [4], biological parameter [5], humidity [6], and temperature [7], to name a name. Unfortunately, to date, most wireless devices are still active devices, i.e., they normally require an external power source, like an integrated energy harvester or a battery, which inevitably adds a significant amount of complexity

and potential error sources to the overall system [8]. To enhance durability and robustness of the system, as well as to reduce maintenance costs, a number of battery-free wireless sensors have been proposed, which could be divided into two categories. The first one is based on the near-field inductive or capacitive coupling mechanism, which has been proved to be effective for versatile LC-resonator based biomedical sensors [9]-[13] and capacitive pressure or humidity sensors [14]-[16]. However, this near-field coupling scheme has the widely-known disadvantages of short interrogation distance that is limited within several inches, which poses an inconvenience for the practical sensing applications. In order to overcome such limitations, electromagnetic backscattering techniques have been exploited for performing a longer wireless sensing. In this vein, microstrip antenna based sensors and also passive radio frequency identification sensors have been proposed for remotely monitoring environmental changes [17]-[19]. However, although such systems can have longer interrogation distance, these backscatter sensors are normally vulnerable to direct coupling with the scattering interferences or clutters surrounding them.

Very recently, compact and passive harmonic sensors are gaining attentions. Analogous to a harmonic radar [20] that has been utilized in tracking objects with a small radar cross-section (RCS) signature [21]-[23], a harmonic sensor could launch and detect orthogonal signals to avoid clutters, multiple interferences, and also crosstalks between $T_x$ and $R_x$ [24]-[26]. These harmonic sensors

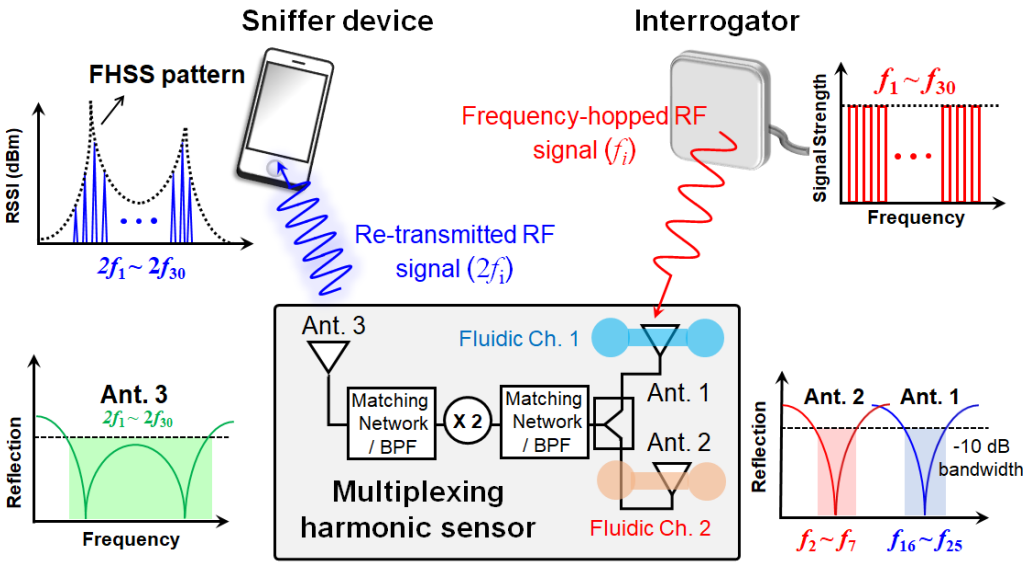


Figure 47. Schematics of the compact multiplexed harmonic sensor based on microstrip antennas.

have been generalized into fields of remote sensing [27], [28], humidity sensing [29], localization of underground buried assets [30]-[32], and even non-invasive detection of critical symbols in healthcare applications [33]-[36]. Especially, facing the crisis of global aging and pandemic (e.g., COVID-19) [37], rapid, low cost, and disposable point-of-care (POC) tests and drive-through tests are in exponentially growing demands. Recently, I have proposed a passive harmonic transponder hybridized with an antenna sensor for monitoring liquid levels in medical and healthcare applications [38], [39]. This technique is based on the harmonic RSSI data under the FHSS of UHF RFID signals, which is suitable for convenient POC and also drive-through tests. In fact, the already popularly deployed RFID toll tag readers could be used as the interrogators, and the healthcare workers may use smartphones as the data sniffers for drive-through tests. Such a contactless, wireless sensing platform may not only drastically improve the throughput, but also reduce the risk for the healthcare workers if testing with contagious diseases. Even though the

existing harmonics-transponder sensors have various advantages in healthcare and IoT applications, they still maintain certain intrinsic limitations. As a representative example, they generally lack the ability to simultaneously deal with multiple test channels or multiple test parameters [40]-[42], which may not satisfy the complexity requirement of many healthcare applications in practice. Another one is the lack of good mechanical flexibility and compactness, which further limits their applications of these harmonic sensors in the fields of textile or wearable electronics. For example, harmonic-based antenna sensors in Refs. [41], [42] were based on semi-rigid, dual- or multi-mode microstrip patch antennas (i.e., cavities with open sidewalls), of which only a specific cavity mode is perturbed by the dielectric loading, whereas others remain unchanged. Taking into account the complicated modal profile in a compact cavity, it is rather difficult to design a multiplexing sensor.

Therefore, in this chapter, I propose a lightweight and flexible multiplexing harmonic-transponder sensor, which allows for rapid, in-situ detection of at least two types of liquid samples. As sketched in Fig. 47, the system consists of a transceiver ($T_x$) that transmits a constant-strength frequency-hopping sequence with overall 30 channels [$f_1, f_2,\ldots, f_{30}$] to the multiplexed harmonic sensor. The frequency-hopped signal will be received by the sensor's ESAs, with strength modulated by the SUT in the fluidic channels. The received RF signals will then undergo the frequency doubling (i.e., [$f_1, f_2,\ldots, f_{30}$] $\rightarrow$ [$2f_1, 2f_2,\ldots, 2f_{30}$]) and is re-transmitted to the sniffers.

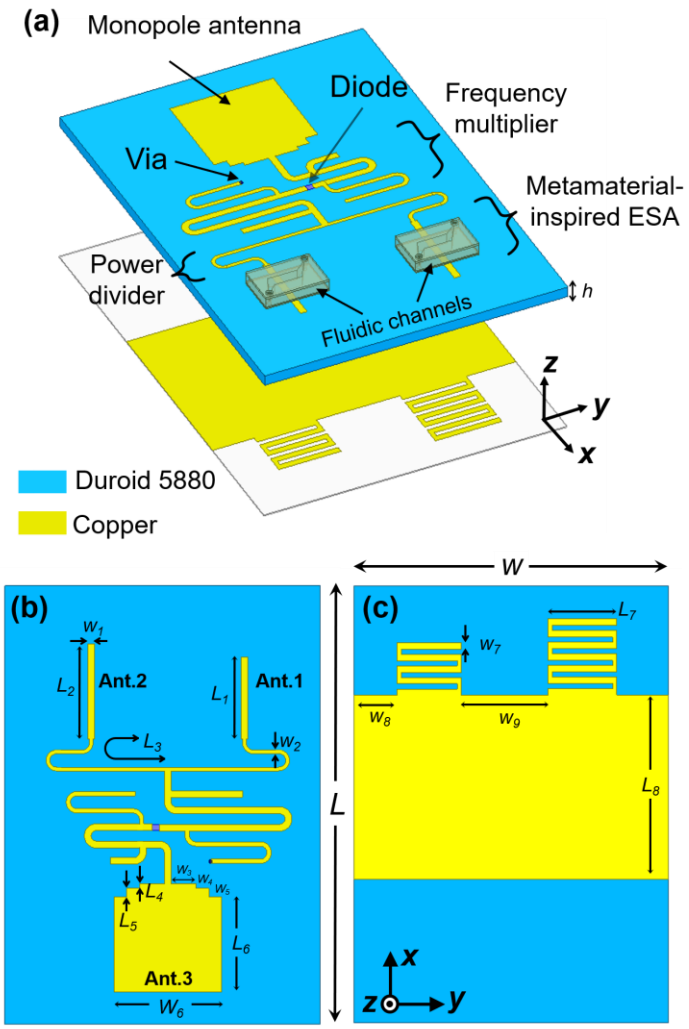


Figure 48. Geometry of the proposed harmonic transponder sensor consisting of two ESAs integrated with two separated fluidic channels, a frequency doubler, a power divider, and a broadband rectangular monopole antenna. (a) 3-D view, (b) top view, and (c) bottom view of this harmonic sensor.

Finally, the dielectric property of the SUT could be retrieved by postprocessing the high-dimensional frequency-hopping spread spectrum (FHSS) pattern [$2f_1$, $2f_2$,…, $2f_{30}$]. We emphasize that the proposed harmonic sensor could be extended into a multiplexed sensing platform that can simultaneously monitor several SUTs, with good isolation and ignorable mutual coupling. The proposed technique may be of interest for emerging textile, wearable, and implantable electronic

devices. In the following chapter, I will discuss the design and also its practical implementation of this flexible multiplexing harmonic sensor for contactlessly sensing two types of binary mixtures.

Table V: Summary of dimensions with regard to the harmonic tag (Unit: mm)

| Par. | $L$ | $W$ | $L_1$ | $L_2$ | $L_3$ | $L_4$ | $L_5$ | $L_6$ | $L_7$ | $L_8$ |
|---|---|---|---|---|---|---|---|---|---|---|
| Value | 100 | 70 | 19 | 22 | 42 | 1 | 2 | 22 | 16 | 43 |
| Par. | $W_1$ | $W_2$ | $W_3$ | $W_4$ | $W_5$ | $W_6$ | $W_7$ | $W_8$ | $W_9$ | |
| Value | 1.58 | 0.85 | 5.7 | 3 | 3 | 25 | 1.5 | 10 | 20 | |

## 6.2 Design and Measurement of Harmonic Transponders

Fig. 48(a) presents the 3D geometry of the harmonic transponder, comprising two metamaterial-inspired electrical small antennas (ESAs) [43]-[45], a power divider, a passive frequency doubler, and a rectangular monopole with their optimal parameters concluded in Table V. Metamaterial-inspired ESAs are commonly composed of *LC* resonant structures, which are inspired by the design of unit cells (or meta-atoms) [46]-[49] constituting metamaterials. Hence, compared to metamaterial-based ESAs, metamaterial-inspired ESAs could be more readily designed and implemented. Here, the metamaterial-inspired ESAs (i.e., Ant.1 and Ant. 2 in Fig. 47) utilized for receiving fundamental tones consist of a short stub and a grounded meander line. The inductive nature of the meander-line meta-atom [43] could compensate

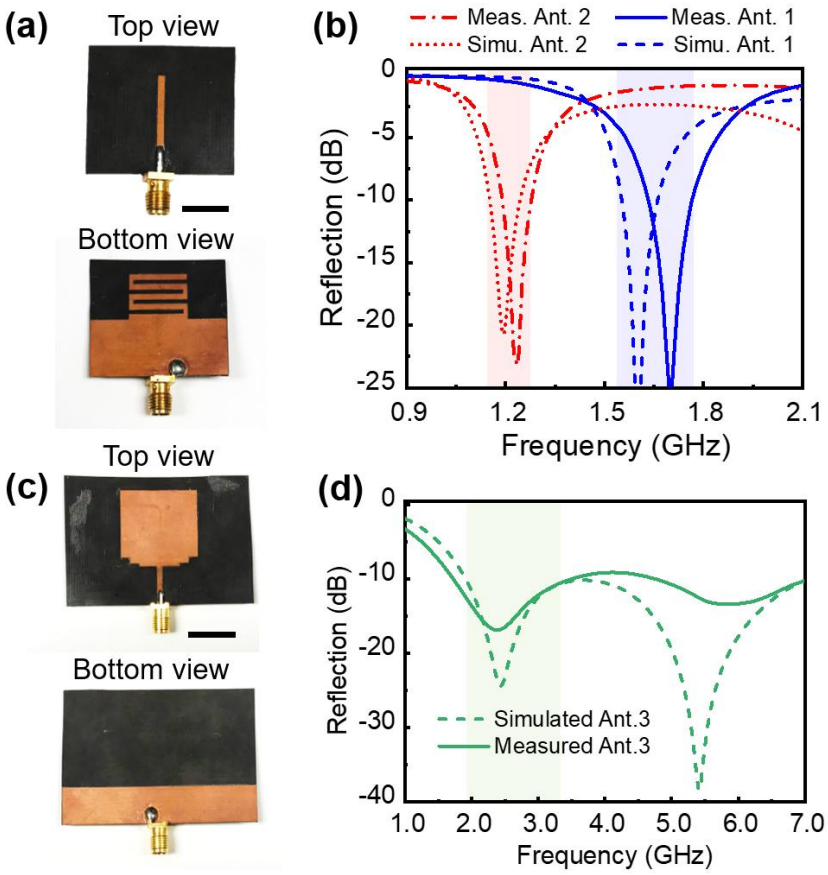


Figure 49. (a) Photographs and (b) measured reflection coefficients for the metamaterial-inspired ESAs (Ant. 1 and Ant. 2). (c) and (d) are similar to (a) and (b), but for the wideband rectangular monopole antenna with geometry perturbations.

for the capacitive nature of the short monopole, so as to form a resonant system directly matched to 50 Ω input impedance, without the need of any matching components. The generated second harmonics will be re-transmitted by a wideband rectangular monopole antenna with geometry perturbations (Ant. 3 with a 50 Ω input impedance in Fig. 47) to the reader. The two metal layers of the harmonic transponder are separated by a Roger 5880 substrate with relative permittivity $\varepsilon_r$ = 2.2, loss tangent δ = 0.0009,

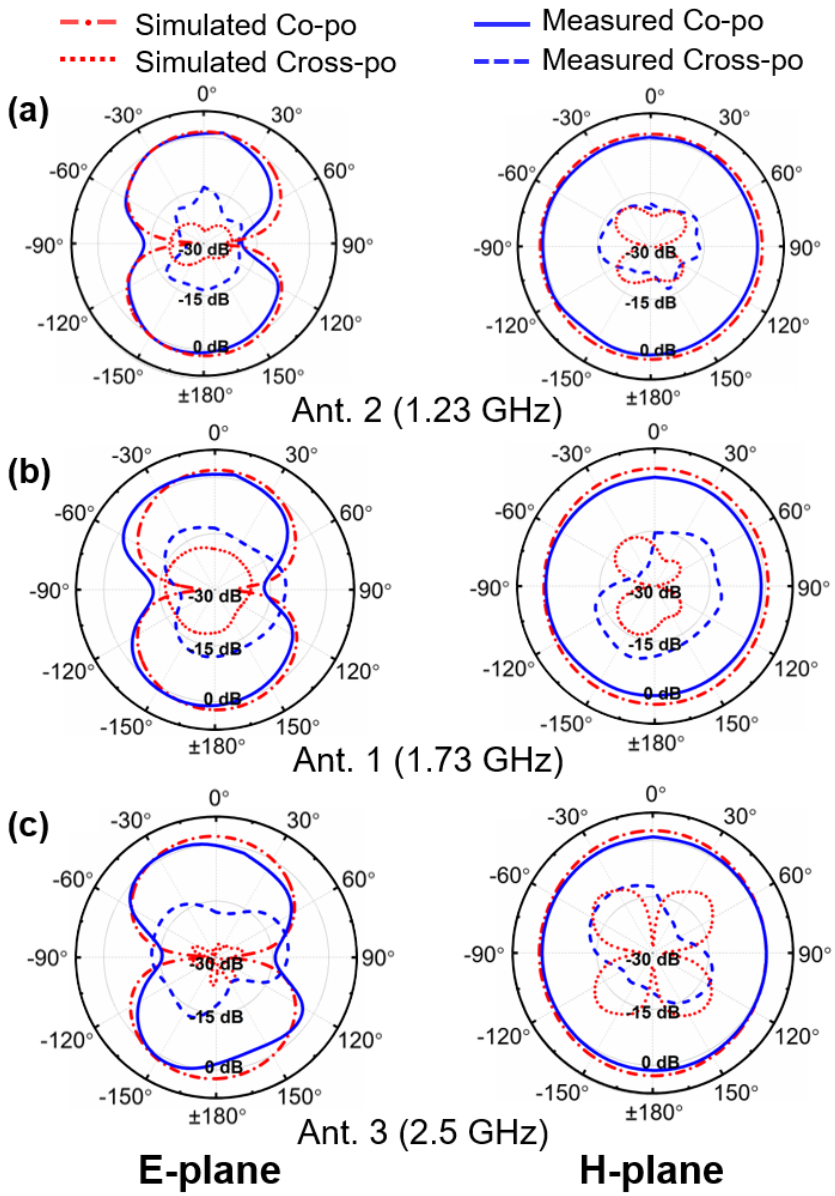


Figure 50. Radiation patterns for (a) Ant. 2 at 1.23 GHz, (b) Ant. 1 at 1.73 GHz, and (c) Ant. 3 at 2.5 GHz.

and thickness $d$ =0.508 mm. Here, commercial software, ANASYS High Frequency Structure Simulator (HFSS), was used for optimization of the proposed antennas [50]. The Advanced Design Simulator (ADS) was used for the design of the frequency doubler and the power divider [51]. Fig.

49 reports photographs and measured reflection spectra for these antennas, which show that the two narrowband ESAs operate at 1.23 GHz and 1.73 GHz, with a bandwidth of 130 MHz and 160 MHz, respectively. The rectangular monopole antenna displays a wideband resonance (2 GHz - 6 GHz) due to the introduced geometry perturbation, covering the entire second-harmonic spectrum of the two ESAs, as illustrated in Fig. 49(d). The measurement and simulation results are in accordance with each other, with the percentage frequency up-shift around 6.5% for Ant. 1 and near 4 % for Ant. 2, ascribed to the potential fabrication errors and small variations in the permittivity of the substrate.

Fig. 50 presents the radiation patterns on *E* (*x*-*z*) and *H* (*y*-*z*) planes for the three antennas in Fig. 49 at their operating frequency (i.e., 1.23 GHz, 1.73 GHz, and 2.5 GHz). Both results exhibit that the three antennas all show the omnidirectional radiation properties with linear polarizations. The measured maximum gains for Ant. 1, Ant. 2, and Ant. 3 are respectively 2 dBi, 1.8 dBi, and 2.1 dBi. The measurement results agree well the simulated ones, as shown in Fig. 50. It should be noted that for all three antennas, the cross-polarization are <-15 dB on the E and H planes, compared to their co-polarization.

These three antennas are combined with a passive frequency doubler [Fig. 51] and a power divider [Fig. 52] for generating a passive harmonic transponder. The schematic diagram and photographs of the passive frequency doubler are presented in Figs. 51(a) and 51(b), of which a shunt quarter-wavelength ($\lambda_0/4$) short-circuited and an open-circuited stubs are placed around a Schottky diode (HSMS 2850). In principle, at $f_0$ ($2f_0$), the $\lambda_0/4$ short-circuited stub is an open (short) end at its input, while the open-circuited stub behaves like an a short (open) end. As a result, the injected RF signal at $f_0$ passes through the input matching network and reaches the diode, whereas the quarter-wavelength open-circuited stub (at $f_0$) at the output shorts the fundamental signals.

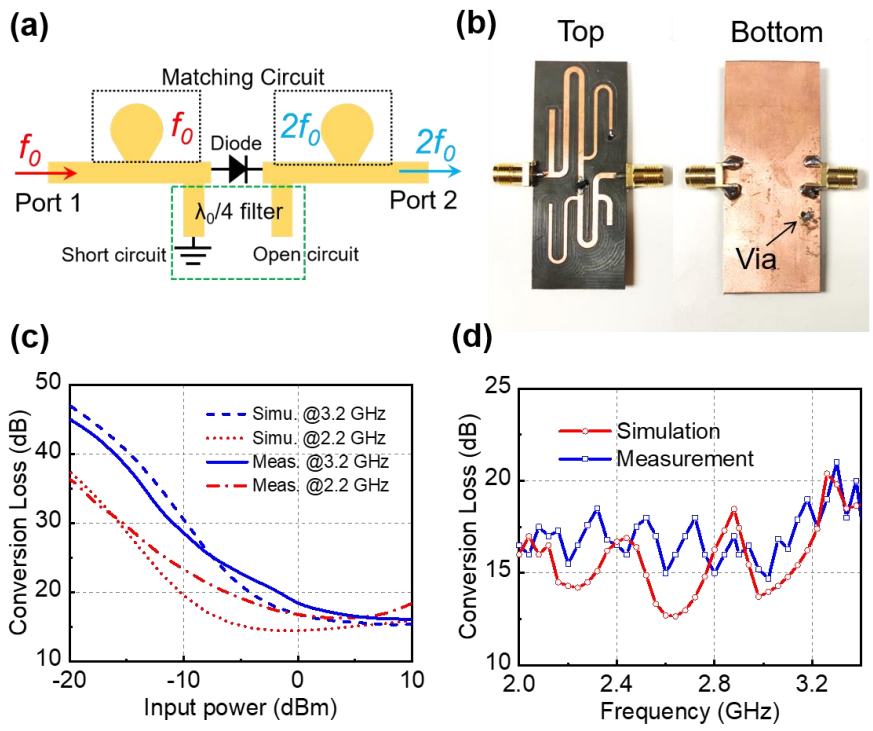


Figure 51. (a) Schematic and (b) implementation of a frequency multiplier, and its measured conversion loss in (c) as a function of different input power level, and in (d) at different output frequency.

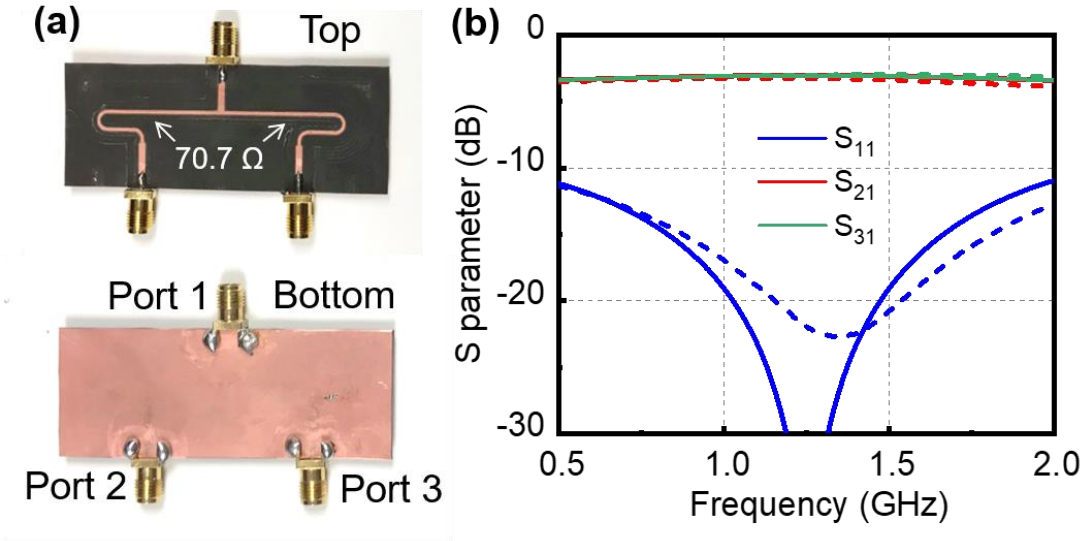


Figure 52. (a) Top and bottom view of the power divider, and (b) its simulated and measured return loss ($S_{11}$) and insertion loss ($S_{21}$ and $S_{31}$)

Fig. 51(c) reports the measured results for the conversion loss of the passive frequency doubler in Fig. 51(b) at different input power. It is seen that at 0 dBm input power, the minimum conversion loss is around 15 dB at 2.2 GHz and is near 17 dB at 3.2 GHz. Fig. 51(d) presents the frequency dependency of the diode-based frequency multiplier at 0 dBm input power, exhibiting that within the frequency band of interest ranging from 2.0 GHz to 3.4 GHz, the frequency doubling efficiency is fairly constant, with only <5 dB fluctuation. It should be noted that the bandwidth and conversion loss flatness of the frequency doubler could be further improved by replacing tuning stubs with lumped-element matching networks and filters. In addition, this work focuses mainly on demonstrating a proof-of-concept prototype and the FHSS sensing scheme. Nevertheless, by scaling the device and circuit properly, the concept could be applied to any frequency band of interest. Fig. 52(a) depicets the photographs of the fabricated power divider, where two quarter-wavelength transformers with a characteristic impedance $\sqrt{2}Z_0 = 70.7\Omega$ are in parallel to each other, for equally separating or combining the RF powers. The simulated and measured S-parameters of the power divider are shown in Fig. 52(b), presenting that the reflection coefficient ($S_{11}$) is always lower than −20 dB over the frequency band of interest from 1 GHz to 1.5 GHz, and the transmission coefficients ($S_{21}$ and $S_{31}$) are still ~ –3 dB within the same frequency range, with a good amplitude consistency ($|S_{21} – S_{31}| < 0.3$ dB).

### 6.3 Microfluidics-Integrated Multiplexing Harmonic Sensor

By loading fluidic channels on top of the resonant ESAs in the harmonic transponder, a battery-free low-profile harmonic sensor could be built, as schematically illustrated in Figs. 53. Here, we adopted the bistatic measurement setup in a noisy environment filled with clutters, echoes, and interferences, as depicted in Fig. 53(a). To avoid the cross-talk between the interrogator and also the sniffer, the interrogator $T_x$ was connected with a low-pass filter (DC - 1.7 GHz) [52] and the

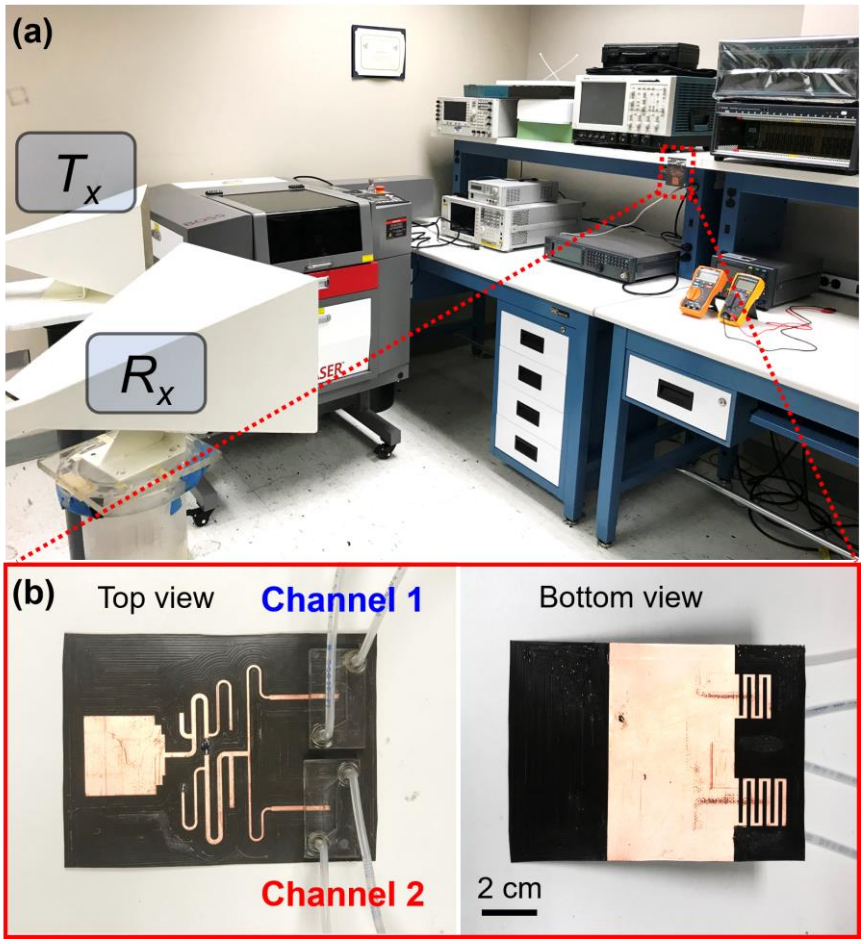


Figure 53. (a) Bistatic measurement configuration in a noisy indoor environment. (b) Top and bottom views of the proposed multiplexed harmonic sensor.

sniffer $R_x$ was connected with a band-pass filter (1.9 - 4.7 GHz) [53]. Fig. 53(b) presents the photographs of this multiplexed harmonic sensor, where two plastic tubes are connected to the isolated fluidic channels for guiding SUTs in and out. We also prepared a binary mixture made of

acetone and water with different volume ratios: A/W = 100 %, 66 %, 33 %, and 0 % (which leads to an (real-

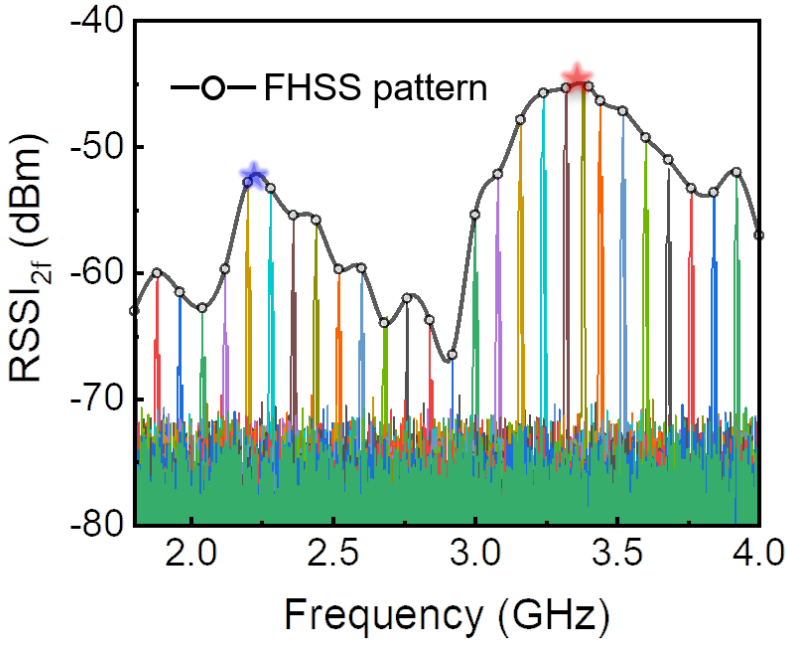


Figure 54. The measured second-harmonic RSSI array of the multiplexed harmonic sensor. Here, the envelope of this RSSI array defines the FHSS pattern.

part) effective relative permittivity $\varepsilon_r$ = 20.7, 32, 58, and 80 [54]). In our measurements [Fig. 54(a)], the interrogator will transmit a frequency-hopped RF signal to the harmonic sensor. The transmitter in the interrogator hops the carrier frequency every 2 seconds and totally 30 frequency channels are swept, with a resolution of 8 MHz. In practice, the frequency hopping rate could be several hundreds of hops per second. Synchronization between the interrogator and the sniffer can be controlled by the Labview program. Afterward, the nonlinear sensor doubles the frequency of

the RF signal and resends the second harmonic to the $R_x$ antenna or sniffer. The backscattered second-harmonic

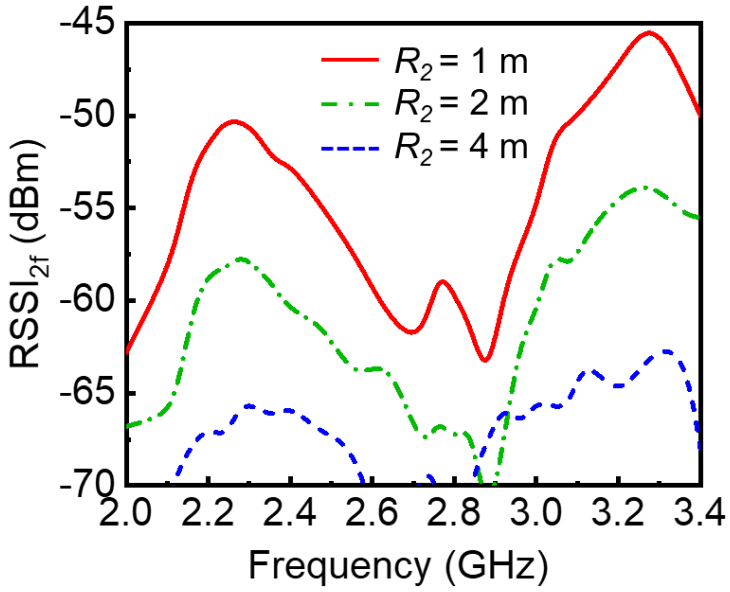


Figure 55. Measured FHSS pattern of the multiplexed harmonic sensor at different interrogating distances.

RSSIs measured by the sniffer form a unique FHSS pattern [see Fig. 54], whose peak frequency could be interrelated with the effective relative permittivity of the injected SUTs. The second-harmonic RSSI could be estimated by the Friis equation, given by [55]

$$\frac{P_r}{P_t} = \left(\frac{\lambda_0}{4\pi R_1}\right)^2 \times \left(\frac{\lambda_0 / 2}{4\pi R_2}\right)^2 \times \frac{G_r G_t G_R G_T}{L_{sys}} \qquad (15)$$

where $G_r$ is the realized gain of the ESAs at $f_0$, $G_t$ is the realized gain of the broadband rectangular monopole antenna at $2f_0$, $G_T$ ($G_R$) denote the realized gain of $T_x$ ($R_x$), $R_1$ ($R_2$) is the distance between $T_x$ ($R_x$) and the sensor, $L_{sys}$ is the system loss that includes the conversion loss of the frequency doubler [Fig. 51(c)], and dielectric losses in passive circuits and SUTs. Here, important

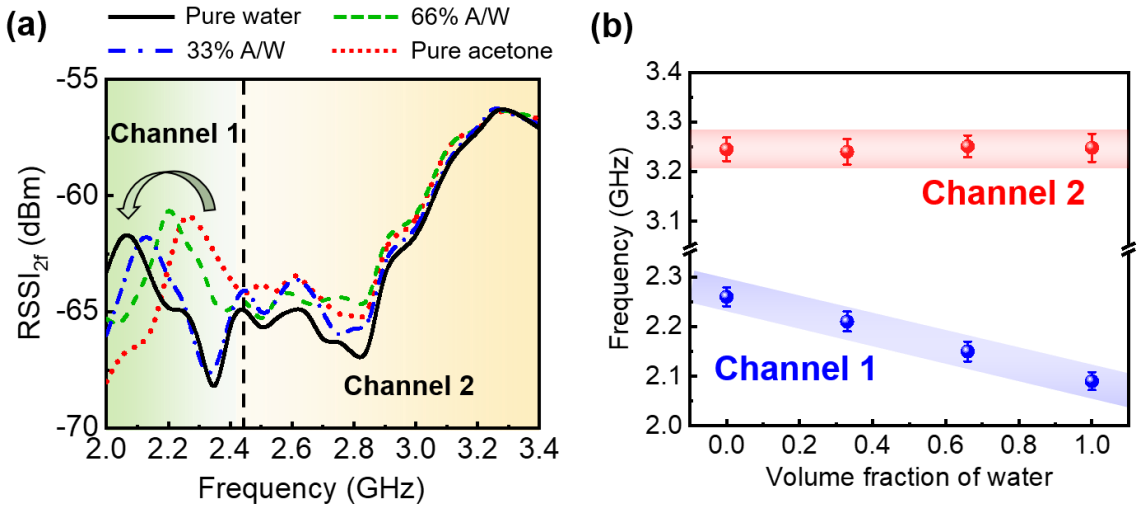


Figure 56. (a) FHSS pattern for the multiplexed harmonic sensor in sensing scenario A, where the Channel 1 is injected with SUT while Channel 2 is kept empty. (b) Peak frequency extracted from FHSS pattern at different volume fraction of water in the mixture.

parameters for our measurement setup are concluded as: $P_t$ = 25 dBm, $R_1$ = $R_2$ = 1 m, $G_T$ = 10.5 dBi at 1.4 GHz, and $G_R$ = 16.5 dBi at 2.8 GHz. Under a fixed transmitted power $P_t$, the received power $P_r$ will be sensitively responsible for the changes in $G_r$ that can be caused by variations in dielectric properties of the liquid solution injected in the fluid channels. Based on the cavity perturbation theory [56], [57], the resonance frequency shift in response to dielectric perturbations is proportional to the electrical field strength of the perturbed mode. As the fluidic channel is

placed on top of the microstrip feedline of the ESA where electric fields are strongly localized, any small fluctuation in the dielectric constant of SUTs could greatly detune the resonant frequency of the ESA [54], which, in turn, lead to a visible downshift in the recorded FHSS pattern.

Fig. 55 shows the measured FHSS patterns at different interrogation distances in the indoor environment shown in Fig. 53; here, except the sensor-to-sniffer distance ($R_2$), all measurement conditions keep the same. It is evident that the peak frequency in the FHSS pattern remains unchanged, regardless of the interrogation range. Consequently, the FHSS pattern analysis could provide an absolute accuracy sensing with high robustness and reliability. This is, on the other hand, impossible for a typical passive harmonic tag that detects the RSSI amplitude at a constant operating frequency. In addition, the redundant information from extra dimensions could tolerate variation of other factors, for example, the sensor location and interferences from near-field objects. The maximum detection range is ~ 4.0 m for a given noise floor of –70 dBm. The maximum range is expected to be increased by adjusting configurations of the spectrum analyzer with reduced noise floor and/or by optimizing antennas and circuits used in the harmonic tag.

Next, in order to demonstrate the multiplexed sensing capability of the proposed wireless sensor, we have also conducted sensing experiments for three different scenarios, which are: (A) Channel 1 is injected with the SUT and Channel 2 is empty; (B) Channel 1 is empty and Channel 2 is injected with the SUT; (C) both fluidic channels are injected with SUTs. Here, important parameters used in this measurement setup are: $P_t$ = 25 dBm, $R_1 = R_2$ = 1.3 m, $G_T$ = 10.5 dBi at 1.4 GHz, $G_R$ = 16.5 dBi at 2.8 GHz, and the liquid volume of SUT is set as 100 μL (i.e., the total volume of the fluidic channel). Fig. 56 presents the measurement results for the sensing scenario A. We find that from Fig. 56(a) that by injecting acetone/water mixtures of different concentrations into the Channel 1, the first RSSI peak in the FHSS pattern could be shifted from 2.28 to 2.07 GHz,

while the second RSSI peak is locked at 3.25 GHz, as concluded in Fig. 56(b). On the other hand, for the scenario B, the first RSSI peak keeps unchanged, while the second RSSI peak is downshifted from 3.11 to 2.6 GHz, as illustrated in Figs. 57(a) and 57(b). The measured results in Figs. 56

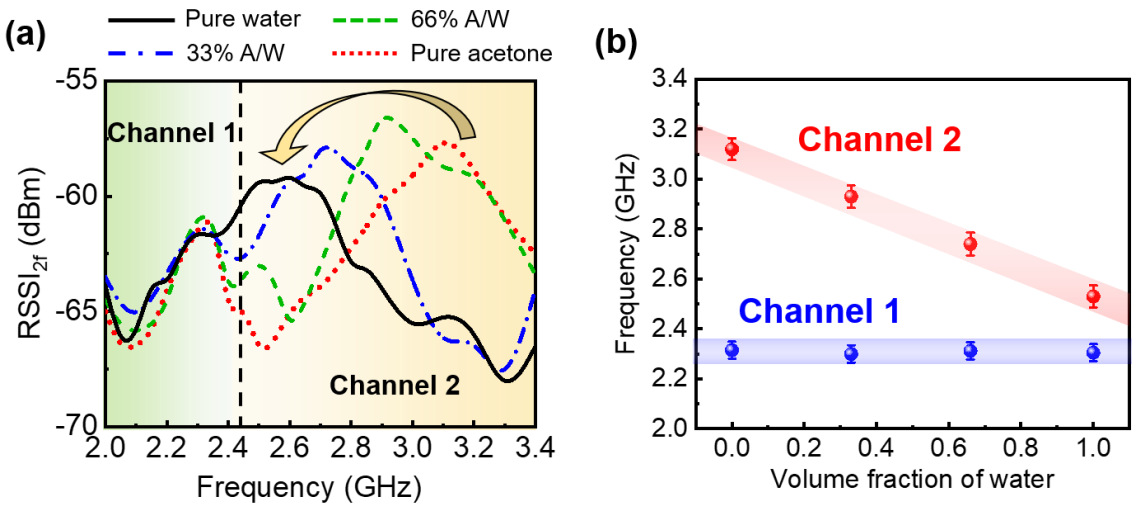


Figure 57. (a) and (b) are similar to Figs. 56(a) and 9(b), but for the sensing scenario B in which Channel 2 is injected with the binary mixture while Channel 1 is kept void.

and 57 obviously indicate that multiplexed sensing with good isolation could be possible with the proposed compact harmonic sensor. Fig. 58 presents the measurement results for the sensing scenario C, where the harmonic sensor is exploited to simultaneously monitor two types of SUTs. It is evidently seen from Fig. 58 that when acetone/water mixture of different concentration are injected into the two fluidic channels, the first RSSI peak is shifted from 2.27 to 2.09 GHz. Besides, the second one is also shifted from 3.12 to 2.61 GHz. Such results further confirm robustness and

multiplexed sensing ability of the proposed harmonic sensor in noisy environments. For different injected SUTs, the peak RSSI strength may slightly change because dielectric constants and loss tangents of them can be different. The loss tangent fitted from the measurement result is 0.025 for pure acetone and 0.04 (0.055) for the mixture with A/W = 66% (33%), and is increased to 0.075 for pure water. Increasing the SUT's dielectric loss may decrease the Q-factor of the ESA, which in turn reduces the peak RSSI value and increases the linewidth of the FHSS pattern, as can be seen in Figs. 56-58.

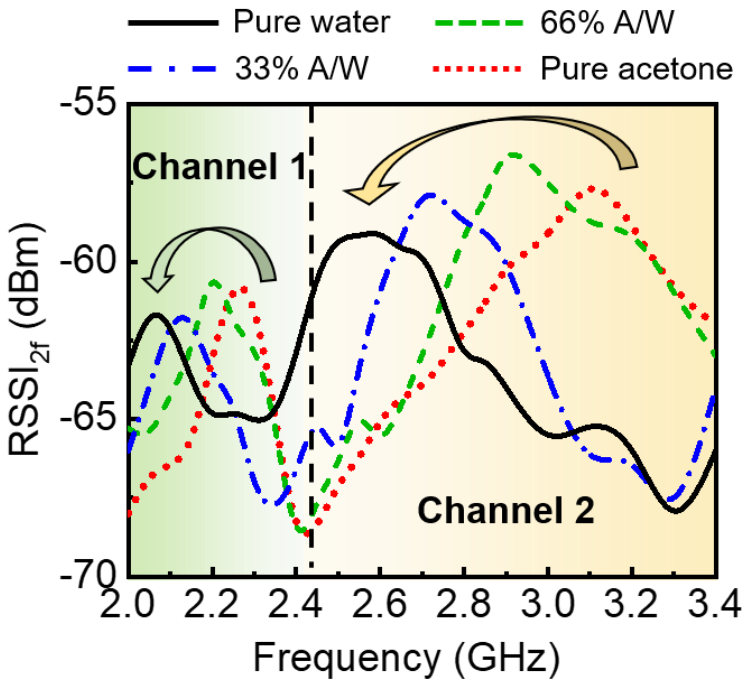


Figure 58. Similar to Fig. 57, but for the sensing scenario C, in which both fluidic channels are injected with binary mixtures.

Finally, we notice that this harmonic sensor was manufactured using a single-layer Roger 5880 substrate with thickness of only 0.5 mm, and therefore, allowing good flexibility. We have

deployed the flexible harmonic tag on an empty dielectric tube (Polyvinyl Chloride (PVC) pipe with a radius of $r$ = 10 cm and a relative permittivity $\varepsilon_r$ = 2.3 at 2.6 GHz), as depicted in Figs. 59(a) and 59(b). In this measurement, the tag has an ±30° bending angle, and the injected liquid volume is kept as 100 µL. The same bistatic telemetry setup was used to measure FHSS patterns of the harmonic tag attached conformally to the PVC tubes. Fig. 59(c) presents the normalized peak frequency extracted from the FHSS patterns for water-acetone mixtures with different water volume fractions; here, three different bending angles were tested. From Fig. 59(c), we find that bending the harmonic tag will not affect the sensing performance, which once again proves the robustness of our prototype in withstanding a moderate range of bends. The sensitivity and resolvability of the proposed device can be defined as the slope of the peak RSSI frequency versus the water volume fraction [see Fig. 59(c)], which are obtained as 2.1 MHz/1 % for Channel 1 and 5.1 MHz/1 % for Channel 2. Such results suggest that for a 100 µL microfluidic reservoir, ±1 % change in the volume fraction of water may be detected by using a standard spectrum analyzer with a 10 kHz resolution bandwidth.

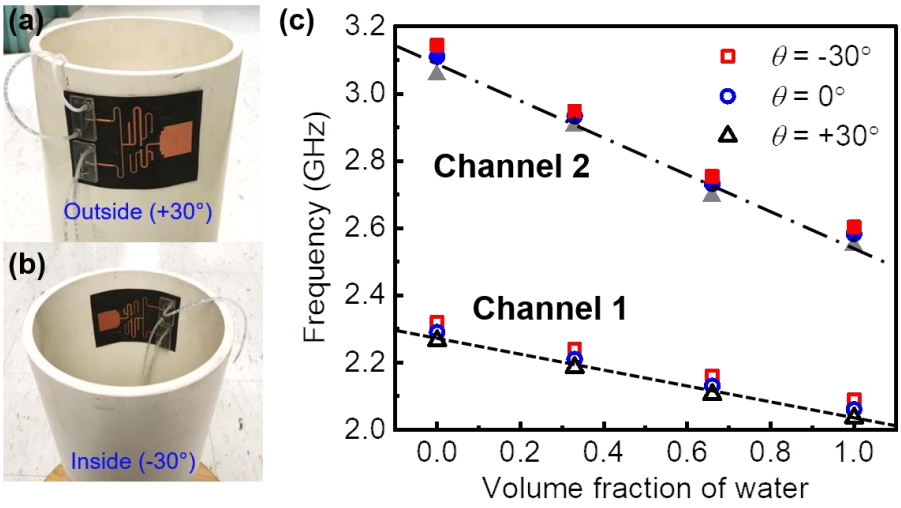

Figure 59. Conformal multiplexed harmonic sensor on a dielectric tube at a bending angle around (a) +30° and (b) -30°. (c) Peak frequency of the FHSS patterns against different binary mixtures for sensing scenario C.

As an example, the flexible harmonic tag can be deployed on PVC pipes in the plumbing system [see Fig. 59(a)], for which plastic tubes can guide SUTs from different nodes into specific channels. Also, a plastic tube carrying environmental mixtures (e.g., water mixed with microplastics, microfibers, detergents, hydrogen peroxides, etc.) could be connected to microfluidic separation and sorting cells for delivering a specific SUT to its assigned channel. In general, the ratio of dielectric constant between these agents and pure water are greater than that between acetone and water. Ideally, an array of narrow-band ESA and liquid channels can be realized for multiplexed sensing purposes.

### 6.4 Conclusion

To meet the requirement for wireless dual-channel sensing, in this chapter, I have demonstrated a compact harmonic tag with a scalable and multiplexed monitoring capability. By hybridizing this harmonic tag with multiple fluidic channels, I have built a battery-free multiplexed harmonic sensor and demonstrated its capability for contactlessly monitoring properties of solutions in an indoor environment. I envision that such multiplexed harmonic tags can also be integrated with the system-level fluidic networks, e.g., sorting cells or diagnostic assays, to maximize its potential in telemetering, wireless sensing, lab-on-a-chip, and rapid healthcare tests applications.

## REFERENCES


[1] S. Amendola, R. Lodato, S. Manzari, C. Occhiuzzi, and G. Marrocco , "RFID technology for IoT-based personal healthcare in smart spaces," *IEEE Internet Things J.*, vol. 1, no. 2, pp. 144-152, 2014.

[2] G. Bedi, G. K. Venayagamoorthy, R. Singh, R. R. Brooks, K. K. Wang, "Review of Internet of Things (IoT) in electric power and energy systems," *IEEE Internet Things J.*, vol. 5, no. 2, pp. 847-870, 2018.

[3] K. G. Ong and C. A. Grimes, "A resonant printed-circuit sensor for remote query monitoring of environmental parameters," *Smart Mater. Struct.*, vol. 9, no. 4, p. 421–428, 2000.

[4] K. G. Ong, K. F. Zeng, and C. A. Grimes, "A wireless, passive carbon nanotube-based gas sensor," *IEEE Sensors J.*, vol. 2, no. 2, pp. 82-88, 2002.

[5] J. Coosemans, M. Catrysse, and R. Puers, "A readout circuit for an intraocular pressure sensor," *Sens. Actuators A, Phys.*, vol. 110, no. 1-3, p. 432–438, 2004.

[6] Y. Feng, L. Xie, Q. Chen, and L. R. Zheng, "Low-cost printed chipless RFID humidity sensor tag for intelligent packaging," *IEEE Sensors J.*, vol. 15, no. 6, pp. 3201 - 3208, 2014.

[7] J. Tan, M. Sathyamurthy, A. Rolapp, J. Gamez, E. Hennig, E. Schäfer, and R. Sommer, "A fully passive RFID temperature sensor SoC with an accuracy of ±0.4 ◦C (3σ) from 0 ◦C to 125 ◦C," *IEEE J. Radio Freq. Identif.*, vol. 3, no. 1, p. 35–45, 2019.

[8] D. Dondi, A. Bertacchini, D. Brunelli, L. Larcher and L. Benini, "Modeling and optimization of a solar energy harvester system for self-powered wireless sensor networks," *IEEE Trans. Ind. Electron.*, vol. 55, no. 7, p. 2759–2766, 2008.

[9] P. Y. Chen, M. Sakhdari, M. Hajizadegan, Q. Cui, M. Cheng, R. El-Ganainy, and A. A. Alù, "Generalized parity-time symmetry condition for enhanced sensor telemetry," *Nat. Electron.*, vol. 1, p. 297, 2018.

[10] P. J. Chen, S. Saati, R. Varma, M. S. Humayun, and Y. C. Tai, "Wireless intraocular pressure sensing using microfabricated minimally invasive flexible-coiled LC sensor implant," *J. Microelectromechan. Syst.,* vol. 19, no. 4, pp. 721-734, 2010.

[11] L. Y. Chen et al., "Continuous wireless pressure monitoring and mapping with ultra-small passive sensors for health monitoring and critical care," *Nat. Commun.,* vol. 5, p. 5028, 2014.

[12] M. Sakhdari, M. Hajizadegan, Q. Zhong, D. N. Christodoulides, R. El-Ganainy, and P. Y. Chen, "Experimental Observation of PT Symmetry Breaking near Divergent Exceptional Points," *Phys. Rev. Lett*. 123, 193901 (2019).

[13] P. Y. Chen and R. El-Ganainy, "Exceptional points enhance wireless readout," *Nat. Electron.,* 2, 323 (2019).

[14] Q. A. Huang, L. Dong and L. F. Wang, "LC passive wireless sensors toward a wireless sensing platform: status, prospects, and challenges," *J. Microelectromechan. Syst.,* vol. 25, p. 822–841, 2016.

[15] K. G. Ong and C. A. Grimes, "A resonant printed-circuit sensor for remote query monitoring of environmental parameters," *Smart Mater. Struct.,* vol. 9, no. 4, p. 421–428, 2000.

[16] T. J. Harpster, B. Stark, and K. Najafi, "A passive wireless integrated humidity sensor," *Sens. Actuators A, Phys.,* vol. 95, pp. 100-107, 2002.

[17] L. Yang, A. Rida, R. Vyas, M. M. Tentzeris, "RFID tag and RF stuctures on a paper substrate using inkjet-printing technology," *IEEE Trans. Microw. Theory Techn.,* vol. 55, no. 12, pp. 2894-2901, 2007.

[18] L. Yang, R. Zhang, D. Staiculescu, C. P. Wong, M. M. Tentzeris, "A novel conformal RFID-enabled module utilizing inkjet-printed antennas and carbon nanotubes for gas-detection applications," *IEEE Antennas Wireless Propag. Lett.* , vol. 8, pp. 653-656, 2009.

[19] B. S. Cook, J. R. Cooper, M. M. Tentzeris, "An inkjet-printed microfluidic RFID-enabled platform for wireless lab-on-chip applications," *IEEE Trans. Microw. Theory Techn.*, vol. 61, no. 12, pp. 4714-4723, 2013.

[20] B. G. Colpitts, G. Boiteau, "Harmonic radar transceiver design: miniature tags for insect tracking," *IEEE Trans. Antennas Propag.*, vol. 52, no. 11, pp. 2825-2832, 2004.

[21] D. Mascanzoni and H. Wallin, "The harmonic radar: A new method of tracing insects in the fields," *Ecol. Entomol.*, vol. 11, pp. 387-390, 1986.

[22] J. R. Riley, A. D. Smith, D. R. Reynolds, and A. S. Edwards, "Tracking bees with harmonic radar," *Nature*, vol. 379, pp. 29-30, 1996.

[23] X. Hui, Y. Ma, and E. C. Kan, "Code division multiple access in centimeter accuracy harmonic RFID locating system," *IEEE J. Radio Freq. Identif.*, vol. 1, no. 1, pp. 51–58, Mar. 2017.

[24] L. Zhu, N. Alkhaldi, H. M. Kadry, S. L. Liao, and P. Y. Chen, "A compact hybrid-fed microstrip antenna for harmonics-based radar and sensor system," *IEEE Antennas Wireless Propag. Lett.*, vol. 17, no. 12, pp. 2444-2448, 2018.

[25] X. Gu, S. N. N, L. Guo, S. Hemour, and K. Wu, "Diplexer-based fully passive harmonic transponder for sub-6-GHz 5G-compatible IoT applications," *IEEE Trans. Microw. Theory Techn.*, vol. 67, no. 5, pp. 1675-1687, 2019.

[26] B. Kubina, J. Romeu, C. Mandel, M. Schussle, and R. Jakoby, "Quasi-chipless wireless temperature sensor based on harmonic radar," *Electron. Lett.*, vol. 50, no. 2, pp. 86–88, Jan. 2014.

[27] D. Ahbe, S. Beer, T. Zwick, Y. Wang, and M. M. Tentzeris, "Dual-band antennas for frequency-doubler-based wireless strain sensing," *IEEE Antennas Wireless Propag. Lett.*, vol. 11, pp. 216-219, 2012.

[28] C. Cho, X. H. Yi, D. Li, Y. Wang, and M. M. Tentzeris, "Passive wireless Frequency doubling antenna sensor for strain and crack sensing," *IEEE Sensors J.*, vol. 16, no. 14, pp. 5725-5733, 2016.

[29] A. Lazaro, R. Villarino, and D. Girbau, “A passive harmonic tag for humidity sensing,” *Int. J. Antennas Propag.*, vol. 2014, 2014, Art. no. 670345.

[30] A. Abdelnour, A. Lazaro, R. Villarino, D. Kaddour, S. Tedjini and D. Girbau, “Passive harmonic RFID system for buried assets localization,” *Sensors*, vol. 18, no. 11, 2018, Art. no. 3635.

[31] M. I. M. Ghazali, S. Karuppuswami, and P. Chahal, “Embedded passive RF tags towards intrinsically locatable buried plastic materials,” in *Proc. IEEE 66th Electron. Compon. Technol. Conf. (ECTC)*, 2016, pp. 2575–2580.

[32] S. Mondal et al., “Monitoring and localization of buried plastic natural gas pipes using passive RF tags,” *AIP Conf. Proc.*, vol. 1949, 2018, Art. no. 020020.

[33] M. Hajizadegan, M. Sakhdari, L. Zhu, Q. S. Cui, H. Y. Huang, M. C. Cheng, et al, “Graphene sensing modulator: Toward low-noise, self-powered wireless microsensors,” *IEEE Sensors J.*, vol. 17, no. 22, pp. 7239-7247, 2017.

[34] X. Hui and E. C. Kan, “Monitoring vital signs over multiplexed radio by near-field coherent sensing,” *Nat. Electron.*, vol. 1, no. 1, pp. 74–78, 2018,

[35] H. Y. Huang, L. Tao, F. Liu, L. Ji, Y. Hu, M. C. Cheng, et al, “Chemical sensitive graphene modulator with a memory effect for internet-of-things applications,” *Microsyst. Nanoeng.*, vol. 2, p. 16018, 2016.

[36] H. Huang, M. Sakhdari, M. Hajizadegan, A. Shahini, D. Akinwande, and P. Y. Chen, “Toward transparent and self-activated graphene harmonic transponder sensors,” *Appl. Phys. Lett.*, vol. 108, no. 17, p. 173503, 2016.

[37] Y. Y. Zheng, Y. T. Ma, J. Y. Zhang and X. Xie, “COVID-19 and the cardiovascular system,” *Nat. Rev. Cardiol.*, 2020.

[38] H. Huang, P. Y. Chen, C. H. Hung, R. Gharpurey, and D. Akinwande, “A zero power harmonic transponder sensor for ubiquitous wireless μL liquid-volume monitoring,” *Sci. Rep.*, vol. 6, p. 18795, 2016.

[39] H. Huang, P. Y. Chen, C. H. Hung, R. Gharpurey, and D. Akinwande, "Frequency hopped wireless passive sensing system with harmonic transponder antenna sensor," in *IEEE MTT-S Int. Microw. Symp. Dig.*, May 2015, pp. 1–4.

[40] V. Palazzi, F. Alimenti, P. Mezzanotte, G. Orecchini, and L. Roselli, "Zero-power, long-range, ultra low-cost harmonic wireless sensors for massively distributed monitoring of cracked walls," in *IEEE MTT-S Int. Microw. Symp. Dig.*, Honolulu, HI, USA, Jun. 2017, pp. 1335–1338.

[41] L. Zhu, and P. Y. Chen, "A compact, zero-power and low-noise harmonic-transponder for liquid and moisture sensing," in 2019 *IEEE International Symposium on Antennas and Propagation and USNC-URSI Radio Science Meeting*, Atlanta, GA, USA, USA, 2019.

[42] L. Zhu, M. Farhat, Y. C. Chen, K. N. Salama and P. Y. Chen, "A compact, passive frequency-hopping harmonic sensor based on a microfluidic reconfigurable dual-band antenna," *IEEE Sensors J.*, 2020. doi: 10.1109/JSEN.2020.3000778.

[43] A. Erentok, and R. W. Ziolkowski, "Metamaterial-inspired efficient electrically small antennas," *IEEE Trans. Antennas Propag.*, vol. 56, no. 3, pp. 691 - 707, 2008.

[44] R. W. Ziolkowski, and A. Erentok, "Metamaterial-based efficient electrically small antennas," *IEEE Trans. Antennas Propag.* , vol. 54, no. 7, pp. 2113 - 2130, 2006.

[45] R. W. Ziolkowski, P. Jin and C.-C. Lin, "Metamaterial Inspired Engineering of Antennas," *Proc. IEEE*, vol. 99, no. 10, pp. 1720 - 1731, 2010.

[46] R. Fleury, J. C. Soric, and A. Alù, "Physical bounds on absorption and scattering for cloaked sensors," *Phys. Rev. B*, vol. 89, p. 045122, 2014.

[47] P. Y. Chen, H. Huang, C. H. Hung, "Compact metamaterial-enclosed wireless sensors with subtle perception of internal physical events," *Appl. Phys. Lett.*, vol. 107, 194101, 2015.

[48] P. Y. Chen and A. Alu, "Dual-mode miniaturized elliptical patch antenna with μ-negative metamaterials," *IEEE Antennas Wireless Propag. Lett.*, vol. 9, pp. 351 - 354, 2010.

[49] P. Y. Chen and A. Alu, "Sub-wavelength elliptical patch antenna loaded with μ-negative metamaterials," *IEEE Trans. Antennas Propag.*, vol. 58, no. 9, pp. 2909-2919, 2010.

[50] *ANSYS 2020 R1 Academic Research Electromagnetics Suite.* Released in 2020. ANSYS, Inc., Southpointe 2600 Ansys Drive Canonsburg, PA, USA.

[51] Keysight PathWave Advanced Design System (ADS) 2020. Released in 2020. Keysight Technologies, 1400 Fountaingrove Parkway Santa Rosa, CA, USA.

[52] *VLF-1525+ from Mini-Circuit.* Accessed: Jan. 10, 2020. [Online]. Availabe: https://www.minicircuits.com/WebStore /dashboard.html?model=VLF-1525%2B.

[53] *VHF-1810+ from Mini-Circuit.* Accessed: Jan. 10, 2020. [Online]. Availabe: www.minicircuits.com /WebStore/dashboard.html?model=VHF-1810%2B

[54] K. Saeed, R. D. Pollard, and I. C. Hunter, "Substrate integrated waveguide cavity resonators for complex permittivity characterization of materials," *IEEE Trans. Microw. Theory Techn.*, vol. 56, no. 10, pp. 2340-2347, 2008.

[55] J. A. Shaw, "Radiometry and the Friis transmission equation," *Am. J. Phys.*, vol. 81, no. 1, pp. 33-37, 2013.

[56] C. Gao, T. Wei, F. Duewer, Y. Lu,and X. D. Xiang, "High spatial resolution quantitative microwave impedance microscopy by a scanning tip microwave near-field microscope," *Appl. Phys. Lett.*, vol. 71, pp. 1872-1874, 1997.

[57] H. Huang, P. S. Zhao, P. Y. Chen, Y. Ren, X. Liu, M. Ferrari, Y. Hu, and D. Akinwande, "RFID tag helix antenna sensors for wireless drug dosage monitoring," *IEEE J. Transl. Eng. Health Med.*, vol. 2, pp. 1–8, 2014.

# VII. A PASSIVE SMART FACE FOR WIRELESS COUGH MONITORING: A HARMONIC DETECTION SCHEME WITH CLUTTER REJECTION

Cough detection has aroused great interest because the assessment of cough frequency may improve diagnosis accuracy for dealing with several diseases, such as chronic obstructive pulmonary disease (COPD) and the recent COVID-19 global pandemic crisis. In this chapter, we propose and experimentally demonstrate a wireless smart face mask based on a passive harmonic tag for real-time cough monitoring and alert. Our results show that the cough events can be successfully monitored through non-contact track of the received signal strength indicator (RSSI) at the harmonic frequency. Owing to the frequency orthogonality between the launched and backscattered radio-frequency (RF) signals, the harmonic tag-based smart mask can well suppress the electromagnetic interferences, such as clutters and crosstalks in noisy environments. We envision that this zero-power and lightweight wireless wearable device may be beneficial for cough monitoring and the public health condition in terms of tracking potential contagious person and virus-transmissive events.

## 7.1 Introduction

Cough, an expiratory maneuver against a closed glottis with characteristic sound, is a common and important symptom in many respiratory diseases, such as pneumonia and tuberculosis [1], [2]. Cough may appear sporadically with illnesses (e.g. colds and flu) to act as a protective and clearing mechanism, but when it becomes chronic, it could severely impair life quality by interfering with breathing, sleep and normal daily activities [3], [4]. As a result, this symptom is the commonest reason for people seeking medical advice, and the assessment of cough frequency is considered as a critical tool in clinical use. More urgently, as the disastrous spreading of COVID-19 in 2020, the

whole world is in demand of some type of affordable, rapid and effective facilities for warning of transmissive events, identifying potential contagious persons, as well as tracking face-mask wearing compliance in public [5]. Cough, which is one of the top symptoms associated with COVID-19, could be of high interest in being monitored, so as to facilitate the above-mentioned demand in the critical pandemic situation.

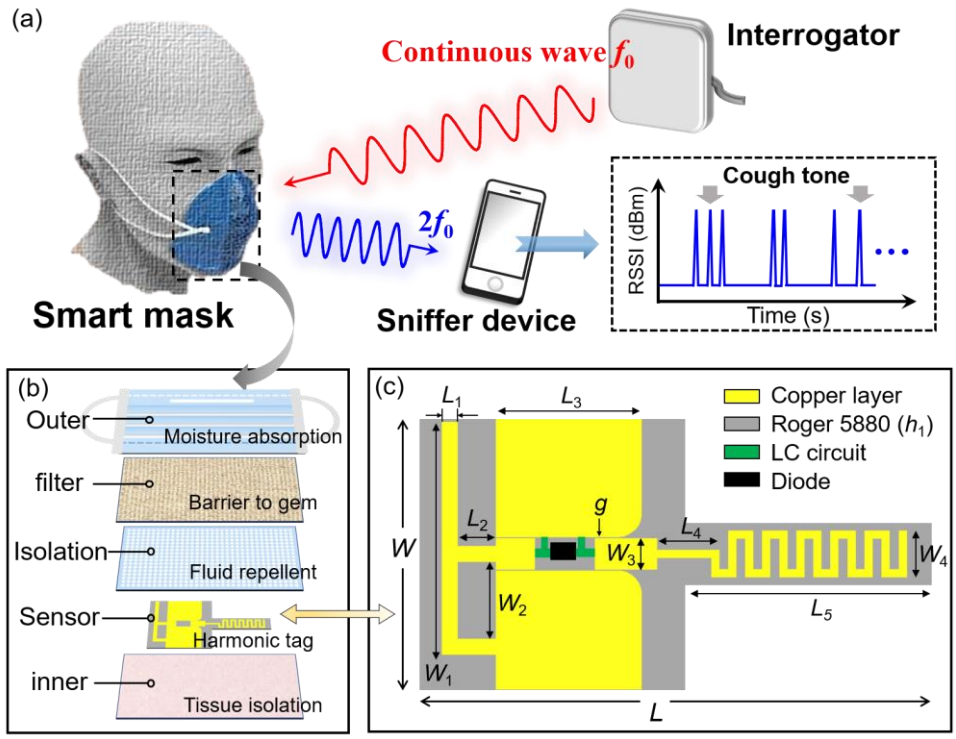


Figure 60. (a) Schematics of a smart face mask based on a passive, lightweight, and low-profile harmonic tag. (b) 3-D view of the geometry of the smart face mask. (c) Schematics and dimensions of the harmonic tag.

Driven by this demand, some attempts to monitor cough have been made, which started around the 1950s with simple audio recording systems that require manual interpretation of cough events [6]. To date, many emerging cough monitoring systems have been developed, which can be

divided into three main categories. The first one reached from the airflow measurement requires placing detection module (e.g., piezoelectric sensor) close to the nose or mouth to obtain the flow dynamics of cough [7], [8]. This method is clearly not suitable for continuous cough monitoring in the outpatient environment [9]. The second type is based on monitoring the movement of the chest or abdominal wall [10]. In this approach, an accelerometer is directly placed at the volunteer's chest wall to record cough events. Although this solution can offer precise measurement results, it typically requires a trained operator to manually identify cough events, which is a rather time-consuming and arduous task [10]. The third one based on the measurement of cough sounds has been more universal because of advances in computer technology and the availability of portable digital sound recording devices [11], [12]. Unfortunately, these automatic cough monitors may suffer from confusion with surrounding noises and other parasitic patient sounds (e.g., throat clearing, humming, or laughing) that are not associated with the disease transmissive event. In addition, cough detection using sound could lose important detailed information, e.g. whether the person is wearing a face mask when coughing.

Very recently, several radio-frequency (RF) approaches, such as antenna sensors and passive radio frequency identification (RFID), have been explored for remotely detecting and monitoring cough events [13], [14]. Despite the improved effectiveness, these backscattering tags are often vulnerable to a low signal-to-clutter/noise ratio in noisy indoor environments, thereby impeding real-time, continuous and acccurate monitoring of coughs. Seeking to overcome the troublesome issues of passive RF sensing, the harmonic transponder sensor (or harmonic sensor) has been recently proposed [15]-[17]. Similar to the harmonic radar invented in 70s [18], a harmonic sensor launches and detects RF signals at orthogonal frequencies (e.g., fundamental frequency and harmonics), with the information of sensor encoded in the frequency-modulated RF

signal, for avoiding multipath interferences, clutters, and crosstalks [19]-[21]. To date, harmonic sensors have been used to remote sensing of mechanical cracks [22], [23], humidity [24], temperature, liquid levels [25], pH [26], and biochemical processes [27], [28], as well as localization of underground buried assets [29], [30]. In this work, we propose a lightweight harmonic sensor that can be flawlessly embedded in the face mask to perform rapid, real-time wireless cough monitoring. The harmonic sensor system is sketched in Fig. 60(a). The reader transmits a continuous-wave (CW) RF signal at frequency $f_0$ to the smart face mask. When the face mask is in close contact with or the proximity of mouth (i.e., air gap $g \sim 0$), the dielectric loading effect due to human tissues will shift resonant frequencies of antennas and, therefore, no detectable harmonic signal can be generated. In other words, the smart face mask is in the OFF state with zero second-harmonic RSSI. On the other hand, when cough happens, the effect of human body disappears (i.e., $g > 10$ mm) and, thus, the RF monotone can be received by the antenna on the face mask, undergoing the frequency multiplication process ($f_0 \rightarrow 2f_0$), and being re-transmitted to the reader or sniffer. As a result, the harmonic tag can be waked up (i.e., ON state) due to coughs, whose frequency and pattern can be retrieved from the time series of the RSSI at the second-harmonic frequency [Fig. 60(a)]. More interestingly, if the proposed smart face mask becomes a universal standard, combining with sound-based cough monitoring, it can serve as a face mask compliance tracker. For example, if the sound monitoring detects a cough event without a matched RF harmonic, it means that the person who coughs is not wearing a face mask, and it will be alerted as a high-risk event.

### 7.2 Design and Measurement of A Harmonic Tag

Fig. 60(b) depicts the exploded view of the proposed smart face mask, which consists of a harmonic transponder sandwiched between a typical face mask and a tissue isolation layer. Fig.

60(c) illustrates the top view of the proposed harmonic transponder comprising a meander-line antenna, a frequency multiplier, and an inverted-F antenna, with their optimal design parameters summarized in Table VI. The two microstrip antennas are matched to a 50 Ω coplanar waveguide (CPW), The harmonic transponder was fabricated on the flexible, single-side Roger 5880 substrate with relative permittivity $\varepsilon_r = 2.2$, loss tangent $\delta = 0.0009$, and thickness of only 0.5 mm. The total dimension of the harmonic tag can fit into a small area on the interior of the face mask.

Table VI: Summary of dimensions in the harmonic tag (Unit: mm)

| Par. | $L$ | $L_1$ | $L_2$ | $L_3$ | $L_4$ | $L_5$ |
|---|---|---|---|---|---|---|
| Value | 65 | 2 | 5 | 18.8 | 8 | 31.5 |
| Par. | $W$ | $W_1$ | $W_2$ | $W_3$ | $W_4$ | $g$ |
| Value | 35 | 30 | 10 | 4 | 6 | 0.2 |

Figs. 61(a) and 61(b) report the measured reflection coefficient ($S_{11}$) and photographs for the microstrip meander-line and inverted-F antennas, respectively. We find that in free space, the meander-line antenna resonates at 1.5 GHz (fundamental frequency) with a -10 dB bandwidth of 164 MHz, while the inverted-F antenna operates at the second-harmonic frequency (3.0 GHz) with a -10 dB bandwidth of 555 MHz. The measurement results are in good agreement with the simulation results, with a fractional frequency shift of 1.33 % for the meander-line antenna and 2.28 % for the inverted-F antenna, due primarily to the fabrication errors and variations in the dielectric constant of the substrate.

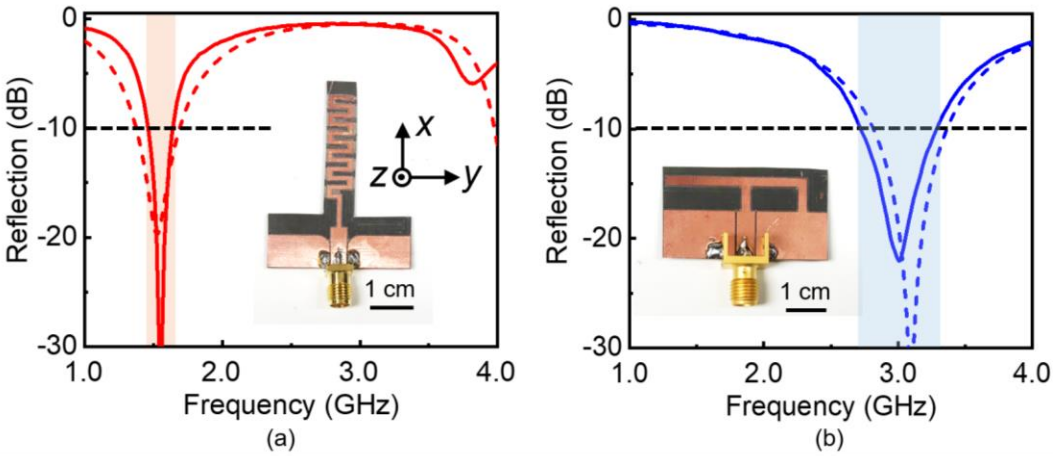


Figure 61. Measured (solid line) and simulated (dashed line) reflection coefficient versus frequency for (a) the meander-line antenna and (b) the printed inverted-F antenna.

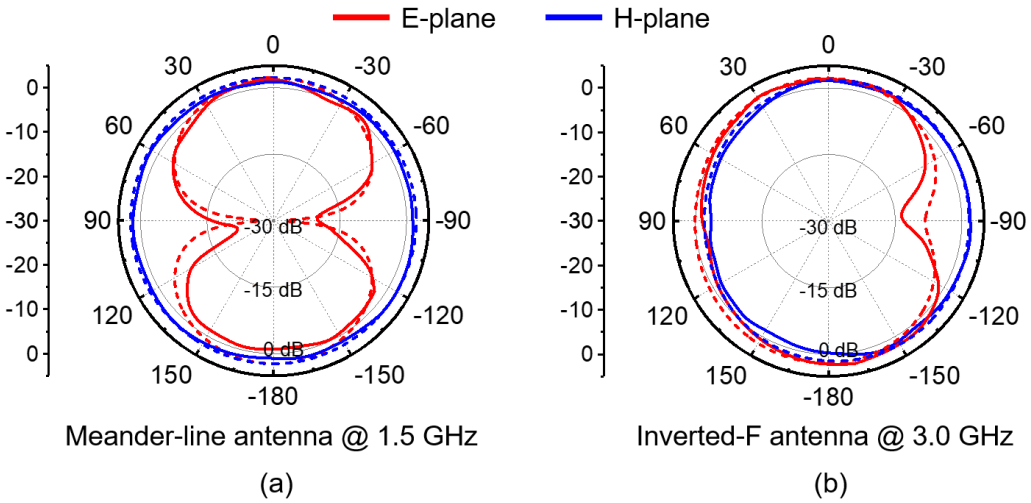


Figure 62. Measured (solid line) and simulated (dashed) radiation patterns for (a) the meander-line antenna at 1.5 GHz and (b) the printed inverted-F antenna at 3.0 GHz on the E-plane (x-z plane) and H-plane (y-z plane).

Fig. 62 reports the simulated and measured radiation patterns of the meander-line and inverted-F antennas in Fig. 61 at their resonant frequencies. It is evident that the measured radiation patterns are in good agreement with the simulated ones on the E-plane (*x*-*z*-plane) and H-plane (*y*-*z* plane). The meander line antenna exhibits an omnidirectional radiation property at 1.5 GHz, with the maximum measured gain of 2.1 dBi and the half-power beam width (HPBW) of 95° on the E-plane. The inverted-F antenna has the maximum gain of 2.45 dBi at 3.0 GHz, with the HPBW of 105° on the E-plane. Both antennas have the radiation efficiency greater than 85 % at the resonant frequency.

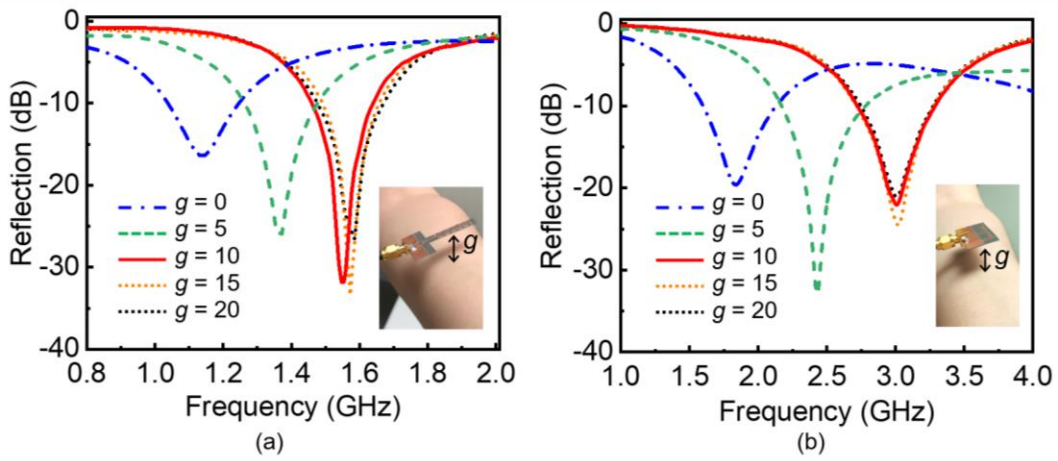


Figure 63. Measured reflection spectra for (a) the meander-line antenna and (b) the inverted-F antenna, as a function of the dimension of gap (g [mm]) between the antenna and human body; the insets show the photograph of the measurement setup.

Next, we will report the effect of human body on radiation properties of the wearable antennas in Fig. 62. In our experiment, the antenna was placed in the vicinity of human body (hand tissues), and the air gap (*g*) between the antenna and the tissues was varied from 0 mm (i.e., attached onto the skin) to 20 mm. The antenna was connected to the Agilent N5222A PNA

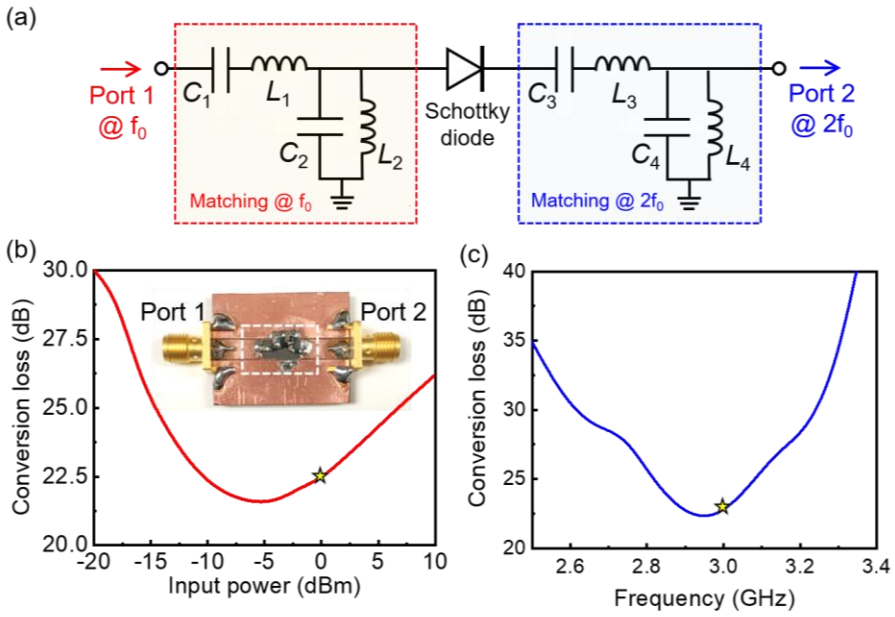


Figure 64. (a) Circuit diagram of a lumped element-based frequency doubler, and its measured conversion loss in dB (b) at different input power levels and (c) at different input frequencies.

microwave network analyzer to track variations of the resonant frequency with the air gap size. Fig. 63(a) reports the measured reflection spectra of the meander-line antenna in Fig. 62(a), showing that when the antenna moves toward the human body, the resonant frequency decreases from 1.5 GHz to 1.15 GHz. Moreover, there is a threshold, $g$ = 10 mm, beyond which the resonant frequency is nearly unchanged and locked at 1.5 GHz. In the same vein, as can be seen in Fig. 63(b), the resonant frequency of the inverted-F antenna in Fig. 62(b) is downshifted from 3.0 GHz to 1.6 GHz in response to reduction of air gap, with a threshold distance, $g$ = 10 mm. According to the cavity perturbation theory, the downshift of resonant frequency in response to dielectric perturbations is proportional to the perturbed field strength [31], [32]. Therefore, due to strong

electric fields in the close vicinity of the antennas, any change in the air gap, if within 10 mm, could cause a remarkable resonant frequency shift. On the contrary, if the antenna is away from tissues, the resonant frequency is nearly independent of the air gap size. When the antennas are utilized in the harmonic tag inside the face mask, their resonant frequencies may be significantly detuned under the normal wearing condition ($g$ < 5 mm). However, when cough happens, the space between the antenna and facial surface increases ($g$ > 10 mm) and, therefore, the operating frequencies of the meander-line and inverted-F antennas may be reconfigured to the fundamental and second-harmonic frequencies (i.e., 1.5 GHz and 3.0 GHz). In this scenario, a second-harmonic RSSI can be detected by the reader or sniffer in the far zone.

Table VII: Parameters of lumped elements with units: C (pF) and L (nH)

| Par. | $C_1$ | $L_1$ | $C_2$ | $L_2$ | $C_3$ | $L_3$ | $C_4$ | $L_4$ |
|---|---|---|---|---|---|---|---|---|
| Value | 10 | 22 | 3.3 | 3.9 | 1.8 | 1.5 | 10 | 33 |

Fig. 64(a) shows the schematic diagram of a miniaturized frequency doubler, whose input and output ports are connected to the meander-line antenna and the inverted-F antenna. In order to save the area of harmonic tag, the bandpass filters and matching networks were constructed by lumped elements and a Schottky diode (SMS 7621), with the important design parameters listed in Table VII. The passbands of the *LC* band-pass filters on the input and output sides are centered 1.5 GHz and 3.0 GHz, respectively. The Advanced Design Simulator (ADS) was utilized to design the frequency doubler [33]. The photograph of the fabricated frequency doubler is shown in the inset of Fig. 64(b). Fig. 64(b) reports the measurement results for the relationship between the

conversion loss and input RF power at 1.5 GHz. We find that at the 0 dBm input level, the conversion loss is ~22.5 dB. Fig. 64(c) reports the measurement results for the conversion loss versus the second-harmonic frequency at input power of 0 dBm. The frequency dependency shows that the minimum conversion loss (~22.5 dB) was obtained at 3.0 GHz.

Finally, the afore-studied antennas and frequency multiplier were integrated to make a passive harmonic transponder (Fig. 60(c)). This compact, low-profile passive harmonic tag was sandwiched between a typical face mask and a protection layer to form a smart face mask for wireless cough monitoring applications (Fig. 60(b)).

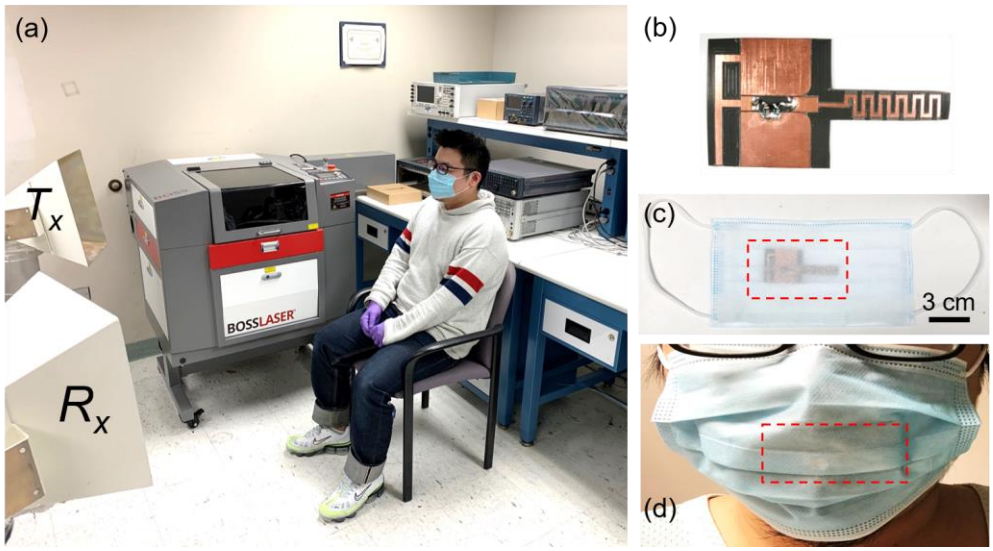


Figure 65. (a) Bistatic measurement setup in an indoor environment. Photograph of (b) the passive harmonic tag, (c) the assembled smart face mask, and (d) the smart face mask worn by the user.

### 7.3 Wireless smart face mask for cough monitoring

We adopted the bistatic measurement setup in a cluttered indoor environment, as illustrated in Fig.

65(a). Figs. 65(b)-(d) present the photographs of the fabricated passive harmonic transponder, the assembled smart face mask, and an user wearing the smart face mask, respectively. During the measurement, the reader's transceiver continuously launches an CW interrogation signal (at 1.5 GHz) to the user wearing the smart face mask. The frequency and pattern of cough can be obtained from the recorded time series of the second-harmonic RSSI (at 3.0 GHz). According to the Friis transmission equation, the second-harmonic RSSI (i.e., received power $P_r$) can be estimated as [34]:

$$\frac{P_r}{P_t} = \left( \frac{\lambda_0}{4\pi\sqrt{2R_1R_2}} \right)^4 \times \frac{G_T(f_0)G_r(f_0,g)G_t(2f_0,g)G_R(2f_0)}{L_{sys}} \qquad (16)$$

where $G_r$ is the realized gain of the meander-line antenna at $f_0$, $G_t$ is the realized gain of the inverted-F antenna at $2f_0$, $G_T$ ($G_R$) denote the realized gain of the reader's transmitter (sniffer), $R_1$ ($R_2$) is the distance between reader (sniffer) and the face mask, $L_{sys}$ is the overall system loss including the conversion loss of the frequency doubler and the insertion loss in filters and transmission line. Some important parameters include: $P_t$ = 20 dBm, $R_1 = R_2$ = 1 m, $G_T$ = 12.5 dBi at 1.5 GHz, and $G_R$ = 15.0 dBi at 3.0 GHz. From Eq. (16), it is evident that under a fixed transmitted power $P_t$, the received power $P_r$ is proportional to the realized gain $G_r$ and $G_t$ of the antennas, which have been demonstrated to be sensitive to the occurrence of cough, as can be seen in Fig. 63. In short, when the user wearing the harmonic mask is at rest (which corresponds to the OFF state of the harmonic tag), resonant frequencies of antennas do not match to 1.5 GHz and 3 GHz, leading to a very small $G_r$ and $G_t$, and thus low harmonic RSSI, as can be seen in Fig. 66(a). On the other hand, the occurrence of cough can dynamically reconfigure the resonant frequencies of the meander-line antenna and the inverted-F antenna to 1.5 GHz and 3 GHz. Therefore, a harmonic

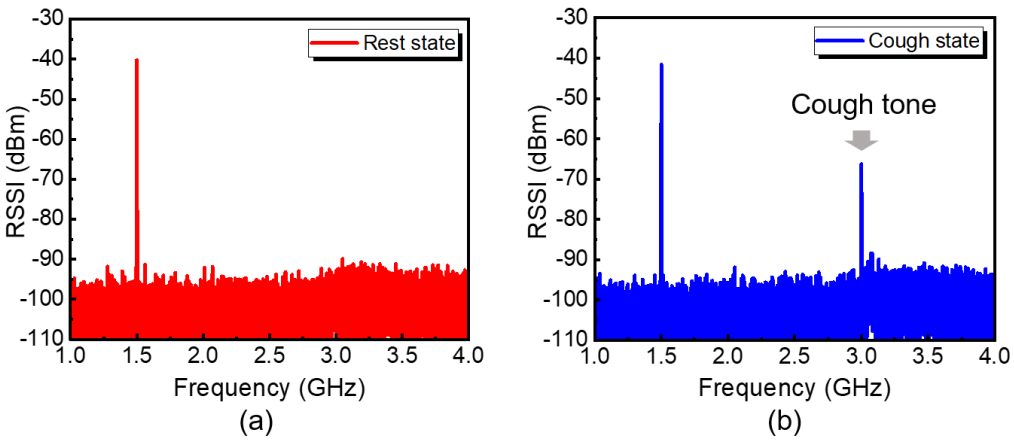


Figure 66. Measured RSSI in the physical state of (a) peaceful rest and (b) cough; the interrogating signal is an unmodulated CW carrier at 1.5 GHz.

RSSI peak can be detected, as can be seen in Fig. 66(b). Consequently, the cough events can be continuously monitored by analyzing the harmonic RSSI pattern over time. We note that in both cough and non-cough cases, due to the serious crosstalk and clutters, a backscattered signal was always detected at the fundamental frequency.

Finally, we validate robustness and effectiveness of our platform by performing the real-time cough monitoring in the noisy environment. The harmonic RSSI is recorded over 100 s. The results reported in Fig. 67(a) shows that the proposed smart face mask enables robust, accurate, and real-time cough monitoring. Figs. 67(b) and(c) present the measured time series of the second-harmonic RSSI at different interrogation distances (see Fig. 65); here, except for the tag-to-sniffer distance ($R_2$), all the other measurement conditions remain the same. It is evidently seen that the pattern of transient response of the smart face mask remains unchanged, regardless of the

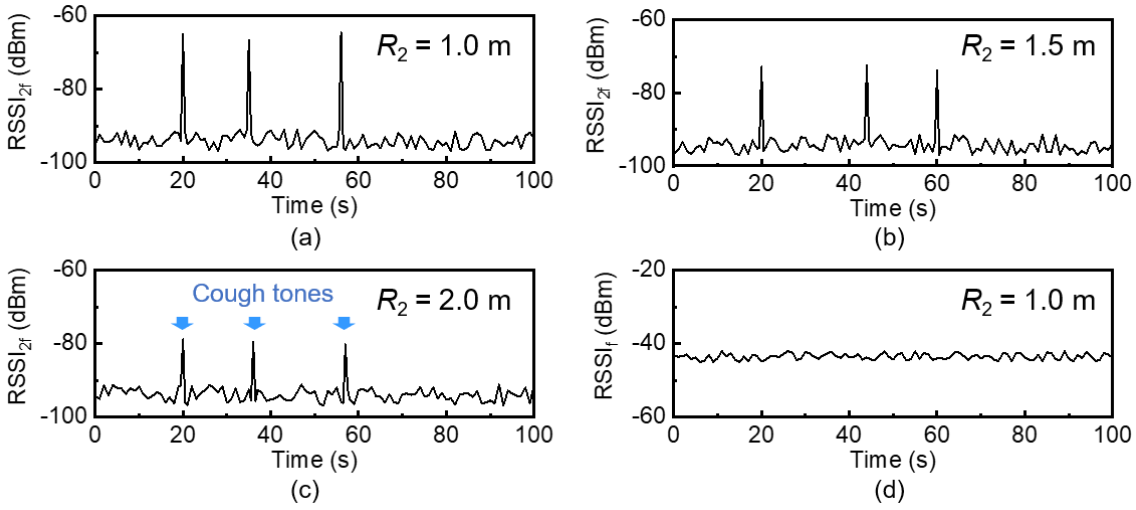


Figure 67. Measured time series of harmonic RSSI at an interrogating distance of (a) 1.0 m, (b) 1.5 m, and (c) 2.0 m. (d) Similar to (a)-(c), but for a traditional passive backscattered mask.

interrogation distance. Therefore, we conclude that the proposed wearable device may provide an accurate cough monitoring with excellent robustness and reliability. For a comparison, we also employed the traditional passive antenna sensor to wirelessly monitor the same cough event. This antenna sensor consists of a microstrip meander-line antenna terminated by a 50 Ω match load. The measured variations of RSSI at 1.5 GHz is presented in Fig. 67(d). Obviously, although the RSSI is still modulated over time, the measured backscattered signal cannot be differentiated from the background noises sourced mainly from crosstalks and clutters. Therefore, it is clearly evident that the proposed harmonics-based wearable device may be a promising candidate for accurate real-time monitoring of coughs.

### 7.4 Conclusion

In this paper, we have demonstrated a lightweight, low-profile and fully-passive harmonic tag embedded in a face mask for the continuous, real-time wireless cough monitoring. Specifically, in

the scheme of harmonics-based sensing, the proposed wearable sensor is capable of measuring the frequency and pattern of cough in the far zone of the cluttered indoor environment. Moreover, comparing to traditional cough monitoring approaches based on passive antenna sensors or backscatter RFIDs, the proposed smart face mask could offer much improved accuracy, robustness, and reliability in real-life applications, potentially benefiting the rapid healthcare tests (e.g., point-of-care testing and driver through tests), telemedicine, healthcare internet-of-things, and biomedical and clinical research.

## REFERENCES


[1] K. F. Chung, "Methods of assessing cough and antitussives in man," *Pulmonary Pharmacol.*, vol. 9, pp. 373-377, 1996.

[2] R. S. Irwin, F. J. Curley, and C. L. French, "Chronic cough. The spectrum and frequency of causes, key components of the diagnostic evaluation, and outcome of specific therapy," *A. Rev. Respiratory Disease*, vol. 141, no. 3, pp. 640-647, 1990.

[3] C. L. French, R. S. Irwin, F. J. Curley, and C. J. Krikorian, "Impact of chronic cough on quality of life," *Arch. Intern. Med.*, vol. 158, no. 15, pp. 1657-1661, 1998.

[4] R. S. Irwin, C. T. French, and K. E. Fletcher, "Quality of life in coughers," *Pulmonary Pharmacol. Therapeutics*, vol. 15, no. 3, pp. 283-286, 2002.

[5] Y. Y. Zheng, Y. T. Ma, J. Y. Zhang and X. Xie, "COVID-19 and the cardiovascular system," *Nat. Rev. Cardiol.*, 2020.

[6] H. A. Bickerman and S. E. Itkin, "The effect of a new bronchodilator aerosol on the air flow dynamics of the maximal voluntary cough of patients with bronchial asthma and pulmonary emphysema," *Journal of Chronic Diseases*, vol. 8, no. 5, pp. 629-638, 1958.

[7] W. T. Goldsmith, A. M. Mahmoud, J. S. Reynolds, W. G. Mckinney, et al., "A system for recording high fidelity cough sound and airflow characteristics," *Ann. Biomed. Eng.*, vol. 38, no. 2, pp. 469-477, 2010.

[8] S. Ren, Y. Shi, M. Cai, and W. Xu, "Influence of secretion on airflow dynamics of mechanical ventilated respiratory system," *IEEE/ACM Trans. Comput. Biol. Bioinform.*, vol. 15, no. 5, pp. 1660-1668, 2018.

[9] S. Ren, M. Cai, Y. Shi, W. Xu, and X. D. Zhang, "Influence of bronchial diameter change on the airflow dynamics based on a pressure-controlled ventilation system," *Int. J. Numer. Method Biomed. Eng.*, vol. 34, no. 3, 2018.

[10] Y. Hu, E. G. Kim, G. Cao, S. Liu, and Y. Xu, "Physiological acoustic sensing based on accelerometers: a survey for mobile healthcare," *Ann. Biomed. Eng.*, vol. 42, no. 11, p. 2264–2277, 2014.

[11] S. Subburaj, L. Parvez, and T. G. Rajagopalan, "Methods of recording and analysing cough sounds," *Pulmonary Pharmacol.*, vol. 9, pp. 269-279, 1996.

[12] P. Munyard, C. Busst, R. Logan-Sinclair, and A. Bush, "A new device for ambulatory cough recording," *Pediatr. Pulmonol.*, vol. 18, no. 3, pp. 178-186, 1994.

[13] C. Liu, J. Xiong, L. Cai, L. Feng, and X. Chen, et al., "Beyond respiration: Contactless sleep sound-activity recognition using RF signals," *in Proceedings of the ACM on Interactive, Mobile, Wearable and Ubiquitous Technologies (ACM UbiComp).*, vol. 3, no. 3, pp. 1-22, 2019.

[14] P. Sharma, X. Hui and E. C. Kan, "A wearable RF sensor for monitoring respiratory patterns," *in 41st Annual International Conference of the IEEE Engineering in Medicine and Biology Society (EMBC)*, pp. 1217-1223, 2019.

[15] L. Zhu, and P. Y. Chen, "A compact, zero-power and low-noise harmonic-transponder for liquid and moisture sensing," in 2019 *IEEE International Symposium on Antennas and Propagation and USNC-URSI Radio Science Meeting*, Atlanta, GA, USA, USA, 2019.

[16] L. Zhu, N. Alsaab, M. M. C. Cheng and P. Y. Chen, "A zero-power ubiquitous wireless liquid-level sensor based on microfluidic-integrated microstrip antenna," *IEEE J. Radio Freq. Identification*, vol. 4, no. 3, pp. 265-274, 2020.

[17] L. Zhu, M. Farhat, Y. C. Chen, K. N. Salama and P. Y. Chen, "A compact, passive frequency-hopping harmonic sensor based on a microfluidic reconfigurable dual-band antenna," *IEEE Sens. J.*, vol. 20, no. 21, pp. 12495-12503, 2020.

[18] D. Mascanzoni and H. Wallin, "The harmonic radar: A new method of tracing insects in the fields," *Ecol. Entomol.*, vol. 11, pp. 387-390, 1986.

[19] B. G. Colpitts, G. Boiteau, "Harmonic radar transceiver design: miniature tags for insect tracking," *IEEE Trans. Antennas Propag.*, vol. 52, no. 11, pp. 2825-2832, 2004.

[20] L. Zhu, N. Alkhaldi, H. M. Kadry, S. L. Liao, and P. Y. Chen, "A compact hybrid-fed microstrip antenna for harmonics-based radar and sensor system,", vol. 17, no. 12, pp. 2444-2448, 2018.

[21] J. R. Riley, A. D. Smith, D. R. Reynolds, and A. S. Edwards, "Tracking bees with harmonic radar," *Nature,* vol. 379, pp. 29-30, 1996.

[22] V. Palazzi, F. Alimenti, P. Mezzanotte, G. Orecchini, and L. Roselli, "Zero-power, long-range, ultra low-cost harmonic wireless sensors for massively distributed monitoring of cracked walls," *in IEEE MTT-S Int. Microw. Symp. Dig.*, Honolulu, HI, USA, Jun, 2017.

[23] C. Cho, X. H. Yi, D. Li, Y. Wang, and M. M. Tentzeris, "Passive wireless Frequency doubling antenna sensor for strain and crack sensing," *IEEE Sens. J.*, vol. 16, no. 14, pp. 5725-5733, 2016.

[24] A. Lazaro, R. Villarino, and D. Girbau, "A passive harmonic tag for humidity sensing," *Int. J. Antennas Propag.*, p. 670345, 2014.

[25] H. Huang, P. Y. Chen, C. H. Hung, R. Gharpurey, and D. Akinwande, "A zero power harmonic transponder sensor for ubiquitous wireless μL liquid-volume monitoring," *Sci. Rep.*, vol. 6, p. 18795, 2016.

[26] M. Hajizadegan, M. Sakhdari, L. Zhu, Q. S. Cui, H. Y. Huang, M. C. Cheng, et al, "Graphene sensing modulator: Toward low-noise, self-powered wireless microsensors," *IEEE Sens. J.*, vol. 17, no. 22, pp. 7239-7247, 2017.

[27] X. Hui and E. C. Kan, "Monitoring vital signs over multiplexed radio by near-field coherent sensing," *Nat. Electron.*, vol. 1, no. 1, pp. 74-78, 2018.

[28] L. Zhu, H. Huang, M. M. C. Cheng and P. Y. Chen, "Compact, flexible harmonic transponder sensor with multiplexed sensing capabilities for rapid, contactless microfluidic diagnosis," *IEEE Trans. Microw. Theory Tech.*, vol. 68, no. 11, pp. 4846-4854, 2020.

[29] A. Abdelnour, A. Lazaro, R. Villarino, D. Kaddour, S. Tedjini and D. Girbau, "Passive harmonic RFID system for buried assets localization," *sensors,* vol. 18, no. 11, p. 3635, 2018.

[30] X. Hui, Y. Ma, and E. C. Kan, "Code division multiple access in centimeter accuracy harmonic RFID locating system," *IEEE J. Radio Freq. Identification,* vol. 1, no. 1, pp. 51-58, 2017.

[31] C. Gao, T. Wei, F. Duewer, Y. Lu,and X. D. Xiang, "High spatial resolution quantitative microwave impedance microscopy by a scanning tip microwave near-field microscope," *Appl. Phys. Lett.*, vol. 71, pp. 1872-1874, 1997.

[32] H. Huang, P. S. Zhao, P. Y. Chen, Y. Ren, X. Liu, et al., "RFID tag helix antenna sensors for wireless drug dosage monitoring," *IEEE J. Transl. Eng. Health Med.,* vol. 2, pp. 1-8, 2014.

[33] *Keysight PathWave Advanced Design System (ADS), Keysight Technol.*, Santa Rosa, CA, USA, 2020.

[34] J. A. Shaw, "Radiometry and the Friis transmission equation," *Am. J. Phys.*, vol. 81, no. 1, pp. 33-37, 2013.

# VIII. CONCLUSIONS

In this thesis, I have proposed a type of conformal and low-profile microstrip antenna for compact harmonic transponder applications. The proposed hybrid-fed geometry has apparently isolated resonances between the fundamental and second harmonic frequencies, which could be predicted analytically by solving transcendental equations. Additionally, I have demonstrated that the $TM_{110}$ and $TM_{210}$ (or $TM_{310}$) modes could be excited at 3 GHz and 6 GHz, respectively, by tailoring the feeding, as well as the antenna geometry. The measurement results exhibit a satisfactory realized gain of the antennas with symmetrical broadside radiation patterns, along with good impedance matching and port isolation.

I have introduced a compact elliptical microstrip patch antenna for harmonic sensing applications that demand dual resonance excited simultaneously at the fundamental frequency ($f_0$) and second-harmonic frequency ($2f_0$). Specifically, I have studied an elliptical patch perturbated with shorting vias, thereby exhibiting an even order $TM_{e110}$ mode at $f_0$ and an odd order $TM_{o110}$ resonant mode at $2f_0$, not coupling to the rest higher-order modes. Moreover, these two operating modes have been demonstrated with the orthogonal linear polarizations, further minimizing the background electromagnetic interferences. I have integrated this dual-resonance antenna with a fluidic channel, and developed a harmonic liquid sensor, which could successfully detect different concentration of the acetone-water mixtures, without being interrupted by multiple scattering generated from the surrounding clutters.

I have also developed a reconfigurable dual-band antenna for realizing far-field wireless frequency-hopping sensing. The proposed antenna, loaded properly with a fluidic channel, is able to exhibit a reconfigurable narrow resonance of the fundamental frequency and an unvaried wideband resonance of the second-harmonic band. I have demonstrated that this dual band antenna is useful

for frequency-hopping telemetry scheme, allowing for robust wireless mixture sensing in rich-scattering environments.

To meet the requirement for wireless dual-channel sensing, I have demonstrated a compact harmonic tag with a scalable and multiplexed monitoring capability. By hybridizing this harmonic tag with multiple fluidic channels, I have built a battery-free multiplexed harmonic sensor and demonstrated its capability for contactlessly monitoring properties of solutions in an indoor environment. I envision that such multiplexed harmonic tags can also be integrated with the system-level fluidic networks, e.g., sorting cells or diagnostic assays, to maximize its potential in telemetering, wireless sensing, lab-on-a-chip, and rapid healthcare tests applications.

At last, I have demonstrated a lightweight, low-profile and fully-passive harmonic tag embedded in a face mask for the continuous, real-time wireless cough monitoring. Specifically, in the scheme of harmonics-based sensing, the proposed wearable sensor is capable of measuring the frequency and pattern of cough in the far zone of the cluttered indoor environment. Moreover, comparing to traditional cough monitoring approaches based on passive antenna sensors or backscatter RFIDs, the proposed smart face mask could offer much improved accuracy, robustness, and reliability in real-life applications, potentially benefiting the rapid healthcare tests (e.g., point-of-care testing and driver through tests), telemedicine, healthcare internet-of-things, and biomedical and clinical research

# APPENDIX: COPYRIGHT PERMISSIONS

In this appendix, I present the copyright permissions for the articles, whose contents were used in this thesis. The list of the articles includes an article in IEEE Antennas and Wireless Propagation Letters (Liang et al., 2018, IEEE AWPL), an article in IEEE Sensor Journals (Liang et al., 2020, IEEE Sensor), an article in IEEE Transactions on Microwave Theory and Techniques (Liang et al., 2019, IEEE TMTT), an article in Measurement Science and Technology (Liang et al., 2021, MST).

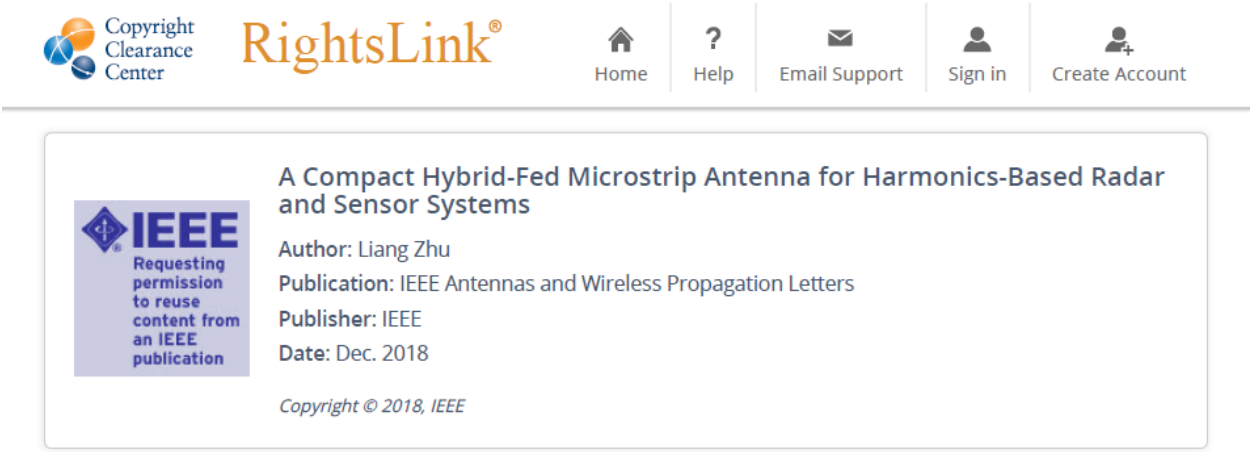


**Thesis / Dissertation Reuse**

**The IEEE does not require individuals working on a thesis to obtain a formal reuse license, however, you may print out this statement to be used as a permission grant:**

Requirements to be followed when using any portion (e.g., _gure, graph, table, or textual material) of an IEEE copyrighted paper in a thesis:

1) In the case of textual material (e.g., using short quotes or referring to the work within these papers) users must give full credit to the original source (author, paper, publication) followed by the IEEE copyright line © 2011 IEEE.

2) In the case of illustrations or tabular material, we require that the copyright line © [Year of original publication] IEEE appear prominently with each reprinted _gure and/or table.

3) If a substantial portion of the original paper is to be used, and if you are not the senior author, also obtain the senior author's approval. Requirements to be followed when using an entire IEEE copyrighted paper in a thesis:

1) The following IEEE copyright/ credit notice should be placed prominently in the references: © [year of original publication] IEEE. Reprinted, with permission, from [author names, paper title, IEEE publication title, and month/year of publication]

2) Only the accepted version of an IEEE copyrighted paper can be used when posting the paper or your thesis online.

3) In placing the thesis on the author's university website, please display the following message in a prominent place on the website: In reference to IEEE copyrighted material which is used with permission in this thesis, the IEEE does not endorse any of [university/educational entity's name goes here]'s products or services. Internal or personal use of this material is permitted. If interested in reprinting/republishing IEEE copyrighted material for advertising or promotional purposes or for creating new collective works for resale or redistribution, please go to http://www.ieee.org/publications_standards/publications/rights/rights_link.html to learn how to obtain a License from RightsLink.

If applicable, University Micro_lms and/or ProQuest Library, or the Archives of Canada may supply single copies of the dissertation.


**Thesis / Dissertation Reuse**

**The IEEE does not require individuals working on a thesis to obtain a formal reuse license, however, you may print out this statement to be used as a permission grant:**

Requirements to be followed when using any portion (e.g., _gure, graph, table, or textual material) of an IEEE copyrighted paper in a thesis:

1) In the case of textual material (e.g., using short quotes or referring to the work within these papers) users must give full credit to the original source (author, paper, publication) followed by the IEEE copyright line © 2011 IEEE.

2) In the case of illustrations or tabular material, we require that the copyright line © [Year of original publication] IEEE appear prominently with each reprinted _gure and/or table.

3) If a substantial portion of the original paper is to be used, and if you are not the senior author, also obtain the senior author's approval. Requirements to be followed when using an entire IEEE copyrighted paper in a thesis:

1) The following IEEE copyright/ credit notice should be placed prominently in the references: © [year of original publication] IEEE. Reprinted, with permission, from [author names, paper title, IEEE publication title, and month/year of publication]

2) Only the accepted version of an IEEE copyrighted paper can be used when posting the paper or your thesis online.

3) In placing the thesis on the author's university website, please display the following message in a prominent place on the website: In reference to IEEE copyrighted material which is used with permission in this thesis, the IEEE does not endorse any of [university/educational entity's name goes here]'s products or services. Internal or personal use of this material is permitted. If interested in reprinting/republishing IEEE copyrighted material for advertising or promotional purposes or for creating new collective works for resale or redistribution, please go to http://www.ieee.org/publications_standards/publications/rights/rights_link.html to learn how to obtain a License from RightsLink.

If applicable, University Micro_lms and/or ProQuest Library, or the Archives of Canada may supply single copies of the dissertation.

**Thesis / Dissertation Reuse**

**The IEEE does not require individuals working on a thesis to obtain a formal reuse license, however, you may print out this statement to be used as a permission grant:**

Requirements to be followed when using any portion (e.g., _gure, graph, table, or textual material) of an IEEE copyrighted paper in a thesis:

1) In the case of textual material (e.g., using short quotes or referring to the work within these papers) users must give full credit to the original source (author, paper, publication) followed by the IEEE copyright line © 2011 IEEE.

2) In the case of illustrations or tabular material, we require that the copyright line © [Year of original publication] IEEE appear prominently with each reprinted _gure and/or table.

3) If a substantial portion of the original paper is to be used, and if you are not the senior author, also obtain the senior author's approval. Requirements to be followed when using an entire IEEE copyrighted paper in a thesis:

1) The following IEEE copyright/ credit notice should be placed prominently in the references: © [year of original publication] IEEE. Reprinted, with permission, from [author names, paper title, IEEE publication title, and month/year of publication]

2) Only the accepted version of an IEEE copyrighted paper can be used when posting the paper or your thesis online.

3) In placing the thesis on the author's university website, please display the following message in a prominent place on the website: In reference to IEEE copyrighted material which is used with permission in this thesis, the IEEE does not endorse any of [university/educational entity's name goes here]'s products or services. Internal or personal use of this material is permitted. If interested in reprinting/republishing IEEE copyrighted material for advertising or promotional purposes or for creating new collective works for resale or redistribution, please go to http://www.ieee.org/publications_standards/publications/rights/rights_link.html to learn how to obtain a License from RightsLink.

If applicable, University Micro_lms and/or ProQuest Library, or the Archives of Canada may supply single copies of the dissertation.

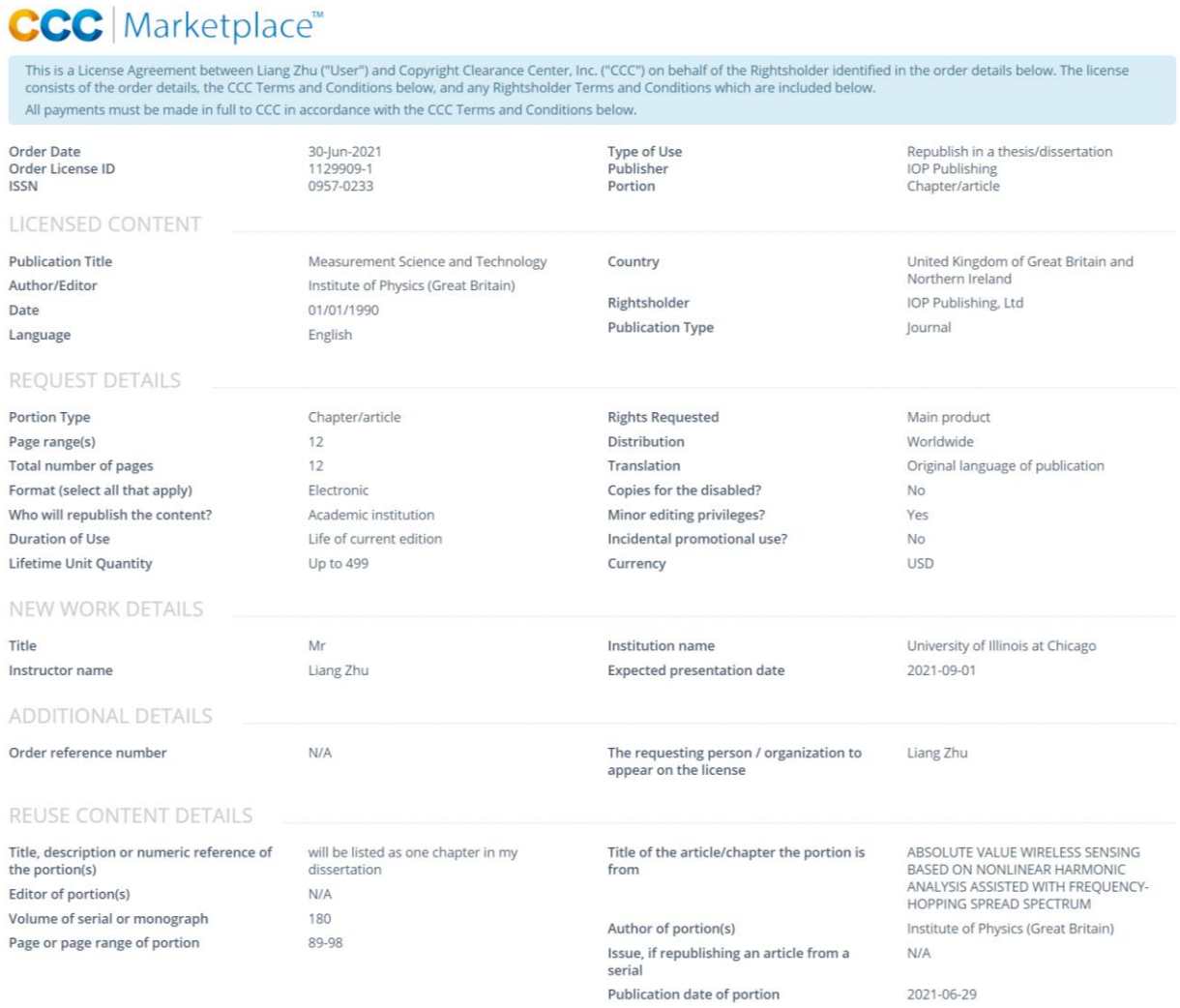

CCC Marketplace™

This is a License Agreement between Liang Zhu ("User") and Copyright Clearance Center, Inc. ("CCC") on behalf of the Rightsholder identified in the order details below. The license consists of the order details, the CCC Terms and Conditions below, and any Rightsholder Terms and Conditions which are included below.

All payments must be made in full to CCC in accordance with the CCC Terms and Conditions below.

| | | | |
|---|---|---|---|
| Order Date | 30-Jun-2021 | Type of Use | Republish in a thesis/dissertation |
| Order License ID | 1129909-1 | Publisher | IOP Publishing |
| ISSN | 0957-0233 | Portion | Chapter/article |

LICENSED CONTENT

| | | | |
|---|---|---|---|
| Publication Title | Measurement Science and Technology | Country | United Kingdom of Great Britain and Northern Ireland |
| Author/Editor | Institute of Physics (Great Britain) | Rightsholder | IOP Publishing, Ltd |
| Date | 01/01/1990 | Publication Type | Journal |
| Language | English | | |

REQUEST DETAILS

| | | | |
|---|---|---|---|
| Portion Type | Chapter/article | Rights Requested | Main product |
| Page range(s) | 12 | Distribution | Worldwide |
| Total number of pages | 12 | Translation | Original language of publication |
| Format (select all that apply) | Electronic | Copies for the disabled? | No |
| Who will republish the content? | Academic institution | Minor editing privileges? | Yes |
| Duration of Use | Life of current edition | Incidental promotional use? | No |
| Lifetime Unit Quantity | Up to 499 | Currency | USD |

NEW WORK DETAILS

| | | | |
|---|---|---|---|
| Title | Mr | Institution name | University of Illinois at Chicago |
| Instructor name | Liang Zhu | Expected presentation date | 2021-09-01 |

ADDITIONAL DETAILS

| | | | |
|---|---|---|---|
| Order reference number | N/A | The requesting person / organization to appear on the license | Liang Zhu |

REUSE CONTENT DETAILS

| | | | |
|---|---|---|---|
| Title, description or numeric reference of the portion(s) | will be listed as one chapter in my dissertation | Title of the article/chapter the portion is from | ABSOLUTE VALUE WIRELESS SENSING BASED ON NONLINEAR HARMONIC ANALYSIS ASSISTED WITH FREQUENCY-HOPPING SPREAD SPECTRUM |
| Editor of portion(s) | N/A | Author of portion(s) | Institute of Physics (Great Britain) |
| Volume of serial or monograph | 180 | Issue, if republishing an article from a serial | N/A |
| Page or page range of portion | 89-98 | Publication date of portion | 2021-06-29 |

**RIGHTSHOLDER TERMS AND CONDITIONS**

These special terms and conditions are in addition to the standard terms and conditions for CCC's Republication Service and, together with those standard terms and conditions, govern the use of the Works. As the User you will make all reasonable efforts to contact the author(s) of the article which the Work is to be reused from, to seek consent for your intended use. Contacting one author who is acting expressly as authorised agent for their co-author(s) is acceptable. User will reproduce the following wording prominently alongside the Work: the source of the Work, including author, article title, title of journal, volume number, issue number (if relevant), page range (or first page if this is the only information available) and date of first publication; and a link back to the article

(via DOI); and if practicable, and IN ALL CASES for new works published under any of the Creative Commons licences, the words "© IOP Publishing. Reproduced with permission. All rights reserved" Without the express permission of the author(s) and the Rightsholder of the article from which the Work is to be reused, User shall not use it in any way which, in the opinion of the Rightsholder, could: (i) distort or alter the author(s)' original intention(s) and meaning; (ii) be prejudicial to the honour or reputation of the author(s); and/or (iii) imply endorsement by the author(s) and/or the Rightsholder. This licence does not apply to any article which is credited to another source and which does not have the copyright line '© IOP Publishing Ltd'. User must check the copyright line of the article from which the Work is to be reused to check that IOP Publishing Ltd has all the necessary rights to be able to grant permission. User is solely responsible for identifying and obtaining separate licences and permissions from the copyright owner for reuse of any such third party material/figures which the Rightsholder is not the copyright owner of. The Rightsholder shall not reimburse any fees which User pays for a republication license for such third party content. This licence does not apply to any material/figure which is credited to another source in the Rightsholder's publication or has been obtained from a third party. User must check the Version of Record of the article from which the Work is to be reused, to check whether any of the material in the Work is third party material. Third party citations and/or copyright notices and/or permissions statements may not be included in any other version of the article from which the Work is to be reused and so cannot be relied upon by the User. User is solely responsible for identifying and obtaining separate licences and permissions from the copyright owner for reuse of any such third party material/figures where the Rightsholder is not the copyright owner. The Rightsholder shall not reimburse any fees which User pays for a republication license for such third party content. User and CCC acknowledge that the Rightsholder may, from time to time,

make changes or additions to these special terms and conditions without express notification, provided that these shall not apply to permissions already secured and paid for by User prior to such change or addition. User acknowledges that the Rightsholder (which includes companies within its group and third parties for whom it publishes its titles) may make use of personal data collected through the service in the course of their business. If User is the author of the Work, User may automatically have the right to reuse it under the rights granted back when User transferred the copyright in the article to the Rightsholder. User should check the copyright form and the relevant author rights policy to check whether permission is required. If User is the author of the Work and does require permission for proposed reuse of the Work, User should select 'Author of requested content' as the Requestor Type. The Rightsholder shall not reimburse any fees which User pays for a republication license. If User is the author of the article which User wishes to reuse in User's thesis or dissertation, the republication licence covers the right to include the Version of Record of the article, provided it is not then shared or deposited online. User must include citation details. Where User wishes to share their thesis or dissertation online, they should remove the Version of Record before uploading it. User may include a Preprint or the Accepted Manuscript (after the embargo period) in the online version of the thesis or dissertation, provided they do so in accordance with the Rightsholder's policies on sharing Preprints or Accepted Manuscripts. User may need to obtain separate permission for any third party content included within the article. User must check this with the copyright owner of such third party content. Any online or commercial use of User's thesis or dissertation containing the article, including publication via ProQuest, would need to be expressly notified in writing to the Rightsholder at the time of request and would require separate written permission from the Rightsholder. As well as CCC, the Rightsholder shall have the right to bring any legal action that it deems necessary to enforce its rights should it

consider that the Work infringes those rights in any way. For content reuse requests that qualify for permission under the STM Permissions Guidelines, which may be updated from time to time, the STM Permissions Guidelines supplement the terms and conditions contained in this license.

SPECIAL RIGHTSHOLDER TERMS AND CONDITIONS

When you transferred the copyright in your article to IOP, we granted back to you certain rights, including the right to include all or part of the Final Published Version of the article within any thesis or dissertation. Please note you may need to obtain separate permission for any third party content you included within your article. Please include citation details, "© IOP Publishing. Reproduced with permission. All rights reserved" and for online use, a link to the Version of Record. The only restriction is that if, at a later date, you wanted your thesis/dissertation to be published commercially, further permission would be required.

**VITA**

NAME: Liang Zhu

EDUCATION: Ph.D., Electrical and Computer Engineering, University of Illinois at Chicago, IL, USA, 2021

M.S., in Optics, Sun Yat-Sen University, China, 2015

B.S., in Optical information Science and Technology, Sun Yat-Sen University, China, 2012

PUBLICATIONS:

L. Zhu, M. Farhat, K. N. Salama, P. Y. Chen, "Emerging 2D Materials and Devices for the Internet of Things," 29-57, Elsevier, Jan (2020).

M. Hajizadegan, M. Sakhdari, L. Zhu, H. Huang, M. M. C. Cheng, J. C. H. Hung, and P. Y. Chen, "Graphene Sensing Modulator: Towards Low-Noise, Self-Powered Wireless Microsensors," *IEEE Sensors Journal*, Vol. 17, 7239-7247 (2017).

Y. He, Y. Li, L. Zhu, H. Bagci, D. Erricolo, and P. Y. Chen, "Waveguide Dispersion Tailoring by using Embedded Impedance Surface," *Physical Review Applied*, Vol. 10, 064024 (2018).

T. Guo, L. Zhu, P. Y. Chen, and C. Argyropoulos, "Tunable Terahertz Amplification Based on Photoexcited Active Graphene Hyperbolic Metamaterials," *Optical Material Express*, Vol. 8, 3941-3952 (2018).

L. Zhu, N. Alkhaldi, H. Kadry, S. Liao, and P. Y. Chen, "A Compact Hybrid-Fed Microstrip Antenna for Harmonics-Based Radar and Sensor Systems," *IEEE Antennas and Wireless Propagation Letters*, Vol. 17, 2444 – 2448 (2018).

L. Zhu, N. Alsaab, M. M. C. Cheng and P. Y. Chen, "A Zero-Power Ubiquitous Wireless Liquid-Level Sensor Based on Microfluidic-Integrated

Microstrip Antenna," *IEEE Journal of Radio Frequency Identification*, Vol. 4, No. 3, pp. 265-274 (2020).

L. Zhu, M. Farhat, Y. Chen, K. N. Salama and P. Y. Chen, "A Compact, Passive Frequency-Hopping Harmonic Sensor Based on a Microfluidic Reconfigurable Dual-Band Antenna," *IEEE Sensors Journal*, Vol. 20, No. 21, pp. 12495-12503 (2020).

L. Zhu, H. Huang, M. M. C. Cheng and P. Y. Chen, "Compact, Flexible Harmonic Transponder Sensor With Multiplexed Sensing Capabilities for Rapid, Contactless Microfluidic Diagnosis," *IEEE Transactions on Microwave Theory and Techniques*, Vol. 68, No. 11, pp. 4846-4854 (2020).

Y. He, Y. Li, L. Zhu and P. Y. Chen, "Miniaturization of Omnidirectional Cavity Antennas Using Substrate-Integrated Impedance Surfaces," *IEEE Transactions on Antennas and Propagation*, vol. 69, no. 3, pp. 1728-1733 (2020).

Y. D. Xu, G. Zhao, L. Zhu, Q. H. Fei, Z. Zhang, et al., "Pencil-paper on-skin electronics," *Proceedings of the National Academy of Sciences*, Vol. 117, No. 31, 18292-18301 (2020).

M. Hajizadegan, L. Zhu, and P. Y. Chen, "Superdirective Leaky Radiation from a *PT*-Synthetic Metachannel," *Optical Express*,29, 12330-12343,12 (2021).

Z. Ye, M. Yang, L. Zhu, and P. Y. Chen, "Singularity-Enhanced Sensing in PTX-Symmetric Systems with Single Port Excitation," *Frontiers of optoelectronics*, https://doi.org/10.1007/s12200-021-1204-6 (2021).

L. Zhu, P. Y. Chen, "A Low-Noise, Real-Time and Passive Wireless Sensing System Enabled by Harmonic Detection of Resonance and Frequency-Hopping Spread Spectrum", *Measruement Science and Tecnology*, (2021)

L. Zhu and P. Y. Chen, "Low-Interference Harmonic Transponder Sensor Using Graphene Electronics," URSI in Boulder, 2018.

L. Zhu, M. Sakhdari, M. Cheng and P. Y. Chen, "Transparent and self-Activated Harmonic Microsensors for IoT Healthcare Applications,"

Wireless Integrated MicroSesning & Systems at the University of Michigan, 2017.

L. Zhu and P. Y. Chen, "A Compact Harmonic Sensor Based on a Dual-Resonant Microstrip Antenna Loaded with a Microfluidic Channel," National Committee for the International Union of Radio Science (USNC-URSI) Boulder, Colorado, 2019.

L. Zhu, P. Y. Chen, D. Erricolo, Y. Li, A. Shamim and H. Bagci, "Dispersion and Field Control in A Metasurface-Implanted Waveguide," National Committee for the International Union of Radio Science (USNC-URSI) Boulder, Colorado, 2019.

L. Zhu and P. Y. Chen, "Compact, Noise-Immune and Battery-Free Harmonic Transponder Sensors," 2019 IEEE MTT-S International conference on Microwaves for Intelligent Mobility (ICMIM).

L. Zhu and P. Y. Chen, "High-Performance Infrared Nano-Rectennas Using New Photonic Nanostructures and 2D Materials," The 63rd International Conference on Electron, Ion, and Photon Beam Technology and Nanofabrication, 2019.

P. Y. Chen and L. Zhu, "Controlling Leaky-Wave by Parity-Time Symmetric Metasurfaces," 2019 IEEE MTT-S International Conference on Numerical Electromagnetic and Multiphysics Modeling and Optimization, 2019.

L. Zhu and P. Y. Chen, "A Compact, Zero-Power and Low-Noise Harmonic-Transponder for Liquid and Moisture Sensing," IEEE APS/URSI 2019, July 7-12, Atlanta, Georgia, U.S.A.

M. Hajizadegan, L. Zhu, P. Y. Chen, "Highly Directive Leaky-Wave Antennas Based on PT-Symmetric Metasurfaces," 2019 International Conference on Electromagnetics in Advanced Applications (ICEAA), 9-13 Sept. Granada, Spain.

B. Y. Jin, T. J. Guo, L. Zhu, P. Y. Chen, C, Argyropoulos, "Tunable THz generation and enhanced nonlinear effects with active and passive graphene hyperbolic metamaterials," Smart Photonic and Optoelectronic Integrated Circuits XXII, 2020, San Francisco, California, United States.

L. Zhu, P. Y. Chen, C. Zhang, “High-Performance, Transparent and Flexible Antenna Based on Conductive Nanocomposites”, in 2020 IEEE International Symposium on Antennas and Propagation and North American Radio Science Meeting 5-10 July 2020, Montréal, Québec, Canada.

C. Zhang, L. Zhu, C. G. Ji, L. Jay Guo and P. Y. Chen, “High-Performance Flexible Microwave Antennas with Ultra-high Visible Transparency,” in ICEAA - IEEE APWC 2020, August 10 -14, in Honolulu, Hawaii, USA.